Title
Electrochemistry and photoelectrochemistry in carbon cycle relevant energy systems

Author
Llorente, Mark Justin

Publication Date
2016

Peer reviewed|Thesis/dissertation

UNIVERSITY OF CALIFORNIA, SAN DIEGO

Electrochemistry and photoelectrochemistry in carbon cycle relevant energy systems

A dissertation submitted in partial satisfaction of the requirements for the degree of

Doctor of Philosophy

in

Materials Science & Engineering

by

Mark Justin Llorente

Committee in charge:

Professor Clifford P. Kubiak, Chair
Professor Vitali F. Nesterenko
Professor Jan B. Talbot
Professor Andrea R.Tao
Professor Charles W. Tu

2016

This dissertation of Mark Justin Llorente is approved, and it is acceptable in quality and form for publication on microfilm and electronically:

Chair

University of California, San Diego

2016

DEDICATION

This dissertation is dedicated to my loving lab mates and friends

who have taught me time and again that life has the most value

when we put in the effort to honestly examine it

and in doing so see each other.

EPIGRAPH

A wise man can learn more from a foolish question than a fool can learn from a wise answer.

Bruce Lee

TABLE OF CONTENTS

LIST OF FIGURES

LIST OF TABLES

ACKNOWLEDGEMENTS

As the boss says, for those who pursue it graduate school is the second greatest period of personal growth only after adolescence. I find it appropriate to repeat the adage that it takes a village to raise a child and I have had many wise villagers who have helped me through this long and often trying process. First I must thank my parents and my late grandmother whose endless support throughout my education opened opportunities for me down paths I never could have seen for myself. In particular, my mother's constancy, resourcefulness, generosity, and determination are virtues I aspire to each day. For helping me find my way toward the hard sciences, I must acknowledge two role models and wonderful men, my high school physics teacher Dr. James Dann and the ever generous philanthropist and engineer Diosdado Banatao who instilled in me the desire to grasp the physical world so that I may apply myself to it. I must also acknowledge with much gratitude the Department of Energy Office of Science, especially Dr. Ping Gu who developed the Office of Science Graduate Fellowship that funded my education for three years. The program brought all us fellows to various national labs around the country for its annual conferences. Without these events and opportunities, I would have never met those many brilliant minds nor received kind and assuring words from the world's foremost energy scientists. Each day I carry with me many important lessons both scientific and personal that have given me a broader perspective than the simple graduate school path often affords.

I must acknowledge the profound encouragement and mentorship I have received from my coworkers and collaborators. Dr. Bhupendra Kumar and Dr. Aaron

Sathrum both gave much of their time and energy to personally steer me toward their visions of a capable scientist. Without the two of them I would not have discovered my own balance of theory and experiment that has become greater than the sum of their parts and helped me find confidence in my pursuits. I must acknowledge Dr. Candace Seu and Melissa Clark who both taught me that thoughtful organization creates the space for spontaneous discovery. Both of them brightened my days and I hope I have afforded them the same. I wish to acknowledge Tram Dang for being a sister, guide, partner, and friend who always made sure that whether at work or at play I always knew I had a place. Dr. Jesse Froehlich and Dr. Michael Doud have worked with me the longest and have been a constant thorn in my side on the basketball courts. Their curiosity and optimistic skepticism always kept me asking questions until we could find the right ones to tackle. Dr. Jane Henderson was a source of warmth and support who would never fail to remind me that I have it in me to pursue what I believe in and to put my personal doubts aside to make room for my strengths. Her own perseverance was a constant inspiration.

An absolute acknowledgment that must not be understated, I wish to thank and acknowledge Professor Clifford Kubiak who works tirelessly to ensure his students' needs are met and who infuses us with tough but inspiring words and stories that came to shape him as a scientist. His perpetual belief that there is something worth pursuing in the unknown and relentless adherence to the realities of experiment has taught me the value of never losing enthusiasm especially when the path is unclear.

I must also thank the many people who have lived with me and taken me in during times of feast and famine. Doctor Neil Brahma and Travis Wong were always welcome faces when I would come home. We spent more than three years as roommates and materials science graduates and even more years as friends. San Diego became a real city with them in it. I must also thank Lauren Locascio without whom I know I could not have finished this degree. With her I have come to understand that the unexpected troubles life throws your way may send you to those who can make you stronger and help you up when you have fallen.

Additionally, I cannot forget my many friends who have shined light on other aspects of life while keeping me engaged with my scientific pursuits. Among them I must acknowledge Dr. Catherine Paltin Hicks for whom no prose can do justice. Even were I not to have known her personally through these years of friendship, her grit, compassion, determination, and drive for growth in all pursuits is a model by which I have strengthened my personal and professional foundations. I must also thank Emily Morgan, Cindy Lam, and Amanda Oquendo for joining me on many café trips to work on writing and presentation making.

I wish to also thank my collaborators Dr. Robert Coridan, Dr. Anna Beck, and Dr. Bichlien Nguyen who have worked with me through both of the projects that comprise this dissertation. Special well wishes and thanks go to Bichlien Nguyen for being both a work colleague and an instant friend.

Chapter 2, in part, is related to a patent "Photoassisted high efficiency conversion of carbon-containing fuels to electricity" with shared invention ownership

by Clifford P. Kubiak, Mark J. Llorente, Nathan S. Lewis, Robert H. Coridan, and Anna R. Beck. Additional work came from Bhupendra Kumar.

Chapter 3, in part, is related to a patent "Photoassisted high efficiency conversion of carbon-containing fuels to electricity" with shared invention ownership by Clifford P. Kubiak, Mark J. Llorente, Nathan S. Lewis, Robert H. Coridan, and Anna R. Beck.

Chapter 4, in part, has been submitted for publication as a manuscript entitled "Paired Electrolysis in the Simultaneous Upgrading of Two Renewable Carbon Feedstocks." by Mark J. Llorente, Bichlien N. Nguyen, Kevin D. Moeller, and Clifford P. Kubiak. The dissertation author is the primary author of this manuscript.

VITA

2007	Bachelor of Science, University of California, Berkeley
2012	Master of Science, University of California, San Diego
2016	Doctor of Philosophy, University of California, San Diego

PUBLICATIONS

Kubiak, C. P.; Llorente, M.J; Lewis, N.S; Coridan, R.H; Beck, A.R. "Photoassisted high efficiency conversion of carbon-containing fuels to electricity" *Google Patents*, **2015**.

Kumar, B.; Llorente, M.J.; Froelich, J; Dang, T.; Sathrum, A.; Kubiak, C.P. "Photochemical and Photoelectrochemical Reduction of CO_2" *Chem. Commun.*, **2012**, *48*, 272-274.

Pastine, S. J., Okawa, D., Kessler, B., Rolandi, M., Llorente, M., Zettl, A., & Fréchet, J. M. "A facile and patternable method for the surface modification of carbon nanotube forests using perfluoroarylazides." *Journal of the American Chemical Society*, **2008**, *130*(13), 4238-4239.

ABSTRACT OF THE DISSERTATION

Electrochemistry and photoelectrochemistry in carbon cycle relevant energy systems

by

Mark Justin Llorente

Doctor of Philosophy in Materials Science & Engineering

University of California, San Diego, 2016

Professor Clifford P. Kubiak, Chair

To create fully sustainable energy systems requires multiple stages of engagement across different fields. The work presented in this dissertation represents a small survey of two major branches of sustainable chemistry – the improved efficiency for converting from renewably sourced fuels to power and the utilization of renewable sources of electricity to produce valuable chemicals from renewable carbon feedstocks. Electrochemistry and photoelectrochemistry are powerful tools for interconversion between chemical and electrical energy and for using light to drive chemical change.

Light can be used to overcome both the kinetic and thermodynamic barriers found in electrochemistry. In a proposed fuel cell device, the feasibility of using multi-

carbon fuels like n-hexane at ambient temperatures and pressures may be made possible by using light activated materials to overcome the kinetic barriers to fuel oxidation. The energy to produce the light may be sourced from the fuel cell itself and fed back into the oxidation process. In an electrolysis reaction, light may be used to drive the uphill reaction by creating sufficient photovoltage and photocurrent. In a paired electrolysis, CO_2 and a lignin derived substrate syringaldehyde are simultaneously upgraded using a customized photovoltaic device to drive both catalytic processes. In both of these implementations, electricity plays the crucial role of connecting light energy to chemical change and provides two examples where it can be used in sustainable chemical methods.

Chapter 1

Introduction to light driven and light assisted electrochemistry in the conversion of small molecules

1.1. Utilizing Light Energy in Electrochemical Processes

Global Energy

Light is the greatest driving force for change on Earth. Nearly all life on the planet derives its chemical energy from the sun whether directly through photosynthesis or indirectly through the consumption of other biological matter. In terms of total energy incident on the Earth, in a 24-hour period its surface receives an average of 2,143,000 terawatt-hours of irradiance.[1] For comparison, human activity was estimated at 155,505 terawatt-hours of commercial energy consumed for the year of 2012.[2] In that year, fossil fuels including petroleum, coal, and natural gas accounted for 86% of primary global energy consumed. The ~22% of fossil fuels not combusted is separated for use in waxes, lubricants, and petrochemical feedstocks.[3] As fossil fuels are a limited resource for which procurement and consumption come with environmental hazards, efforts to offset our dependence on them are being pursued by: (1) raising the efficiency of existing technologies, (2) increasing harvesting of renewable energy, and (3) developing sustainable chemical and industrial methods that use renewable carbon feedstocks to accommodate decreased use of fossil fuels.[4]

In overcoming our dependence on fossil fuels, we may find inspiration from recognizing that the chemical structures and stored energy that give value to these carbon rich materials originate from biochemical conversion of solar energy. Fossil fuels are derived from vast tracks of ancient plant and oceanic life aged for millions of years under high temperatures and pressures. While bioengineering and biomimicry are promising fields of study that may open new sustainable processes, as of today the implementation of these biological systems is limited in scope by low energy conversion efficiencies and high costs. Solar energy conversion to biomass fuels has been prohibitively inefficient and has been estimated to cap at about 10% conversion efficiency.[5] These processes cannot yet compete with the lower price point of extracting and refining fossil fuels for transportation and manufacturing without sustained government subsidizing.[6]

Electrochemistry

Fortunately, we are not limited to the materials and environmental constraints of biological methods. Alternative means for light-driven chemistry makes use of inorganic materials to overcome energetic, kinetic, and operational limitations. Among the methods best suited for converting light to chemical energy, electrochemistry and photoelectrochemistry provide expansive platforms for developing new reactions that use electricity to bridge light and chemical change. Electrochemistry takes advantage of a pervasive duality in nature; every natural process may be described as the pairing of an oxidation and a reduction. The challenge comes from implementing both halves effectively. In electrochemistry, these oxidations and reductions correspond to explicit charge transfers to and from electrodes that drive each of the half-reactions. Some of the benefits of electrochemical methods are as follows: (1) replacing sacrificial reductants

and oxidants with inert electrodes, (2) minimizing byproducts from sacrificial substrates, (3) controlling and tuning reaction rates via the manipulation of electrical current and voltage, (4) providing reaction pathways that may work at near ambient temperatures and pressures, and (5) compartmentalizing half-reactions into separate environments with different sets of products, though an ion bridge or membrane is typically required to separate compartments in order to minimize interactions between half-reactions.[7]

In principle we may combine any two complementary half-reactions to create a complete chemical process. Figure 1 below shows a generic diagram for an electrochemical electrolysis cell with a compartment separator and driven by a generic voltage source. On the left is the anode compartment wherein electrons are removed from species R_1 to form oxidized species O_1. On the right is the cathode compartment wherein electrons are transferred to species O_2 to form R_2. Electrons travel from the anode to the cathode and ions such as protons or electrolyte diffuse through the separator to compensate for the net change in charge. Examples in pairings of half-reactions will be discussed in Chapters 4 and 5.

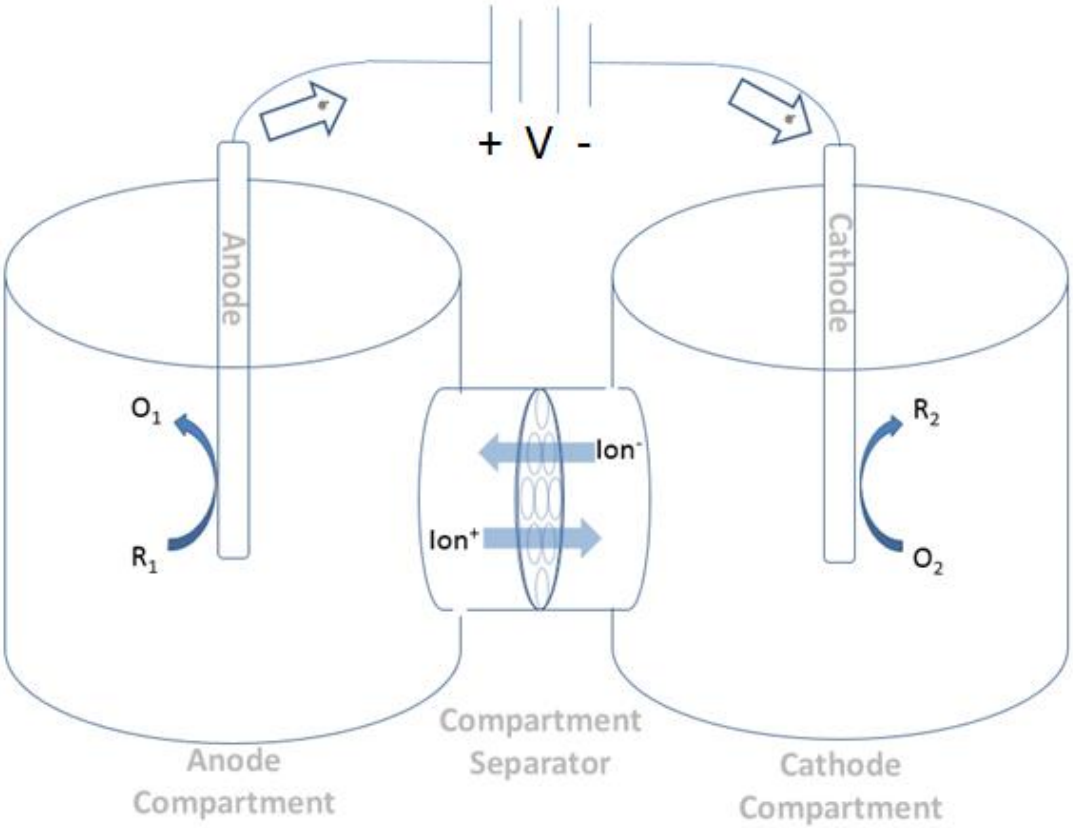

Figure 1-1 A basic diagram of an electrolysis cell as driven by a generic voltage source. The cell is composed of two main compartments each with its own electrode. As depicted, the species R_1 is oxidized to O_1 at the anode. The electrons from this half-reaction are driven by the voltage source to the cathode where they reduce O_2 to R_2. Positive ions drift to the right and negative ions to the left to compensate for this net flow of charge, though often one species is the main charge carrying ion such as with the use of proton exchange membranes. Ion species mobility through the separator is often selective based on the size of the ions and the separator material.

Photoelectrochemistry (PEC) describes the branch of electrochemistry that uses materials such as semiconductors and molecular dyes that are electrochemically active under illumination. These materials absorb photons to promote electrons from low lying energy states to higher ones leaving behind “electron-holes,” herein referred to as “holes.” The excited electrons may be transferred via downhill pathways to an electrical load such as a chemical reduction or recombine with holes releasing their remaining

energy as heat. Similarly, holes may drive a load such as a chemical oxidation or recombine with electrons. We will discuss the mechanisms that produce photocurrents and photovoltages in semiconductors in Sections 1.3 and 1.4, but it shall suffice to say that photons absorbed by these materials excite charges that are used in chemical reductions and oxidations.

As per Figure 1-1, we may generalize all electrochemical processes as performing simultaneous electron and hole transfers via electrodes called the cathode and anode, respectively. These electrodes may transfer charges directly to substrates or through mediators and electrocatalysts to perform chemical steps once they are reduced or oxidized to the appropriate oxidation states. Electrical power may be drawn or fed into chemical reactions depending on the spontaneity of the total reaction and the rate at which current is provided. For example, in galvanic cells and fuel cells, electricity may be drawn from a downhill chemical reaction by splitting it into its constituent half-reactions such as the pairing of a fuel or metal oxidation with the reduction of oxygen or metal cations. We may also drive an electrolysis cell with an applied voltage to perform uphill reactions. Since product selectivity and reaction rates are voltage dependent, we may set current densities and voltages to achieve maximal production rates or minimize energy costs. The only fundamental restriction when pairing two half-reactions is that current through the anode must match current through the cathode.

Regardless of the polarity of the voltage across a cell, the direction of current gives the designation of cathode or anode. Current direction is determined by the relative energy position of electrochemical potentials between the electrodes and the half-reactions coupled to them. An electrode will act as a cathode when it has a more negative

potential than the half-reaction coupled to it. This half-reaction potential is described by the Nernst equation, E1-1.

$$E = E^0 + \frac{RT}{nF}\ln\left(\frac{a_O}{a_R}\right) \simeq E^0 + \frac{RT}{nF}\ln\left(\frac{C_O^*}{C_R^*}\right) \qquad \textbf{E1–1}$$

This is the equilibrium potential for a half-reaction, i.e. with no current flowing into or out of the redox couple. E^0 represents the electrochemical potential at standard conditions. The terms a_O and a_R represent the thermodynamic activities or effective concentrations (C_O and C_R) of the oxidized and reduced species respectively. When activities for the two species are similar, we may conveniently approximate the ratio of their activity contributions by the ratio of their concentrations. As the concentration of oxidized species increases or the concentration of reduced species decreases, the potential for the redox couple becomes more positive which corresponds to a less negative potential required to reduce the oxidized species.

Faradaic current which is the current that is produced via charge transfers between electrodes and substrates is more than a function of the potential difference between electrode and bulk solution. When current is being drawn from or driven into solution at a constant applied voltage, a local change in concentration takes place near the heterojunction such that the local potential of the redox couple at the surface matches the applied potential at the electrode surface. A concentration gradient is formed in solution producing a net flow of redox species as described by equation E1-2. In the case of cathodic charge transfers, reduced species are formed at the heterojunction and diffuse away from the electrode while oxidized species diffuse toward it. The slope of the concentration gradient is proportional the flux of redox species and thus proportional to

the electrical current density. One may increase the chemical potential gradient and therefore maintain higher current densities through enhanced mass transport like stirring of the solution so that redox species diffusion to or from the electrode is not the rate limiting step.

$$J = \frac{Current}{Electrode\ Area} = nFD_{analyte}\frac{dC_{analyte}}{dx}|_{x=0} \qquad \textbf{E1-2}$$

An important method for controlling mass transport of analytes and probe charge transfer kinetics is rotating disk electrochemistry. In standard rotating disk electrochemistry, a flat circular electrode material is spun in solution about its vertical axis. This rotation stirs the solution below causing a flow of solution volume toward the electrode center and over its surface. So long as the flow remains non-turbulent, electrical current at the central disk electrode may be predicted by the Levich Equation, E1-3, where mass transport limited current is a function of electrode area A, and the square root of rotation rate, ω.

$$I = 0.620\, nFAD^{\frac{2}{3}}\nu^{\frac{1}{6}}\omega^{\frac{1}{2}}C \qquad \textbf{E1-3}$$

In one important variant of this technique, rotating ring disk electrochemistry, or RRDE, we have a second electrode in the shape of a ring that may be set to a different potential from the disk. As solution flows over the disk electrode, it subsequently travels over the ring. A charge transfer event may take place at the disk and be followed by a charge transfer event at the ring. After normalizing currents to the number of electrons in their respective half-reactions, n_r and n_d, the ratio of ring current and disk current will remain constant regardless of rotation rate, though its value will always be less than unity due to diffusion losses. This current ratio is given as a function of their geometries which

may be calculated using a series of equations, E1-4 and E1-5. A general RRDE electrode apparatus is pictured below in Figure 1-2.

$$N_{Theoretical} = 1 - \sigma_{OD}^2 + \sigma_B^{\frac{2}{3}} - G(\sigma_C) - \sigma_B^{\frac{2}{3}} G(\sigma_A) + \sigma_{OD}^2 G(\sigma_C \sigma_{OD}^3) \qquad \textbf{E1-4}$$

$$G(x) = \frac{1}{4} + \left(\frac{\sqrt{3}}{4\pi}\right) \ln\left[\frac{\left(x^{\frac{1}{3}}+1\right)^3}{x+1}\right] + \frac{3}{2\pi} \arctan\left[\frac{2x^{\frac{1}{3}}-1}{\sqrt{3}}\right] \qquad \textbf{E1-5}$$

$$\sigma_{OD} = \frac{ring\ outer\ diameter}{disk\ diameter}, \qquad \sigma_{ID} = \frac{ring\ inner\ diameter}{disk\ diameter}$$

$$\sigma_A = \sigma_{ID}^3 - 1, \qquad \sigma_B = \sigma_{OD}^3 - \sigma_{ID}^3, \qquad \sigma_C = \frac{\sigma_A}{\sigma_B}$$

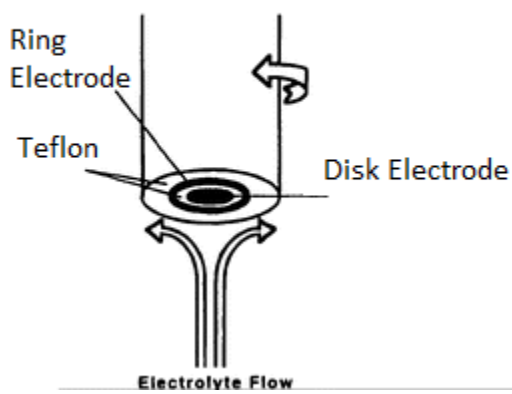

Figure 1-2 A generic rotating ring disk electrode shaft and the flow of solution over its surface. The ring and the disk are separate electrodes that may be made of different materials and held at different potentials. Rotation creates a flow of solution from the bulk to the center of the electrode and out radially past the ring electrode. Substrates may undergo sequential electron transfers first at the disk and secondly at the ring. Image taken from Collman, and Decreau, "Functional biomimetic models for the active in the respiratory enzyme cytochrome c oxidase".[8]

The physics describing photovoltaics are analogous to those describing solution phase redox chemistry. The first photovoltaic was itself a solution phase electrochemical cell.[9] Because of this congruity, photovoltaics and semiconductor photoelectrodes are

highly compatible technologies for pairing with electrochemical reactions so as to minimize the steps for converting light irradiance to electrical power or electrical power to chemical change. Section 1.3 will relate the electrochemical potentials within a semiconductor to the previously described Nernst potential in more detail.

1.2 Current Applications in Electrochemistry – Synthesis and Fuel Cells

Large scale commercial electrochemical processes have long been staples of the chemical industry. The Chloralkali process uses NaCl rich water to form chlorine gas, hydrogen gas, and NaOH, three chemical precursors that play critical roles in other synthetic processes.[10] Aluminum metal was once so difficult to produce that it was as valued as silver, a history evidenced by the 8.9 inch aluminum pyramid capping the Washington Monument and the aluminum dinnerware of Napoleon III.[11] With the invention of the Hall-Héroult process which produces aluminum from reduction of molten ore and oxidation of carbon feedstocks, aluminum has become a disposable household commodity. With regard to organic synthesis, some commercial processes have already been shifted to electrochemical methods including the production anthraquinone, perfluorinated hydrocarbons, and adiponitrile synthesis which is a precursor for nylon fibers and resins. Table 1-1 contains a selection commercial electrochemical processes and the companies that own them.

Table 1-1 A list excerpt outlining commercial products electrochemically manufactured and the companies that use these processes. Original list found in "Electrochemical Manufacturing in the Chemical Industry" by Gerardine G. Botte [7]

Product	**Starting Material**	**Company**
Acetoin	Butanone	BASF
Acetylenedicarboxylic acid	1,4-Butynediol	BASF
Adipoin dimethyl acetal	Cyclohexanone	BASF
Adiponitrile	Acrylonitrile	Monsanto (Solutia), BASF, Asahi Chemical
4-Aminomethylpyridine	4-Cyanopyridine	Reilly Tar
Anthraquinone	Anthracene	L. B. Holliday, ECRC
Azobenzene	Nitrobenzene	Johnson Matthey Company
p-t-Butylbenzaldehyde	p-t-Butyltoluene	BASF, Givaudan
L-Cysteine	L-Cystine	Wacker Chemie AG
1,4-Dihydronaphthalene	Naphthalene	Clariant
2,5-Dimethoxy-2,5-dihydrofuran	Furan	BASF
Hexafluoropropyleneoxide	Hexafluoropropylene	Clariant
m-Hydroxybenzyl alcohol	m-Hydroxybenzoic acid	Otsuka
p-Methoxybenzaldehyde	p-Methoxytoluene	BASF
Perfluorinated hydrocarbons	Alkyl substrates	3M, Bayer, Clariant
Salicylic aldeyde	o-Hydroxybenzoic acid	India
Succinic acid	Maleic acid CERCI,	India
3,4,5-Trimethoxytolyl alcohol	3,4,5-Trimethoxytoluene	Otsuka Chemica

Nearly all of these processes use fossil fuels either explicitly as a reactant or implicitly as an energy source. To perform sustainable electrochemistry, the sourcing of reactants and energy must be renewable and performed with minimal detriment to the environment. With regard to small molecule carbon feedstocks such as methane and

methanol, reforming of organic material at high temperatures and pressures is already a widely used method for converting organic matter into a mixture of products.[12] One example is the Fischer-Tropsch process which uses a mixture of CO and H_2 called syngas to create synthetic oils and fuels with average molecular weights and chain lengths set by the temperature and pressure of the reactor.[13] Other methods that maintain the integrity of organic reactants such as aromatic rings which will be further discussed in Chapters 4 and 5.

CO_2 is the primary pollutant that we wish to mitigate from human activity. Engineers in Germany have produced a pilot plant that uses solar energy to convert atmospheric CO_2 into liquid fuels using a series of established steps: CO_2 sequestration by thermal cycling of adsorption polymers, water reduction to H_2, reverse water-gas shift to take CO_2 and H_2 to CO and H_2O, and a method similar to Fischer-Tropsch to form a synthetic diesel.[14,15] 70% has been put forth as an efficiency value for the solar energy conversion efficiency for their process, but it is unclear if this includes the full energy costs associated with CO_2 sequestration, heating of reactors, and electrical costs. Further improvements for future plants of this type will come from less energy intensive sequestration methods and electrocatalysts with lower energy demands for the same rates of CO_2 reduction.

Few heterogeneous CO_2 reduction electrocatalysts have garnered as much interest as pure copper metal in aqueous solutions. While most catalysts are selective for a two-electron reduction product such as CO, formate, or oxalate, copper metal can reduce CO_2 to higher order products including the multicarbon species ethylene, a feedstock in polymer synthesis.[16,17] Selectivity for various CO_2 and proton reduction products is set by

the potential of the copper electrode where higher order reduction products tend to form at more negative reduction potentials as may be visualized in Figure 1-3 below. Like the Fischer-Tropsch process, one cannot choose to produce a single product, but by setting a voltage one may choose a particular profile of CO_2 reduction products.[18,19]

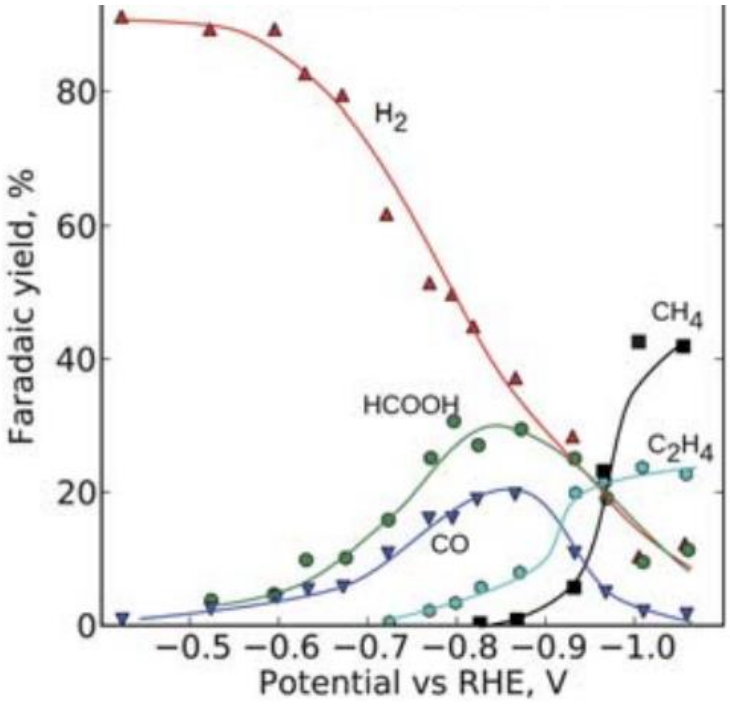

Figure 1-3 Faradaic yield for planar polycrystalline copper in the reduction of CO_2 in aqueous media. All potentials are referenced to RHE, regular hydrogen electrode, so that values are pH independent. Hydrogen is produced at less negative potentials but two electron CO_2 product rates increase with more negative potentials until methane and ethylene become the dominant products around -0.95 V vs RHE. Image taken from Peterson, et al. from "How copper catalyzes the electroreduction of carbon dioxide into hydrocarbon fuels".[19]

The hydrogen fuel cell is the most commercially used electrochemical power conversion method for transportation, but hydrogen suffers inherent issues with storage and transport due to being a gas at ambient conditions which increases energy costs of storage and limits vehicles to regions of close proximity to hydrogen refueling.[20] Alternatives to hydrogen include many small molecule fuels such as methanol, and

formate. While these may hold a higher volumetric energy density than hydrogen and are readily dissolved in solution, they suffer from practical setbacks in a fuel cell implementation such as fuel crossover wherein methanol or formate at the anode compartment diffuses through the membrane and enters the oxygen rich cathode compartment where it is directly consumed by oxygen, its energy wasted as heat.[21,22] Larger molecules are not as susceptible to fuel crossover but suffer from the formation of highly stable oxidation intermediates that precede necessary oxidation steps such as C-C and C-H activation.[23,24] These intermediates impose barriers to further oxidation. In order to overcome these barriers energy must be redirected back into the system usually in the form of heat. The Haile group from Caltech has developed a fuel cell that takes advantage of heat given off during the operation of the fuel cell in order to maintain an operational temperature of ~240°C, but due to the high temperature of this cell and the heat that must first be provided to it to begin operation, applications are at present limited.[25,26]

Light may also be used to overcome kinetic barriers. n-TiO_2 is a well-established and stable high band gap semiconductor and photoelectrocatalyst. The valence band of TiO_2 is mostly of oxygen 2p in character.[27] Under illumination from near-UV radiation with photon energy >3.0eV, powerful oxidizing holes are excited that spontaneously drift to the surface where they are capable of oxidizing most organic material to CO_2 in the presence of oxygen or water, a process called mineralization. Many implementations of light driven electrochemical devices using high band gap semiconductors to oxidize substrates exist in the literature, some of which describe their devices as fuel cells or energy scavenging pollutant oxidizers.[28-31] While electricity is obtained from these devices, the sourcing of light energy must be accounted for. For example, should one

rely on solar UV radiation, UV radiation represents only 3% of the solar flux due to atmospheric absorption. Utilizing solar energy for large band gap semiconductors would be prohibitively slow and limited to daylight hours. Should artificial light sources be used, one must take into account the energy costs associated with illumination from that source. Many photo fuel cell schemes perform at an energy deficit in great part because they rely on all oxidative current to be produced through illumination of the photoanode or fail to report an efficiency with total energy input included.[32,33] Further investigation in schemes that can obtain current from fuels in excess of the traditional photocurrent will be discussed in Chapters 2, 3, and 5.

1.3 Introduction to Semiconductor Photoelectrochemistry

A simple assumption for photoexcitations is that photons have energies greater than the material band gap in order to excite charges. Each pair includes two charges, the negatively charged electron and the positively charged hole. Though two charge carriers are excited per absorbed photon, the net current is equivalent to one charge carrier per photoexcitation. To illustrate this, one may imagine the extreme scenario wherein electrons and holes have drastically different mobilities within the material. If electrons are mobile but holes are localized, the photocurrent would be predominantly made of electrons that would drive a load, complete the circuit, and recombine with the localized holes. In the more general case where both photoexcited charges are mobile, both majority hole and majority electron currents will traverse the circuit in opposite directions until they reach a region that is rich with the opposite charge carriers as depicted in Figure 1-4 below. In other words, when a current carrying a majority electrons meets a

current composed of a majority holes they create a region of simultaneously high concentrations of both charges that are in excess of the thermal equilibrium. This high concentration of both leads to immediate recombination of these charges.

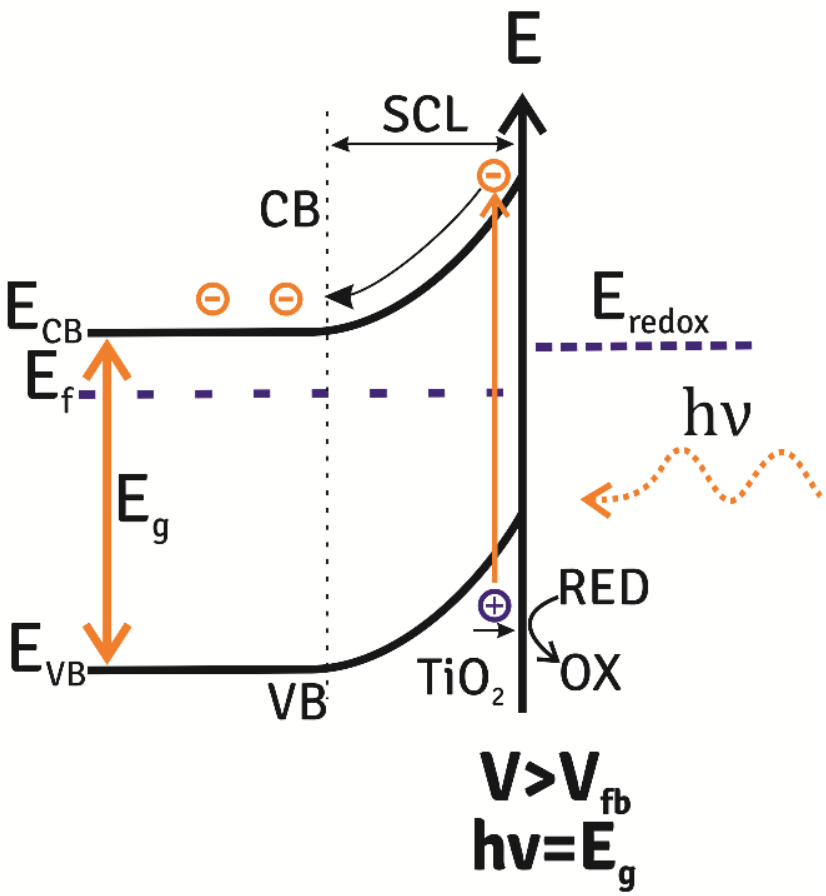

Figure 1-4 Band bending in the depletion region of an n-type semiconductor in contact with solution forces electrons near the surface into the bulk and holes in the depletion region to the surface. Photoexcitation is the primary source of the minority carrier, holes. Image taken from Bessegato, Guaraldo, and Zanomi, "Enhancement of Photoelectrocatalysis Efficiency by Using Nanostructured Electrodes."[34]

Charge counting of this kind is an important consideration when regarding the power and current one can generate from these processes. The power delivered by a photovoltaic, galvanic cell, or fuel cell is given by the current multiplied by its voltage. As such, the incident photon to current efficiencies and quantum yields are useful metrics

for evaluating power conversion from photoelectrochemical systems. Incident photon to current efficiency is an easily measured value that expresses the percent of photons incident to the semiconductor that create photocurrent carrying charges. Quantum yield refers to the ratio of current-carrying charges to the amount of absorbed photons. In practice, IPCE is a more practical figure of merit when considering the total energy conversion of the system. Low IPCE values may arise from low absorptivity or high non-radiative recombination. As an example, hematite related materials α-$Fe_2O_{3-x}S_x$ whose band gaps may be tuned from 1.4-2.2 eV by varying oxygen and sulfur content show promise as solar spectrum absorbers and photooxidizing electrode materials but tend to give low IPCE and QY values due to their high density of localized recombination sites and low charge mobility which prevent photoexcited electrons and holes from separating even under heavy biasing.[35]

$$IPCE = \frac{photocurrent}{total\ incident\ excitation\ light} \times 100\% \qquad \textbf{E1-6}$$

$$QY = \frac{photocurrent}{rate\ of\ absorbed\ photons} \qquad \textbf{E1-7}$$

Similar to the Nernstian potential for a redox species in solution, a location dependent thermodynamic potential exists within semiconductors called the Fermi level, E_F. There are many nuanced uses of the term “Fermi level” within physics, electrical engineering, and electrochemistry, but for the purpose of this discussion we will refer to the Fermi level as the total electrochemical potential for charges within a material as measured against an external reference. Much as with the Nernst potential where the electrochemical potential can be used to determine the ratio of reduced to oxidized species, the Fermi level can be used to determine the ratio of concentrations for electrons

and holes as given by equations E1-8 and E1-9. N_C represents the effective density of states accessible to electrons in the conduction band E_C and N_P the effective density of states accessible to holes in the valence band E_V. k is the Boltzmann constant and T is the temperature.

$$n = N_C \exp\left(-\frac{E_C - E_F}{kT}\right) \qquad \textbf{E1-8}$$

$$p = N_V \exp\left(\frac{E_V - E_F}{kT}\right) \qquad \textbf{E1-9}$$

In an ideal semiconductor with zero defects, the Fermi level would reside almost directly between the conduction and valence bands described in equation E1-10 below. The concentration of thermally excited electrons would be matched by an equivalent number of thermally excited holes. We call a material whose properties approach an idealized defect free charge concentration "intrinsic." One may add defects to adjust charge concentrations, namely dopants, to a semiconductor with electron donors or electron acceptors. Electron donors have an equivalent valency of +1 with respect to the intrinsic material and lead to n-type. These orbitals correspond to localized singly-occupied electronic states that reside just below the conduction band and whose electrons are easily promoted to the conduction band by thermal excitation. Electron accepting dopants have a valency of -1 with respect to the intrinsic semiconductor and correspond to localized singly-unoccupied orbitals that reside just above the valence band and are easily populated by thermally excited electrons from the valence band and lead to p-type. These electrons leave behind valence band holes. In some materials such as TiO_2, vacancies such as lower than stoichiometric oxygen lead to a higher than intrinsic electron concentrations in the conduction band.

Unlike the Nernst potential, we have spatially dependent considerations specific to solid state materials that affect the equilibrium Fermi level within a semiconductor. These effects are summed up in the term V(x) which includes voltage offsets due to applied potentials, capacitance, and surface charges but also the built in potential which is a function of position.

$$E_F = \left[\frac{E_C+E_V}{2} + \frac{kT}{2}\ln\left(\frac{m_h^*}{m_e^*}\right)^{\frac{3}{2}}\right] + \frac{RT}{F}\ln\left(\frac{n_{electrons}}{n_i}\right) + V(x) \qquad \textbf{E1-10}$$

$$= [E^\circ{}_{intrinsic}] + \frac{RT}{F}\ln\left(\frac{n_{electrons}}{n_i}\right) + V(x)$$

$$n_i = \sqrt{N_C N_V \exp\left(-\frac{E_{bandgap}}{kT}\right)} \qquad \textbf{E1-11}$$

While similar in form to the Nernst equation, it must be noted that E_C and E_V are not explicitly referenced to a potential. While their energy positions with respect to each other are determined by the band gap energy, $E_{bandgap}/e$, their positions relative to a reference potential are subject to change due to external voltages included in V(x) as well as material specific effects such as the composition and orientation of atoms at the electrode surface. For example, for compound semiconductors made from multiple elements, varying the electrolyte by pH changes ion adsorption on the surface creating changes in the capacitance that offset the relative positions of the band edges.[36] Due to these complications, in practice when attempting to determine the position of band edges it is best to use experimental methods which will be discussed in Section 1.4.

Similar to the Nernst equation, altering charge concentrations shifts the Fermi level higher or lower with respect to the band edges in much the same way as adding

reductants or oxidants to a solution with redox species; however, because of the stationary nature of dopant atoms, the dopant ions remain fixed in the semiconductor. When the donated mobile charges are drawn elsewhere, the ions are left behind creating a fixed charge that produces an electric field that resists further loss of mobile charges as consistent with equation E1-12. This resulting field is exploited in photovoltaics, photodiodes, and photoelectrodes to direct photoexcited charges in opposite directions and produce a photocurrent before they can recombine. Below is a potential diagram depicting the energy positions of band edges for various semiconductors at a pH of 1.

$$-\frac{d^2}{dx^2}V_{electric} = \frac{d}{dx}Electric\ Field = \varepsilon_0\rho_{uncompensated\ dopant\ ions} \qquad \textbf{E1-12}$$

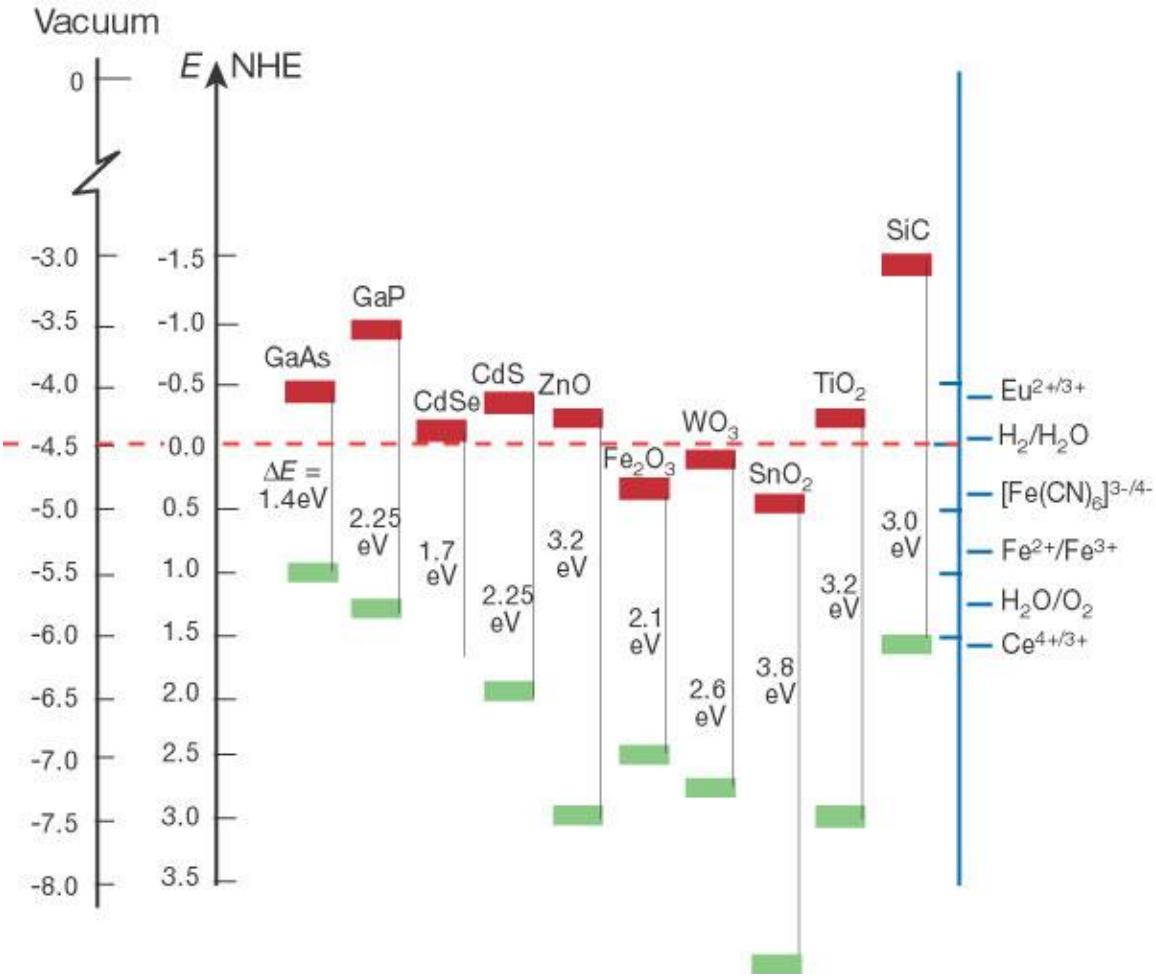

Figure 1-5 Semiconductor band edges at pH 1 with respect to NHE and vacuum level without external biasing. The band edges of compound semiconductors shift with pH as a function of ion absorption on their surfaces. Some of these values are only calculated from known shifting trends because of instability in acidic media. Image taken from "Photoelectrochemical cells" authored by Michael Grätzel.[9]

We may look to an example of a semiconductor-liquid heterojunction formed when a photoelectrode is placed in solution. As depicted in Figure 1-6 below, before a heterojunction is formed a voltage difference exists between the Fermi level of the semiconductor and the Nernst potential of the redox species in solution. In this example, the n-type semiconductor's Fermi level is higher in energy than the redox couple. Once the junction is formed, charges spontaneously flow from the semiconductor into the

redox couple until equilibrium is reached. At the heterojunction, negative ions in solution accumulate near surface to compensate for the positive fixed charge that remains in the semiconductor. Equilibrium is reached when the electrochemical potential throughout the whole system is flat and constant.

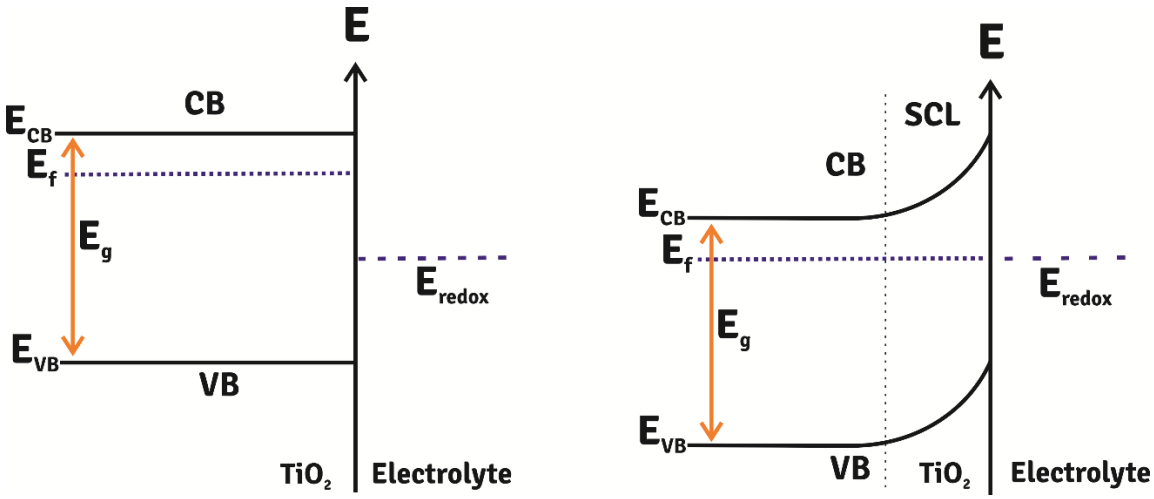

Figure 1-6 Semiconductors and solution before and after a heterojunction is formed and equilibrium reached. Before charge transfers occur, the electrochemical potential of the semiconductor E_F is more negative than the redox potential E_{redox}. Upon contact, electrons flow from the semiconductor to the redox couple forming the depletion region where band bending occurs. Equilibrium is reached when the electrochemical potential across all points is constant. Image taken from Bessegato, et al.[34]

A counterintuitive feature of this equilibrium is that an electric potential remains. In solution with no applied electric potential, should cations and anions be spatially separated, an electric field from the ions would persist that would draw ions of opposite charge to each other until no net charge gradient persists. No long range electric fields or potential gradients would be expected at equilibrium. Within the semiconductor, the built in field cannot be relieved through ion drift. To accommodate this field and still maintain equilibrium one may note that there are multiple terms contributing to the electrochemical potential within the semiconductor. Unlike the Nernst equation with only

one variable term that offsets the potential, the Fermi level equation explicitly contains spatially dependent electric and chemical potentials. As the electric potential changes in the depletion region, an equal and opposite potential change occurs in the chemical potential of electrons and holes as described by E1-10. The Fermi level remains flat. The built in potential is revealed not in the Fermi level but in the raising and lowering of band edges whose positions are a direct function of the electrical potential term and not a direct function of band occupancy.

While the built in potential serves as a useful metric to describe the electric potential that an electrode may deliver to a photoexcited charge, it is not itself the photovoltage. Photovoltage is produced when there is a difference in Fermi levels between the bulk and surface due to the accumulation of photoexcited charges. In other words, a photovoltage is due to a chemical potential increase, not electric. Under illumination, charges are added in excess of equilibrium. While photoexcitation does not directly affect the electric potential, it increases the chemical potential of electrons and holes. When electrons and holes are no longer in equilibrium with each other, their Fermi levels effectively separate producing two distinct electrochemical potentials for each species. These levels are described as the quasi Fermi levels for electrons and holes. As one may note from the Fermi level equation, a chemical potential varies linearly with the natural log of charge concentration. In an electron rich n-type material, an increase in electrons due to photoexcitation may have minimal effect on the electron quasi Fermi level, but the local increase in holes may yield a much larger shift in the hole quasi Fermi level. In general, in illuminated and sufficiently doped semiconductors the photovoltage is due to a change in the minority carrier's quasi Fermi level. Under low illumination or

uninhibited charge transfer from the electrode, photoexcited charges cannot accumulate and quasi Fermi levels remain close to the equilibrium Fermi level. This condition is referred to as the short circuit condition where photocurrent is produced but no photovoltage.

Photovoltage arises when photoexcited charges accumulate after separation. This photovoltage creates additional driving force for charge transfers to solution and therefore increases the faradaic current. This accumulation occurs when there is hindrance to charge transfers out of the electrode whether due to slow charge kinetics or lack of substrate to accept the minority carriers at the surface. In a well-constructed photoelectrode, the back contact provides little to no kinetic barrier for charge transfer out of the electrode, so charge accumulation should only occur near the surface. Under accumulation, minority carrier concentrations increase within the depletion region which leads to a decrease in the magnitude of the built in potential. Accumulated minority carriers alleviate the fixed charge of dopant ions which in turn reduces the magnitude of the built in potential and strength of the built in field that separates photoexcited charges. A large photovoltage corresponds to a large quasi Fermi level splitting and reduced band bending. Given a sufficient decrease in the built in potential, minority carriers near the surface persist long enough to diffuse back to the majority carrier rich region where they recombine with majority carriers thus decreasing the photocurrent. This behavior may be illustrated in the photocurrent-voltage behavior in Figure 1-7. As one would expect from Equation E1-13, whether through applied potentials or photovoltage, as the built-in potential is decreased, a sharp decrease in photocurrent will take place when the built in potential approaches zero.[37-39]

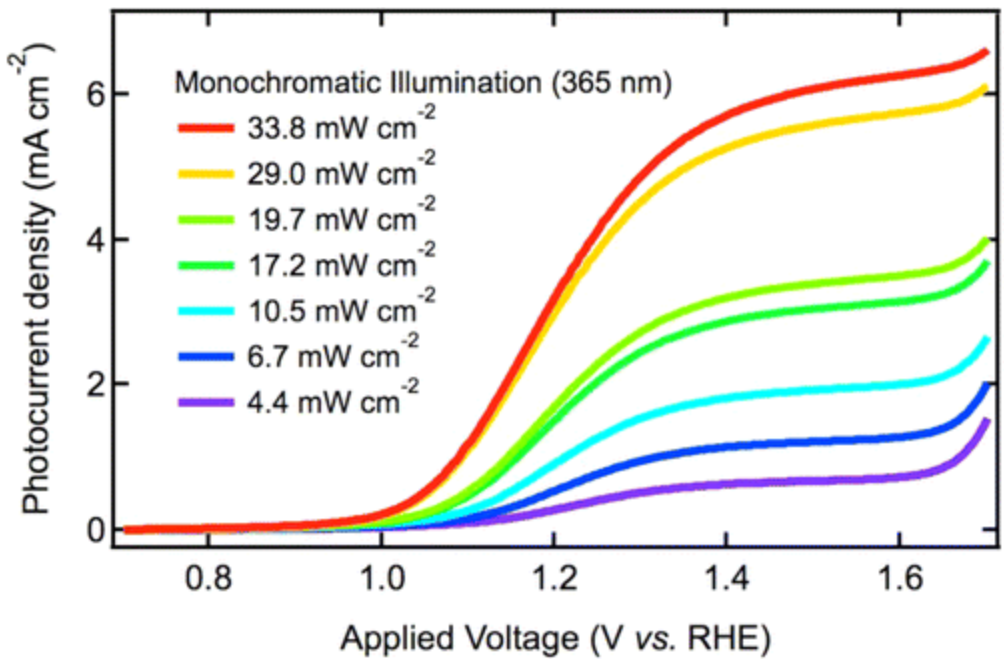

Figure 1-7 Current voltage behavior of a hematite Fe_2O_3 electrode in 1 M NaOH in aqueous media under increasing illumination. Photocurrent scales linearly with excitation intensity and begins to plateau at more anodic potentials. Recombination dominates at cathodic potentials until photocurrent diminishes to zero. Figure taken from "Rate Law Analysis of Water Oxidation on a Hematite Surface" by Le Formal, et al.[40]

$$I_{Faradaic} = Light\ Intensity \times N(V_{built-in}) \times (1-\rho) \qquad \textbf{E1-13}$$

$$N(V) = \frac{\left[1-\beta(V_{\mathrm{built-in}})\left(1-\frac{L_K}{L_K+L_\epsilon}\right)\right]}{\left[1+\frac{\kappa}{k'_\Sigma c_0}+\frac{k_1 L_K}{k'_\sigma \exp(V_{built-in})}\right]} \qquad \textbf{E1-14}$$

In equation E1-14, N represents the collection efficiency of photoexcited charges, ρ is the fraction of excited charges lost to surface recombination, and β is the fraction of light absorbed outside of the depletion region as given by exp(-W/L_ϵ) where W is the voltage dependent width of the depletion region and L_ϵ is the absorption length for photons through the semiconductor. L_κ is the bulk diffusion length of minority carriers. The term κ represents the fraction of minority carriers lost to recombination within the diffusion layer, c_0 is the concentration of minority carriers at the electrolyte interface, k_1

is the recombination rate due to mid gap trap states, and k'_{Σ} represents the rate of all heterogeneous charge transfers of minority carriers out of the electrode. $V_{built\text{-}in}$ represents that total band bending in the depletion region of the electrode. As one may expect under high band bending, charge collection efficiency N approaches a plateau near 1 and under low band bending approaches 0.

1.4 Current-voltage behavior in Fermi level pinned and unpinned semiconductors

The previous discussion of semiconductor electrochemistry serves as a basic framework for describing the phenomena that dictate semiconductor electrode behavior. Many kinetic parameters can affect the overall photoelectrode behavior of an electrode in solution. One should expect band positions, charge transfer rates, and band bending to be functions of the electrode composition as electrode fabrication as well as externalities such as electrolyte, substrate concentrations, and ion adsorption. The results of this large collection of variables may be difficult to predict but often follow reliable trends related to the nature of the interface. For example band edges of compound semiconductors predictably shift in energy position due to pH or other variances in electrolyte concentrations. In practice values such as band edge position and built in potential are best characterized through measurements specific to the experimental conditions.

To perform reliable electrochemical measurements on a semiconductor electrode, it must be constructed such that only its active surface is available to solution and the semiconductor back contact produces minimal resistance to current. Most semiconductor electrodes are created from single crystalline planar materials or thin films attached to conductor leads through low resistance contacts called ohmic contacts. An ohmic contact is formed when a conductive material such as a metal has an unbiased Fermi level nearly

matched to that of the doped semiconductor. A simple approximation of this follows Anderon's rule wherein one may approximate the unbiased Fermi levels of metals and n-type semiconductors by their electron affinities or p-type materials by their ionization energies, but this does not always follow as surface dipoles may form at the interface creating an induced mismatch in Fermi levels. When the conductor Fermi level and semiconductor Fermi level are poorly matched, charges flow between the two materials until a depletion region is formed in the semiconductor of the same nature as that produced at the semiconductor-electrolyte heterojunction.[41] This depletion region reveals itself in undesirable non-linear resistance.

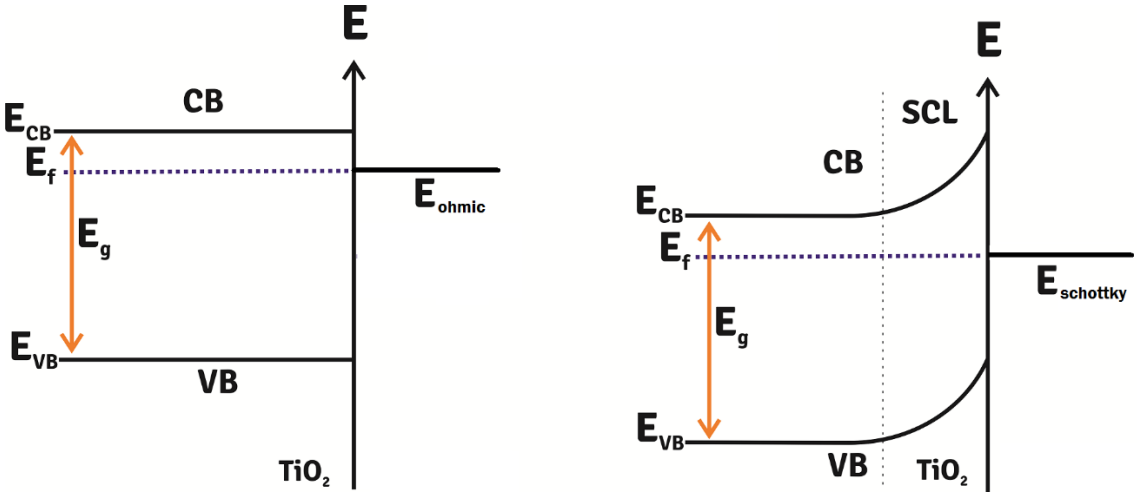

Figure 1-8 Ohmic contact vs Schottky barrier. On the left, when the Fermi levels of a semiconductor and a conductor are well matched, little to no depletion region is formed leading to a minimal barrier to charge transfer in both directions. When the Fermi level of the conductor lies within the band gap, a depletion region is formed leading to diode-like electrical behavior and a built in potential as previously described. Image edited from Bessegato, et al.[33]

One may easily determine if a contact is ohmic by testing for a linear resistance through the contact. By creating two separate contacts to the semiconductor, one may create a conductor-semiconductor-conductor series. Current vs voltage may then be

measured across the two contacts with the semiconductor as the electrical load. With no Schottky barriers, resistance should be constant and current should show no hysteresis. Hysteresis loops in voltage cycling indicate charging and discharging of trap states formed at the heterojunction.

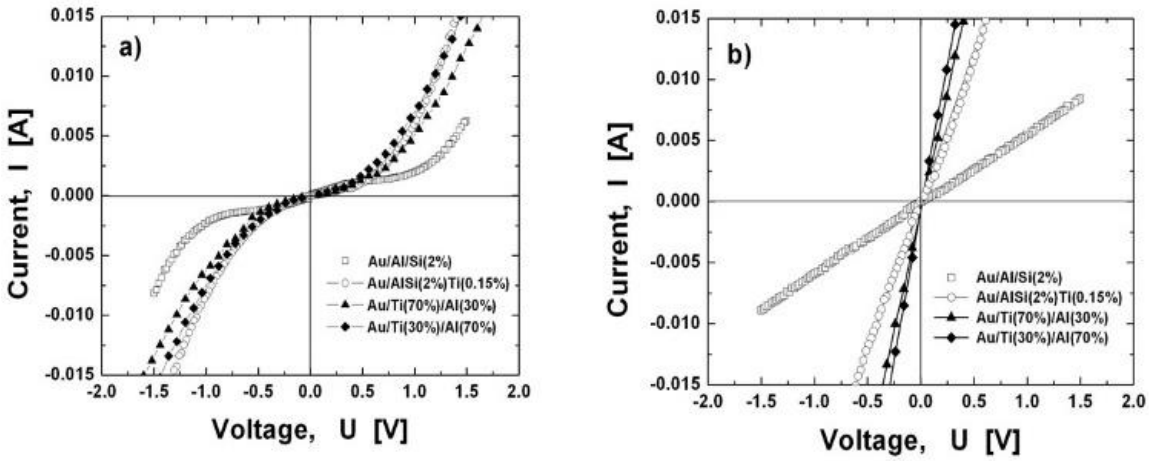

Figure 1-9 Measured current versus voltage behavior before and after annealing of contact materials to a p-Si semiconductor. Figure taken from Kolaklieva and Kananakov, "Ohmic Contacts for High Power and High Temperature Microelectronics."[42]

In attempting to measure the conduction and valence band edges at the electrode surface when coupled to solution, one may approximate the conduction band edge of n-type materials and valence band edge of p-type materials with the Fermi level. When the applied potential and the surface Fermi level are equal, the depletion region disappears and there is no band bending. This condition called the flat band potential corresponds to the applied potential at which photocurrent first appears. Semiconductor electrodes exhibit capacitive current and dark photocurrent which may obfuscate the exact position. Light chopping while performing a potential sweep is one method for elucidating the

point at which photocurrent onset begins as shown in Figure 1-10.

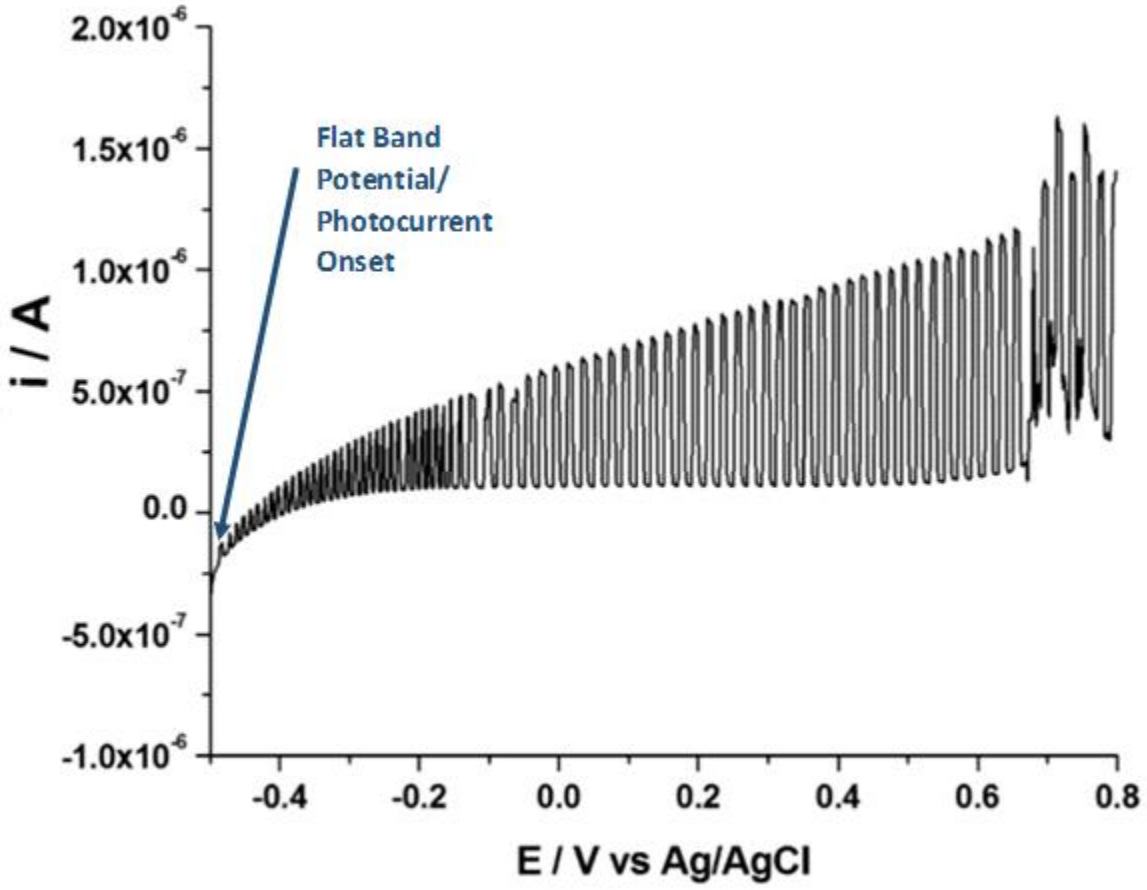

Figure 1-10 Linear sweep voltammetry recorded in 0.1 M phosphate buffer,·pH 7, 0.1 mM hydrazine under chopped UV light using a TiO_2 nanowire array. The flat band potential is reached when the difference between photocurrent and dark current is reduced to zero. Image taken from "Arrays of TiO_2 Nanowires as Photoelectrochemical Sensors for Hydrazine Detection" by Michael Ongaro, et al.[43]

Another method for determining the Fermi level at the surface is through Mott Schottky plots wherein a small alternating voltage is applied during a slow voltage scan. The response to the alternating voltage determines the capacitance of the electrode-solution hetereojunction. In the potential regime wherein there remains a significant built in potential, the dominant term in capacitance is a function of built in potential such that $1/C^2$ is proportional to the voltage minus the flat band potential as given by Equation E1-

15. At ambient temperatures, one may find the flat band potential by extrapolating from this linear region toward the x-axis and subtracting 25.9 mV from this result as depicted by the Mott Schottky plot in Figure 1-11.

$$\frac{1}{C^2} = \frac{2}{\varepsilon\varepsilon_0 N_0 F}\left(V - V_{flat\ band} - \frac{RT}{F}\right) \qquad \textbf{E1-15}$$

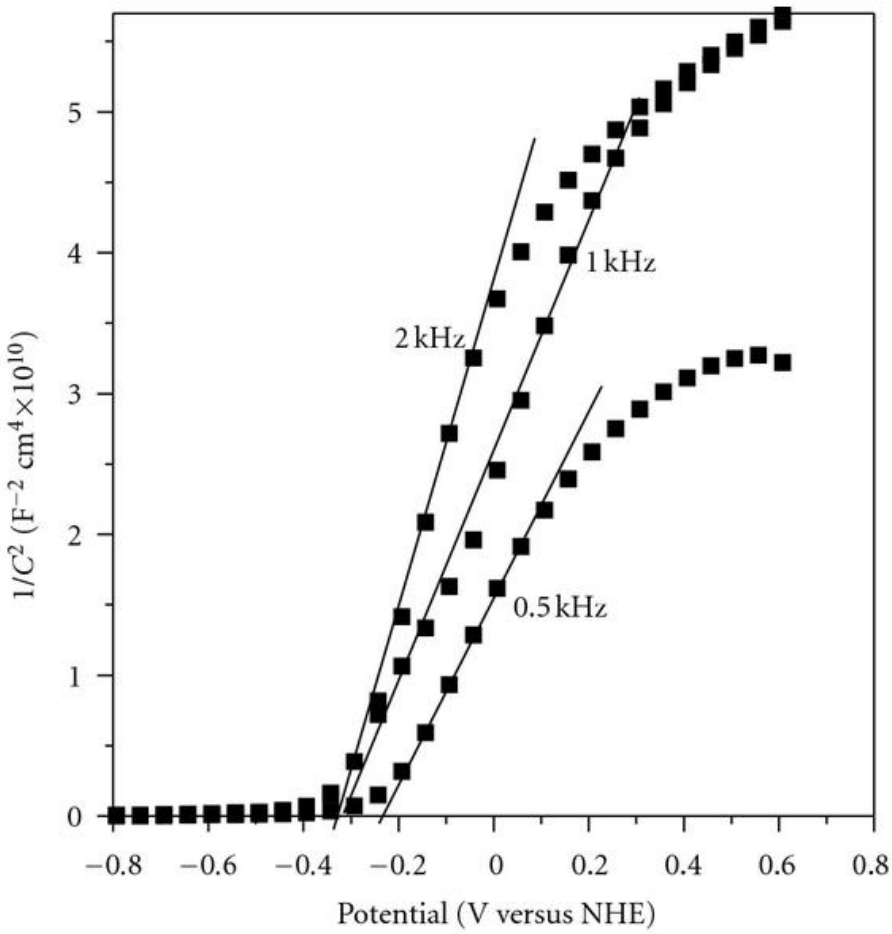

Figure 1-11 A Mott Schottky plot showing the linear regions and flat band potentials vs NHE for a nanoparticle-film TiO_2 electrode. The dispersion in measured band edge positions is attributed to frequency-dependent capacitance on non-planar electrodes wherein lower frequencies may better represent the true flat band potential. Image taken from "(Photo)electrochemical Methods for the Determination of the Band Edge Positions of TiO_2-Based Nanomaterials" by Radim Beranek.[36]

A useful deviation from previously discussed semiconductor electrode behavior arises in a phenomenon called Fermi level pinning. It should be noted that some literature calls this behavior "unpinning" with respect to redox couples in solution, but for the duration of this discussion we will refer to this same phenomenon as the pinning of the Fermi level to a particular set of surface states. A material's surface often differs in electronic character from the bulk. Surface atoms undergo uncompensated strain from a different bonding environment. This may also result in dangling bonds, localized radical orbitals, that act as charge traps or active binding sites for species in solution. Energy position of these states usually lies near the middle of the material's band gap, and while a small surface concentration of them may account for slight deviations toward intrinsic material concentrations near the surface, with as few as $10^{12}/cm^2$ of mid gap surface states the surface begins to act nearly metallic in character.[44,45] In semiconductors such as p-Si, this leads to band bending that is identical in behavior to semiconductor-metal heterojunctions as previously discussed. The net effect is that the surface potential is allowed to vary over a wide range of potentials while the bulk semiconductor acts as a constantly biased photodiode. This means that for a given illumination and for a large range of applied potentials, current vs. applied potential is shifted by this photovoltage as in Figure 1-12.

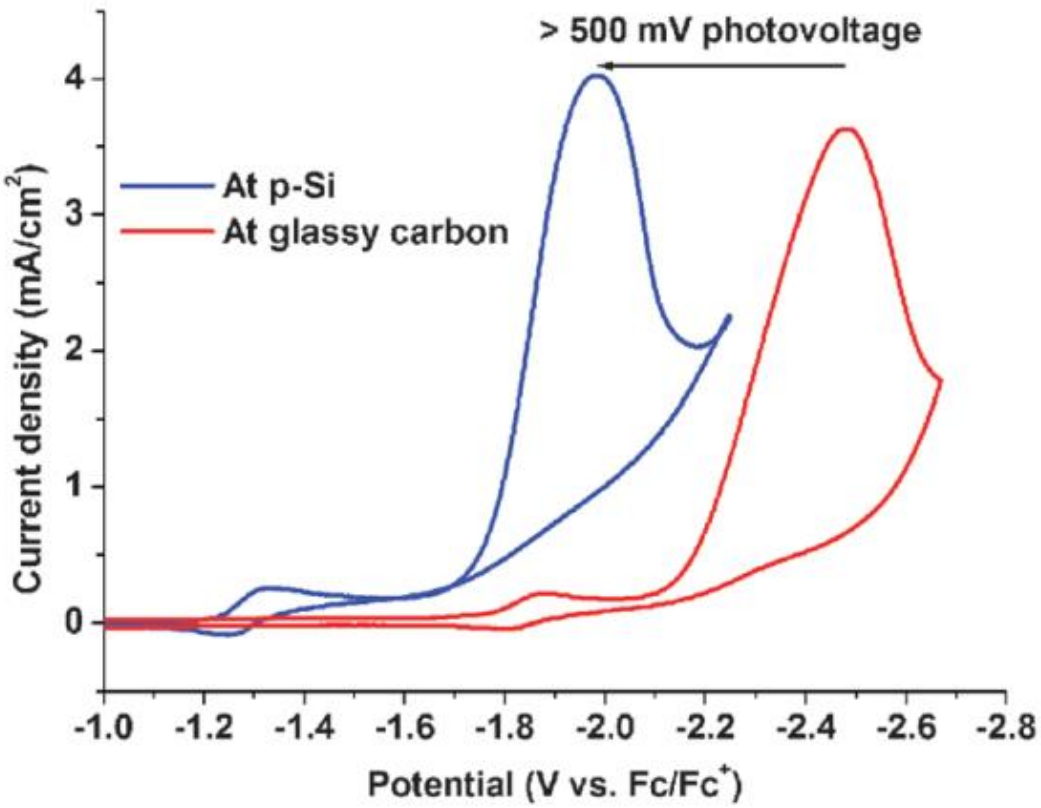

Figure 1-12 Re(bipy-tBu)(CO)3Cl electrochemistry under a CO2 atmosphere on both glassy carbon and p-Si working electrodes showing more than 500 mV of photovoltage at illuminated p-Si 0.5 mM catalyst, 0.1 M NBu_4PF6 electrolyte, Pt counter electrode, 100 mV/s scan rate. Image taken from "Tunable, light-assisted co-generation of CO and H_2 from CO_2 and H_2O by Re(bipy-tbu)$(CO)_3$Cl and p-Si in non-aqueous medium" by Kumar, et al.[46]

With respect to using light energy, the photovoltage of Fermi level pinned electrodes are inherently limited. Due to the origin of Fermi level pinning arising from mid gap states, the semiconductor approaches intrinsic charge concentrations and the equilibrium Fermi level approaches the center of the band gap. This means that even though photon energy must be at least the energy of the band gap in order to photoexcite charges, the maximum photovoltage one may achieve is about half of the total band gap, around 500mV for highly doped p-Si, compared to 720 mV for a full p-n junction silicon

photovoltaic.[46,47] While a potentially useful phenomenon to assist with energy demand in electrochemical processes, due to the size of the built in potential being roughly half of the band gap energy, one immediately loses half of the desired power one could have obtained from other implementations of this material. More complete use of the absorbed light energy may be achieved with embedded p-n junctions in the semiconductor, with a thin protective metal oxide layer that enhances the built in potential, or with external photovoltaics.[48]

Herein, we will investigate chemical methods that use light to drive reactions and release stored energy from fuels.

1.5 References

1 Tsao, J., Lewis, N. & Crabtree, G. Solar FAQs.

2 Agency, I. E. *Key world energy statistics*. (International Energy Agency, 2007).

3 Administration, E. I. *Petroleum & Other Liquids*, <http://tonto.eia.doe.gov/dnav/pet/pet_pnp_pct_dc_nus_pct_a.htm> (2015).

4 Dincer, I. Renewable energy and sustainable development: a crucial review. *Renewable and Sustainable Energy Reviews* **4**, 157-175, doi:http://dx.doi.org/10.1016/S1364-0321(99)00011-8 (2000).

5 Melis, A. Solar energy conversion efficiencies in photosynthesis: Minimizing the chlorophyll antennae to maximize efficiency. *Plant Science* **177**, 272-280, doi:http://dx.doi.org/10.1016/j.plantsci.2009.06.005 (2009).

6 Hill, J., Nelson, E., Tilman, D., Polasky, S. & Tiffany, D. Environmental, economic, and energetic costs and benefits of biodiesel and ethanol biofuels. *Proceedings of the National Academy of Sciences* **103**, 11206-11210, doi:10.1073/pnas.0604600103 (2006).

7 Botte, G. G. Electrochemical Manufacturing in the Chemical Industry. *Electrochemical Society Interface*, 49 (2014).

8 Collman, J. P. & Decreau, R. A. Functional biomimetic models for the active site in the respiratory enzyme cytochrome c oxidase. *Chemical Communications*, 5065-5076, doi:10.1039/B808070B (2008).

9 Gratzel, M. Photoelectrochemical cells. *Nature* **414**, 338-344 (2001).

10 Moussallem, I., Jörissen, J., Kunz, U., Pinnow, S. & Turek, T. Chlor-alkali electrolysis with oxygen depolarized cathodes: history, present status and future prospects. *J Appl Electrochem* **38**, 1177-1194, doi:10.1007/s10800-008-9556-9 (2008).

11 Roesky, H. W. The Renaissance of Aluminum Chemistry†. *Inorganic Chemistry* **43**, 7284-7293, doi:10.1021/ic0400641 (2004).

12 Fox, J. M. I., Chen, T. P. & Degen, B. D. An evaluation of direct methane conversion processes. *Journal Name: Chemical Engineering Progress; (USA); Journal Volume: 86:4*, Medium: X; Size: Pages: 42-50 (1990).

13 Dry, M. E. The Fischer–Tropsch process: 1950–2000. *Catalysis Today* **71**, 227-241, doi:http://dx.doi.org/10.1016/S0920-5861(01)00453-9 (2002).

14 E³ Earth, E. & Environment. in *IASS Working Paper* (Institute for Advanced Sustainability Studies (IASS), Potsdam, 2014).

15 Lu, W., Verdegaal, W. M., Yu, J., Balbuena, P. B., Jeong, H.-K. & Zhou, H.-C. Building multiple adsorption sites in porous polymer networks for carbon capture applications. *Energy & Environmental Science* **6**, 3559-3564, doi:10.1039/C3EE42226G (2013).

16 Hori, Y., Murata, A. & Takahashi, R. Formation of hydrocarbons in the electrochemical reduction of carbon dioxide at a copper electrode in aqueous solution. *Journal of the Chemical Society, Faraday Transactions 1: Physical Chemistry in Condensed Phases* **85**, 2309-2326, doi:10.1039/F19898502309 (1989).

17 Hori, Y., Takahashi, I., Koga, O. & Hoshi, N. Selective Formation of C2 Compounds from Electrochemical Reduction of CO2 at a Series of Copper Single Crystal Electrodes. *The Journal of Physical Chemistry B* **106**, 15-17, doi:10.1021/jp013478d (2002).

18 Li, C. W., Ciston, J. & Kanan, M. W. Electroreduction of carbon monoxide to liquid fuel on oxide-derived nanocrystalline copper. *Nature* **508**, 504-507, doi:10.1038/nature13249 (2014).

19 Peterson, A. A., Abild-Pedersen, F., Studt, F., Rossmeisl, J. & Norskov, J. K. How copper catalyzes the electroreduction of carbon dioxide into hydrocarbon fuels. *Energy & Environmental Science* **3**, 1311-1315, doi:10.1039/C0EE00071J (2010).

20 Chalk, S. G. & Miller, J. F. Key challenges and recent progress in batteries, fuel cells, and hydrogen storage for clean energy systems. *Journal of Power Sources* **159**, 73-80, doi:http://dx.doi.org/10.1016/j.jpowsour.2006.04.058 (2006).

21 Gurau, B. & Smotkin, E. S. Methanol crossover in direct methanol fuel cells: a link between power and energy density. *Journal of Power Sources* **112**, 339-352, doi:http://dx.doi.org/10.1016/S0378-7753(02)00445-7 (2002).

22 Jia, N., Lefebvre, M. C., Halfyard, J., Qi, Z. & Pickup, P. G. Modification of Nafion Proton Exchange Membranes to Reduce Methanol Crossover in PEM Fuel Cells. *Electrochemical and Solid-State Letters* **3**, 529-531, doi:10.1149/1.1391199 (2000).

23 Park, S., Vohs, J. M. & Gorte, R. J. Direct oxidation of hydrocarbons in a solid-oxide fuel cell. *Nature* **404**, 265-267 (2000).

24 Friedl, J. & Stimming, U. Model catalyst studies on hydrogen and ethanol oxidation for fuel cells. *Electrochimica Acta* **101**, 41-58, doi:http://dx.doi.org/10.1016/j.electacta.2012.12.130 (2013).

25 Uda, T. & Haile, S. M. Thin-Membrane Solid-Acid Fuel Cell. *Electrochemical and Solid-State Letters* **8**, A245-A246, doi:10.1149/1.1883874 (2005).

26 Shao, Z., Haile, S. M., Ahn, J., Ronney, P. D., Zhan, Z. & Barnett, S. A. A thermally self-sustained micro solid-oxide fuel-cell stack with high power density. *Nature* **435**, 795-798, doi:http://www.nature.com/nature/journal/v435/n7043/suppinfo/nature03673_S1.html (2005).

27 Sanjinés, R., Tang, H., Berger, H., Gozzo, F., Margaritondo, G. & Lévy, F. Electronic structure of anatase TiO2 oxide. *Journal of Applied Physics* **75**, 2945-2951, doi:doi:http://dx.doi.org/10.1063/1.356190 (1994).

28 Lianos, P. Production of electricity and hydrogen by photocatalytic degradation of organic wastes in a photoelectrochemical cell: The concept of the Photofuelcell: A review of a re-emerging research field. *Journal of Hazardous Materials* **185**, 575-590, doi:http://dx.doi.org/10.1016/j.jhazmat.2010.10.083 (2011).

29 Stathatos, E., Lianos, P., Falaras, P. & Siokou, A. Photocatalytically deposited silver nanoparticles on mesoporous TiO2 films. *Langmuir* **16**, 2398-2400 (2000).

30 Wang, G., Ling, Y., Lu, X., Wang, H., Qian, F., Tong, Y. & Li, Y. Solar driven hydrogen releasing from urea and human urine. *Energy & Environmental Science* **5**, 8215-8219, doi:10.1039/C2EE22087C (2012).

31 Zaky, A. M. & Chaplin, B. P. Porous Substoichiometric TiO2 Anodes as Reactive Electrochemical Membranes for Water Treatment. *Environmental Science & Technology* **47**, 6554-6563, doi:10.1021/es401287e (2013).

32 Drew, K., Girishkumar, G., Vinodgopal, K. & Kamat, P. V. Boosting Fuel Cell Performance with a Semiconductor Photocatalyst: TiO2/Pt−Ru Hybrid Catalyst for Methanol Oxidation. *The Journal of Physical Chemistry B* **109**, 11851-11857, doi:10.1021/jp051073d (2005).

33 Antoniadou, M., Kondarides, D. I., Dionysiou, D. D. & Lianos, P. Quantum Dot Sensitized Titania Applicable as Photoanode in Photoactivated Fuel Cells. *The Journal of Physical Chemistry C* **116**, 16901-16909, doi:10.1021/jp305098m (2012).

34 Bessegato, G. G., Guaraldo, T. T. & Zanoni, M. V. B. *Enhancement of Photoelectrocatalysis Efficiency by Using Nanostructured Electrodes*. (2014).

35 Xia, C., Jia, Y., Tao, M. & Zhang, Q. Tuning the band gap of hematite α-Fe2O3 by sulfur doping. *Physics Letters A* **377**, 1943-1947, doi:http://dx.doi.org/10.1016/j.physleta.2013.05.026 (2013).

36 Beranek, R. (Photo)electrochemical Methods for the Determination of the Band Edge Positions of TiO2-Based Nanomaterials. *Advances in Physical Chemistry* **2011**, doi:10.1155/2011/786759 (2011).

37 Albery, W. J., Bartlett, P. N., Hamnett, A. & Dare-Edwards, M. P. The Transport and Kinetics of Minority Carriers in Illuminated Semiconductor Electrodes. *Journal of The Electrochemical Society* **128**, 1492-1501, doi:10.1149/1.2127670 (1981).

38 Albery, W. J. & Bartlett, P. N. The Recombination of Photogenerated Minority Carriers in the Depletion Layer of Semiconductor Electrodes. *Journal of The Electrochemical Society* **130**, 1699-1706, doi:10.1149/1.2120065 (1983).

39 Albery, W. J. & Bartlett, P. N. The Transport and Kinetics of Photogenerated Carriers in Colloidal Semiconductor Electrode Particles. *Journal of The Electrochemical Society* **131**, 315-325, doi:10.1149/1.2115568 (1984).

40 Le Formal, F., Pastor, E., Tilley, S. D., Mesa, C. A., Pendlebury, S. R., Grätzel, M. & Durrant, J. R. Rate Law Analysis of Water Oxidation on a Hematite Surface. *Journal of the American Chemical Society* **137**, 6629-6637, doi:10.1021/jacs.5b02576 (2015).

41 Akihiro, N., Masakazu, S., Katsushi, F. & Yoshiaki, N. Comparison of Semiconductor–Electrolyte and Semiconductor–Metal Schottky Junctions Using AlGaN/GaN Photoelectrochemical Electrode. *Japanese Journal of Applied Physics* **52**, 08JN20 (2013).

42 Kolaklieva, L. & Kakanakov, R. *Ohmic Contacts for High Power and High Temperature Microelectronics*. (2009).

43 Ongaro, M., Signoretto, M., Trevisan, V., Stortini, A. & Ugo, P. Arrays of TiO2 Nanowires as Photoelectrochemical Sensors for Hydrazine Detection. *Chemosensors* **3**, 146 (2015).

44 Moison, J. M. & Bensoussan, M. Surface recombination, surface states and Fermi level pinning. *Rev. Phys. Appl. (Paris)* **22**, 293-297 (1987).

45 Linsebigler, A. L., Lu, G. & Yates, J. T. Photocatalysis on TiO2 Surfaces: Principles, Mechanisms, and Selected Results. *Chemical Reviews* **95**, 735-758, doi:10.1021/cr00035a013 (1995).

46 Kumar, B., Smieja, J. M., Sasayama, A. F. & Kubiak, C. P. Tunable, light-assisted co-generation of CO and H2 from CO2 and H2O by Re(bipy-tbu)(CO)3Cl and p-Si in non-aqueous medium. *Chemical Communications* **48**, 272-274, doi:10.1039/C1CC16024A (2012).

47 Kumar, B., Llorente, M., Froehlich, J., Dang, T., Sathrum, A. & Kubiak, C. P. Photochemical and Photoelectrochemical Reduction of CO2. *Annual Review of Physical Chemistry* **63**, 541-569, doi:doi:10.1146/annurev-physchem-032511-143759 (2012).

48 Scheuermann, A. G., Lawrence, J. P., Kemp, K. W., Ito, T., Walsh, A., Chidsey, C. E. D., Hurley, P. K. & McIntyre, P. C. Design principles for maximizing photovoltage in metal-oxide-protected water-splitting photoanodes. *Nat Mater* **advance online publication**, doi:10.1038/nmat4451

Chapter 2

Catalytic photocurrent multiplication in the oxidation of multi-carbon fuels, principles and challenges

2.1 Introduction to Photo Fuel Cells and Current Multiplication

As technology to improve energy density in batteries has been slow forthcoming, there has been increasing interest in the related technology of transportable fuel cells. Since the energy density of liquid fuels is two orders of magnitude larger than that of commercial batteries, small transportable fuel cells could prove longer lasting and higher power alternatives.[1] As discussed in Chapter 1, there are many hurdles in the implementation of small transportable fuel cells. Gas phase molecules such as hydrogen require compression or cooling to condense and store them which increases the effective fuel weight and energy cost from specialized containment.[2] Small molecule solution phase fuels such as methanol suffer from relatively low gravimetric energy density. Methanol suffers from fuel crossover between the anode and cathode compartments leading to the fuel being directly oxidized by oxygen with its energy lost to heat. Formate is less susceptible to membrane crossover due to its ionic nature but has an energy density less than half of methanol.[3] Larger molecule fuels may serve as competent alternatives though not without their own challenges.

As our capacity for storing solar energy in multi-carbon fuels continues to improve, increasing the efficiency of energy extraction from these fuels is key to a renewable energy cycle.[4] When oxidizing multi-carbon fuels such as hydrocarbons or aromatics by electrolytic means, oxidation stalls when stable intermediates are formed such as carboxylates which require energy intensive C-C activation. Unless additional energy is supplied to the system or the applied overpotential becomes exceedingly anodic, these intermediates prevent access to stored chemical energy and can lead to undesirable side products that mitigate further fuel oxidation.[5,6]

Methods for overcoming these limitations include higher temperature fuel cell devices that operate above 200°C such as those developed by the Haile group in Caltech; however, to avoid damaging devices or users, near-ambient operating temperatures may be necessary for electronic applications, especially personal devices.[7] As an alternative to heat, light energy may be used to overcome kinetic barriers. Large band gap photoanodes absorb light to produce photoexcited holes capable of oxidizing most organic materials.[8,9] This light energy need not be used in every oxidation step. In principle, once a stable compound has undergone oxidation at the photoanode, a more reactive intermediate will be produced. This second intermediate often comes in the form of a radical which may be further oxidized without additional light input. “Dark” oxidation may continue via electron injection into the conduction band or oxidation by another electrode until another prohibitively stable intermediate is formed or until complete mineralization is achieved.

For this scheme to prove practical, it must maximize the electrical energy extracted while minimizing the light used. Since electrical power is proportional to current, P=IV, we may wish to reframe this as maximizing current and minimizing light

for a given voltage. Such a fuel cell device will be called a photo fuel cell and any system that produces current in excess of the photogenerated current will be described as exhibiting photocurrent multiplication or simply current multiplication. The initially imagined scheme for such a device is depicted in Figures 2-1.

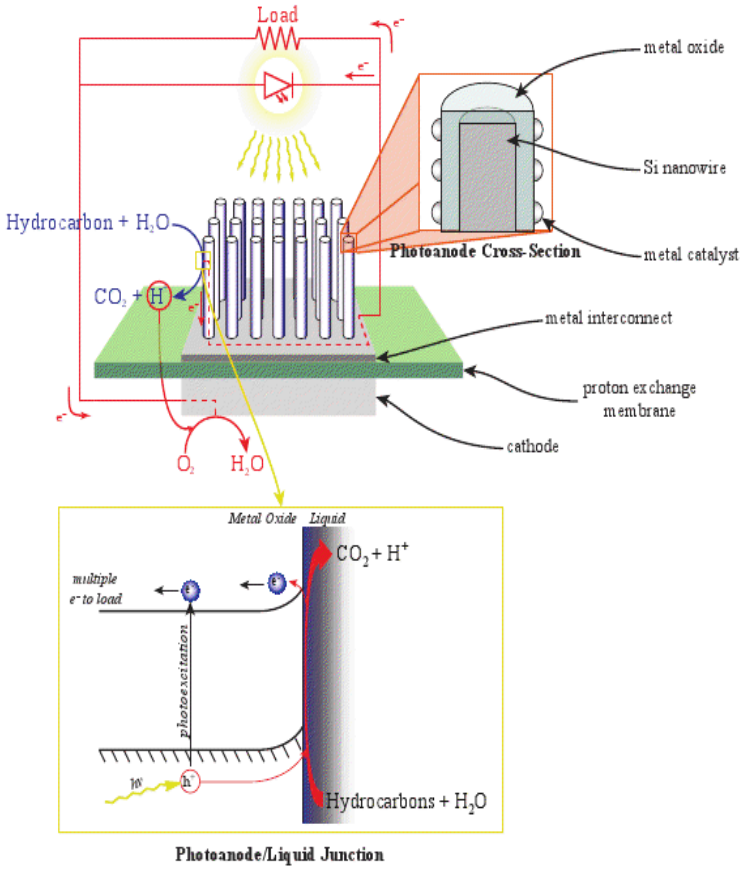

Figure 2-1 A basic scheme of a simplified photo fuel cell device. The photoanode consists of an array of high surface area microwires coated with additional metal catalyst nanoparticles which decompose the fuel. Under illumination, metal nanoparticles may increase photoexcited charge carrier separation by accepting electrons from the semiconductor and enhancing the built in potential near the surface. The semiconductor array back contact collects more electrons than photoexcited holes produced. Oxygen is reduced to water at the cathode.

An additional point of consideration is the choice of light source used for these processes. In general, most semiconductors absorb photons that have higher energy than their band gap. As depicted in the previous figures, LEDs may be driven by fuel cells and feed energy back into them. While some of the energy is recovered and used in performing oxidations, any losses in light production or light absorption will lead to massive net energy losses from the device. The most efficient UV-LEDs have ~50% power and external quantum efficiency at present which on its own may prove to be sufficient if the other energy conversion efficiency is sufficiently high or it could represent a major hurdle in the feasibility of such a device.[10]

Current Multiplication on Semiconductor Electrodes

The term current multiplication is used to describe any phenomenon wherein the choice of substrate leads to photocurrent that exceeds what would be expected for a given illumination intensity and applied voltage. Strictly speaking, current multiplication occurs when a mechanism yields an effective quantum yield greater than unity often in a distinct multiple such as doubling or quadrupling. Systems that produce conducting electrons or holes excess of the photoexcited pairs must receive the additional charges from the consumption of material or chemical substrate. A famous example of this is found in the light-enhanced etching of n-silicon where photoexcited holes drift to the surface and destabilize surface silicon bonds. In the presence of F^- the destabilized surface silicon atoms are readily ionized by entering solution which creates enough driving force to eject up to three additional electrons into the conduction band of the bulk semiconductor for a quantum yield of 4.

Current multiplication may also occur on high band gap semiconductors such as TiO_2, ZnO, CdS, and WO_3 in the presence of organic substrates.[11,12] In this process the initial oxidation of a molecule creates a highly reducing radical that injects its unpaired electron into the semiconductor conduction band. In other words, unlike light-assisted silicon etching, an electron excess of the photogenerated current is transferred to the electrode from a substrate oxidation intermediate. As an example in Figure 2-2, methanol is a well-established current doubling substrate. Once oxidized, the O-H bond is activated leaving behind highly reducing methoxy radical. This radical transfers an electron to the conduction band of the semiconductor anode, a process we will describe in more detail in the next section.

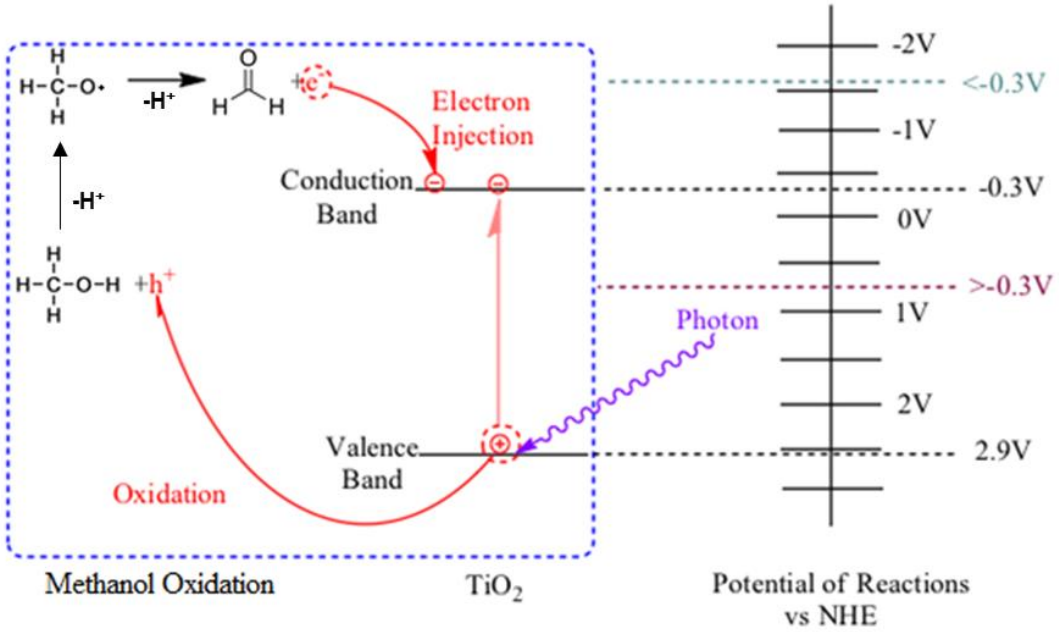

Figure 2-2 Photocurrent doubling through the oxidation of methanol. A photon is first absorbed at the large bandgap semiconductor producing an electron hole pair. The hole oxidizes the oxalate which activates the O-H bond which leads to spontaneous deprotonation and leaves behind the methoxy radical. This radical has a reducing enough potential to inject an electron into the conduction band of the semiconductor giving a yield of two electrons per photoexcitation event and upon a second deprotonation becomes formaldehyde.

2.2 Discussion

Metal Oxides

For a given metal oxide, reaction conditions can dictate its efficacy as a photoanode material. In aqueous systems, high acidity or alkalinity may etch away active material or increase photocurrent response. TiO_2 is most active under basic aqueous conditions mostly due to the high concentration of hydroxides which participate in oxidation as adsorbed OH• intermediates. In highly acidic conditions TiO_2 can be quickly etched away. WO_3 is most active under acidic and neutral conditions but is unstable in basic media.[13] I fabricated and tested various electrode materials for their capacity to current multiply with the most robust and actives electrodes made from films of p25 TiO_2 nanoparticle films and electrodeposited films of WO_3. It should be noted that these materials also have the roughest surface topologies of the materials I tested and therefore had the advantage of more reaction sites per given mass of deposited material.

The four main types of electrode materials I tested were TiO_2 nanoparticle films, sol gel TiO_2, commercial single crystalline rutile TiO_2, and electrodeposited WO_3. The fabrication methods of all of these electrodes are discussed in more detail in Section 2.3. I chose these various forms of TiO_2 due to their well-established capacity for mineralization of organics under UV illumination in both neutral and alkaline aqueous media. I chose electrodeposited WO_3 for being an effective and robust current doubling photoanode under acidic conditions.[14] I fabricated the TiO_2 electrodes using Degussa p25 nanoparticles by spincoating and annealing either a nanoparticle suspension or a sol gel precursor solution onto conductive back contacts made of titanium, silver, or conductive metal oxides. To make the (001) rutile electrodes, I used a quartz tube furnace and

forming gas to hydrogen dope commercially available polished single crystalline squares with conductive silver paint as a back contact. I fabricated WO_3 electrodes through electrochemical deposition as per literature methods.[15] **Figure 2-3** shows scanning electron microscope (SEM) images of the electrode materials used in my studies.

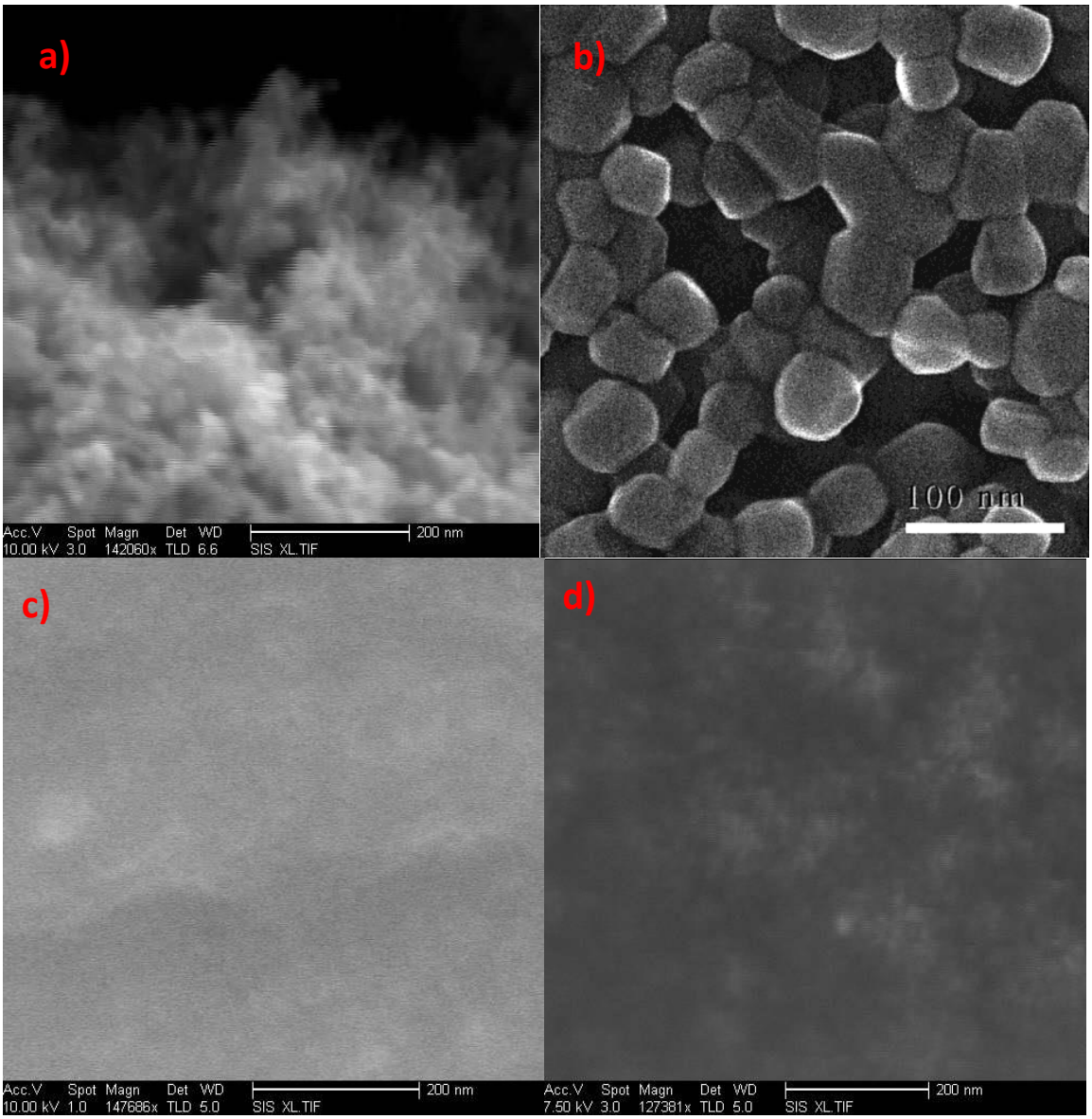

Figure 2-3 Sub-micron SEM images showing surface topology of the photoanode materials I studied: a) p25 TiO_2 film, b) electrodeposited WO_3, c) sol gel TiO_2, and d) single crystalline rutile (001) TiO_2. The highest surface area materials, a) and b) gave the highest photoresponse to illumination and were used in subsequent photoelectrochemical studies. Image b) was taken with the assistance of collaborator Robert Coridan.

Demonstrations of current multiplication using methanol as the current doubling substrates are shown in the photocurrent vs voltage curves below in Figure 2-4 and Figure 2-5. Oxidations with WO_3 were performed in 0.1 M H_2SO_4 aqueous solution with 2.4 mW/cm^2 365 nm excitation and oxidations with p25 TiO films were performed under 0.1 M NaOH aqueous media under 0.6 mW/cm^2 365 nm illumination.

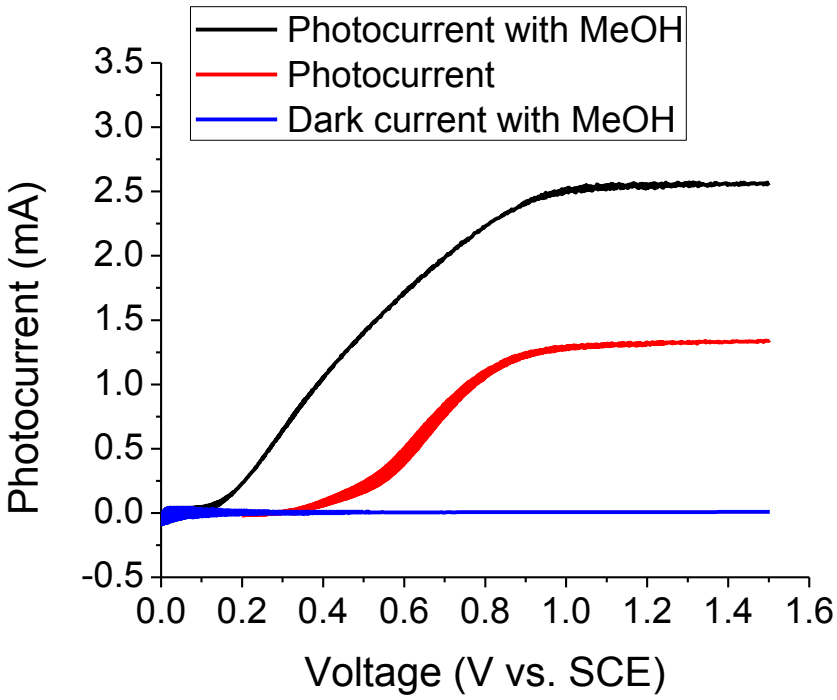

Figure 2-4 Cyclic voltammograms using WO_3 electrode run with 0.1M H_2SO_4 aqueous. Scan rate was performed at 5 mV/s. Samples with methanol contain four percent MeOH by volume or 1000 mM MeOH wherein saturated photocurrent is reached.

An increase in photocurrent when switching between substrates is insufficient to prove current doubling is taking place. For example, some substrates may be easily adsorbed at the surface but have slow oxidation kinetics. On TiO_2, photocurrent with saturated methanol is more than double that of the oxidation of water, which cannot be explained by current doubling alone. Intensity modulated photocurrent spectroscopy

(IMPS) is a powerful technique for evaluating the quantum yield and photocurrent efficiency of compound semiconductors.[11,16] This method uses a sinusoidal signal to modulate the intensity of light from the photon source but requires planarized materials to deliver reliable values at higher frequencies. Alternative methods for demonstrating current multiplication were needed.

A direct comparison between traditional photocurrent and current doubling may be seen in the oxidation of solution saturated ferrocene versus solution saturated methanol as shown in Figure 2-5. Ferrocene is a well-established redox standard in electrochemistry with fast charge transfer kinetics that may be reversibly oxidized to ferrocenium. Photocurrent from methanol is nearly exactly double that of the ferrocene oxidation.

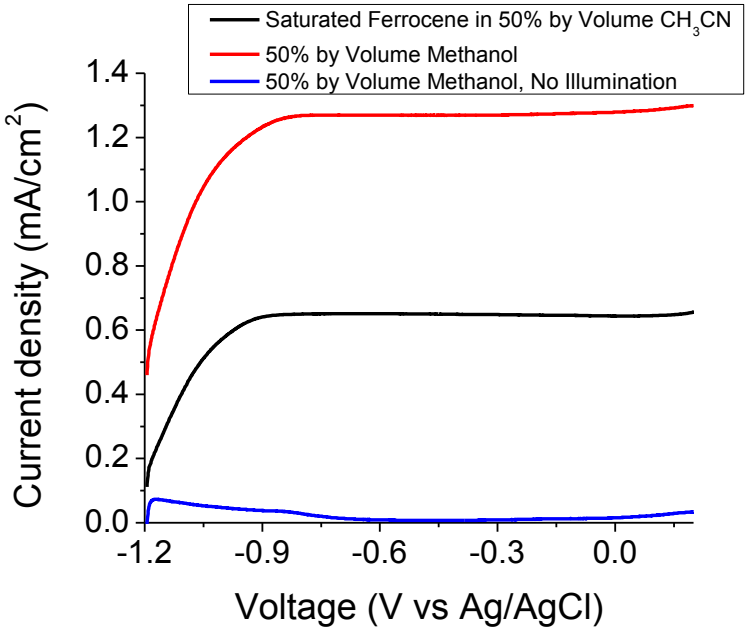

Figure 2-5 Comparing photocurrent between ferrocene and methanol under 2.4 mW/cm^2 illumination on a p25 electrode. Both solutions contain 0.1 M NaOH. The solution with ferrocene contains 50% acetonitrile by volume to ensure solubility of the analyte. Current with methanol is almost exactly double that of the ferrocene as is consistent with current doubling. Scans were performed at a rate of 20 mV/s.

Overcoming the Limitations of Current Doubling

There are both kinetic and thermodynamic limitations to current multiplication. For current doubling to occur, we are primarily interested in materials that can produce highly energetic holes, but we also require low enough conduction bands to accommodate electron injection from reaction intermediates yet high enough to maintain a depletion region without requiring high anodic biasing to collect electrons and push photoexcited holes to the surface. With regard to the choice of fuel substrates, oxidized species must have an oxidation potential more negative than the conduction band height. In other words, the oxidation intermediate must be a powerful enough reducing agent to transfer an electron to the conduction band of the electrode. Table 2-1 below shows the redox potentials of various free radicals in water. The highlighted radicals have energy positions negative enough to reduce the conduction band of TiO_2 at pH 7.

Table 2-1 Redox potentials of free radicals in aqueous solution. Species with redox potentials more negative than the conduction band of TiO_2 are highlighted in blue. E_m is the measured potential and E° is the potential normalized to pH 7. All highlighted substrates are established current doubling substrates. Table adjusted from "Redox potentials of free radicals. I. Simple organic radicals" by Rao and Hayon.[17]

Substrate	Radical form	pH	E_m, V	$E^{\circ\,1}$, V
Lactic acid	$CH_3\dot{C}(OH)COOH$	3.2	+0.40	+0.25
	$CH_3\dot{C}(OH)COO^-$	7.0	−0.20	−0.12
	$CH_3\dot{C}(O^-)COO^-$	10.8	−0.56	−0.47
Glycolic acid	$\dot{C}H(OH)COO^-$	7.0	−0.36	−0.28
	$\dot{C}H(O^-)COO^-$	10.0	−0.66	−0.57
Glycolamide	$\dot{C}H(OH)CONH_2$	3.2	+0.34	+0.19
	$\dot{C}H(O^-)CONH_2$	7.0	−0.26	−0.17
Lactamide	$CH_3\dot{C}(OH)CONH_2$	3.2	+0.20	0.05
	$CH_3\dot{C}(O^-)CONH_2$	8.5	−0.43	−0.34
Isopropyl alcohol	$(CH_3)_2COH$	1.5	−0.58	−0.83
	$(CH_3)_2\dot{C}OH$	7.0	−0.90	−0.82
				−1.05
	$(CH_3)_2\dot{C}O^-$	13.0	<−1.40	<−1.31
		13.5	∼−1.95[f]	∼−1.95
Ethyl alcohol	$CH_3\dot{C}HOH$	7.0	−0.77	−0.69
				−0.93
	$CH_3\dot{C}HO$	13.0	<−1.40	<−1.31
		13.5	∼−1.65[f]	∼−1.65
Methyl alcohol	$\dot{C}H_2OH$	7.0	−0.73[f]	−0.73
	$\dot{C}H_2O^-$	11.8	<−1.40	<−1.31
		13.5	−1.48[f]	∼1.48
Ribose	$\cdot C_5H_9O_5$	7.0	−0.05	+0.03
		7.0	∼−0.65	∼−0.57
Deoxyribose	$\cdot C_5H_9O_4$	7.0	−0.19	−0.11
		7.0	−0.65	−0.57
Formate	$\cdot CO_2^-$	7.0	≪−0.50	≪−0.42
		6.0	−1.09	−1.09
Oxaloacetate	$\dot{C}(OH)COO^-$	7.0	−0.16	−0.29
	$\vert$			
	CH_2COO^-			
	$\dot{C}(O^-)COO^-$	10.8	<−0.90	<−1.03
	$\vert$			
	CH_2COO			
Glycine	$NH_2\dot{C}HCOO^-$	8.0	−0.87	−0.73
Glycine anhydride	$NH\dot{C}HCONHCH_2CO$	7.0	∼+0.40	∼+0.49
	$N\dot{C}HCONHCH_2CO$	10.8	−0.48	−0.39

While current multiplication may be directly measured through photoelectrolysis, we must also ensure that we are producing the desired two electron oxidation product. In the case of methanol oxidation, formaldehyde is our expected product. I quantified formaldehyde using an aldehyde specific detection chromophore called Purpald which was prepared by standard methods.[18] Standards were created using methanol stabilized formaldehyde in concentrated NaOH solutions which were subsequently diluted with

0.1M NaOH water. Pure methanol showed no interaction with purpald. Figure 2-6 demonstrates the linearity of Purpald's absorption peak with concentrations of formaldehyde.

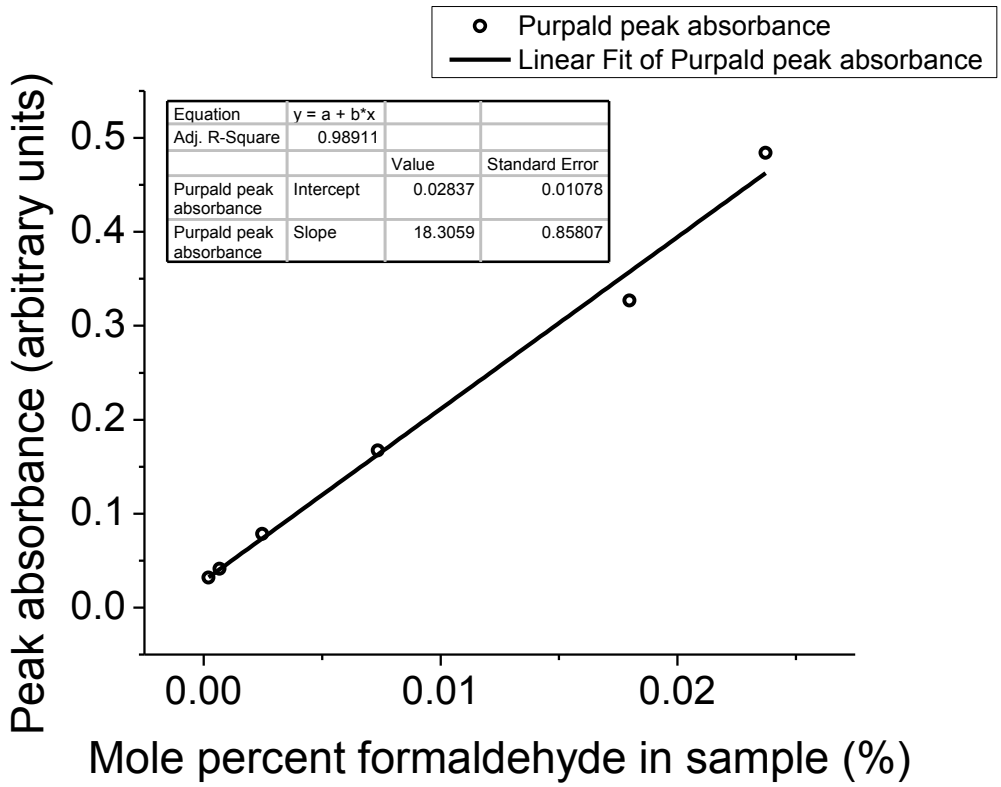

Figure 2-6 Formaldehyde calibration line with reliable linear correlation between formaldehyde concentration and peak absorption of Purpald at 538 nm. This calibration curve was created with help of collaborator Anna Beck.

Bulk electrolyses with and without solution stirring were performed and formaldehyde was measured via Purpald. Bulk electrolyses with WO_3 were performed in 4 mM MeOH in 0.1 M H_2SO_4 aqueous solution using electrodeposited WO_3 as the working electrode material under 2.4 mW/cm^2 illumination from a 365 nm LED. Similar electrolyses were performed for p25 TiO_2 using 4 mM MeOH and 0.1 M NaOH. A sample UV-visible absorption spectrum of Purpald WO_3 oxidation is pictured below in **Figure 2-7**. Stirring of both solutions gave higher yields for formaldehyde; however, the

total yields remained low. Oxidations by WO_3 gave 15% yield with stirring and 7.8% yield without. Oxidations with TiO_2 gave 12% yield with stirring and 9% without.

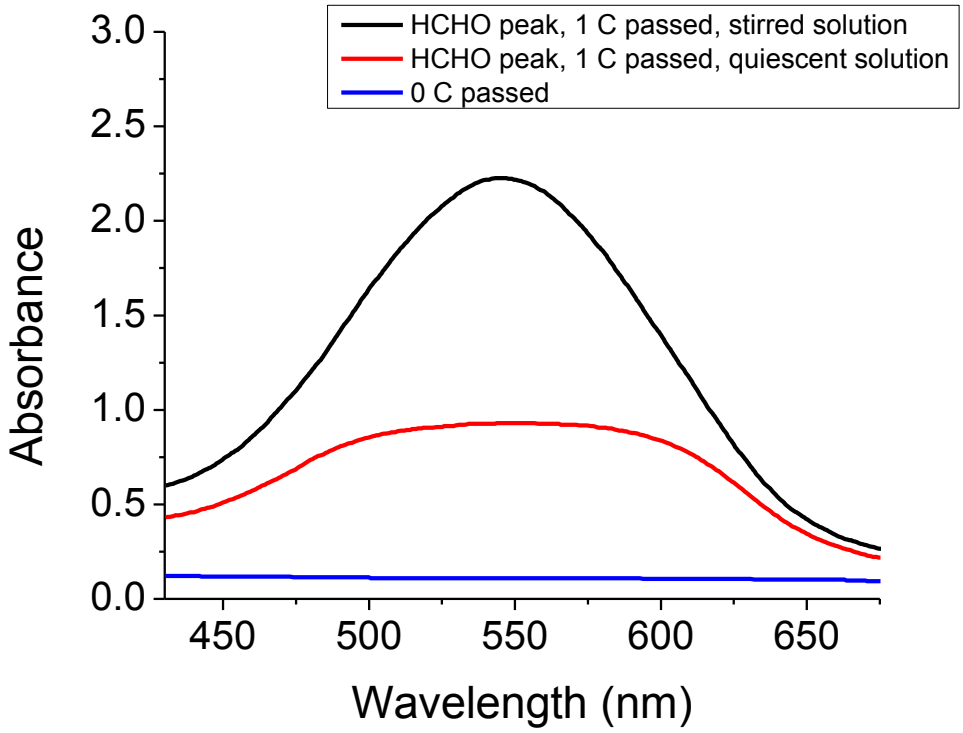

Figure 2-7 Absorption peaks of Purpald after the photoxidation of 40mM MeOH in 0.1M H_2SO_4 aqueous solution on illuminated WO_3 held at 0.5V vs Ag/AgCl. The peak heights correspond to formaldehyde yields of 15% with solution stirring and 7.8% with no stirring. This shows a 1.9x increase in formaldehyde yield when solution is stirred. Photocurrent with and without stirring were identical under these conditions.

As one may note, less than quantitative yields of formaldehyde are detected implying that formaldehyde is consumed by the photoelectrode as a current doubling substrate. While current doubling is beneficial to the overall conversion efficiency of the system, electrons acquired from formaldehyde would be better retrieved via non-photoanodic means. Methods for improving formaldehyde electron collection will be explored in Chapter 3.

2.3 Methods

Fabrication of Metal Oxide Photoelectrodes

The electrodes used in this chapter were fabricated via spin coating nanoparticle TiO_2 and electrodepositing nanoparticle WO_3 onto conductive back contacts. FTO, ITO, Ag, Ti were used as back contacts as all these materials demonstrated ohmic behavior when using these forms of WO_3 and TiO_2. ITO and FTO on glass were used as purchased from Sigma Aldrich for back illumination experiments. Ti and Ag back contact films were deposited onto glass slides via sputtering. All surfaces were degreased via sonication in a series of water, isopropanol, and methanol before material deposition. Once the films were annealed, onto the back contact surfaces, a circular area of active semiconductor surface on all electrodes was left uncovered while the rest was sealed with an inert Loctite 1C Hysol epoxy to prevent contact between solution and inactive parts of the electrode.

TiO_2 Nanoparticle Film Electrode Deposition

For TiO_2 films, commercially available p25 TiO_2 was purchased from Degussa. The material is comprised of a mixture of rutile and anatase phase nanoparticles with an average diameter of 25 nm. A suspension of 400 mg of p25 nanoparticles in 5 mL of 50%v/v ethanol and water was cast onto the conductive back contacts at 500 RPM for 5 seconds followed immediately by spinning the stage at 1500 RPM for another 60 seconds or until the film is uniform and solvent evaporated. I left one edge of the back contact surface revealed where a wire lead could be attached. The as deposited material was placed into a 500°C tube furnace open to atmosphere for three hours to anneal the film to the back contact and the nanoparticles to each other.

WO_3 Nanoparticle Film Electrodeposition

WO_3 electrodes were made as per literature.(ref) A solution of peroxytungstic acid (50 mM) in 30% (v/v) isopropanol/water was stirred at room temperature for 24 hours in the presence of a Pt mesh. The Pt mesh and isopropanol reduced the concentration of free H_2O_2. An FTO slide was then immersed in the peroxytungstic acid solution to a depth of 1.0 cm, and cathodic electrodeposition was performed in quiescent solution at -0.50 V vs. Ag/AgCl to produce a passage of charge density of -0.25 C/cm^2 at a current density of approximately -0.3 mA/cm^2. The sample was then removed, rinsed with water and ethanol, then heated in air at 275°C for 10 minutes. The deposition cycle was completed three times. The sample was annealed at 500°C in air for an hour yielding an approximate WO_3 film thickness of 300 nm.

TiO_2 Sol Gel Film Deposition

Sol gel solution of TiO_2 was made by pipetting 758 µL of titanium isopropoxide into a flask with 15 mL of isopropanol. Solution was stirred and 35 mL of 3% hydrogen peroxide was added dropwise to solution until the addition was completed. The flask was lightly covered with aluminum foil to stir overnight. The prepared solution was spincoated at 1500 RPM then annealed at 450°C for 3 hours.

Rutile TiO_2 Annealing

Single crystalline rutile (001) surface TiO_2 was purchased from Across International and was annealed at 800°C under forming gas to increase material conductivity through hydrogen doping.

Bulk Photoelectrolyses

Photoelectrolyses were performed using a custom Teflon electrochemical cell with quartz windows. Photoelectrodes were placed within the working solution 1 cm from the illumination source. Electrodes were illuminated under 2.4 mW/cm^2 illumination intensity from a 365 nm LED purchased from Thor Labs and light intensity was measured by an Ophir PD300 silicon photodiode power sensor. For photoelectrolyses using WO_3 and TiO_2 photoanodes, 0.1 M H_2SO_4 and 0.1 M NaOH aqueous solutions were used, respectively. Prior to all electrochemical experiments, the working solution was sparged with N_2 or Argon gas to remove oxygen.

Formaldehyde Quantification

Formaldehyde was quantified via an aldehyde detecting chromophore called Purpald. A Purpald solution was prepared by standard methods.(ref) 10-20 mg purpald was added to 1.5 mL of 1 M NaOH solution. 10 µL of target solution was added and solutions were sonicated or allowed to react for 30 minutes until the full color developed. Standards were created using methanol stabilized formaldehyde in concentrated NaOH solutions diluted with 0.1M NaOH water. Pure methanol showed no interaction with purpald. The absorption peak corresponding to the Purpald reaction was centered at 545 nm and peak height tracked linearly with known aldehyde concentration. Peak height was measured using a Shimadzu UV- 3600 spectrometer. Aldehyde product quantification from bulk electrolyses was performed by by adding 10 µL of the working electrolyte solution to the standard Purpald detection solution as previously described and measuring the 545 nm absorption peak height. When aldehyde product was too concentrated for the spectrometer to detect, dilutions of the target electrolyte solutions were made and added to standard Purpald detection solution until they were within quantification limits.

2.4 Conclusion

From the above results, we have re-established current multiplication as a viable method for fuel oxidation in a fuel cell device but have not been able to surpass the limit of current doubling which restricts us to, at best, two electrons captured from a fuel per excitation event in a photoanode. While this limit could represent a major hurdle in the net efficiency of a fuel cell device as we have proposed, multiple catalysts and anode materials could be used simultaneously to bypass this doubling threshold and capture electrons from oxidation intermediates downstream from the photoanode. For example, formaldehyde, which is a relatively potent reducing agent, may be easily oxidized at a gold or platinum anode instead of the illuminated TiO_2 and WO_3 electrodes as shown in this chapter and induced mass transport such as through solution stirring may prove sufficient to prevent unwanted downstream oxidation of intermediates by the photoanode.

2.5 Acknowledgements

Much of the material in this chapter is related to a patent "Photoassisted high efficiency conversion of carbon-containing fuels to electricity" with shared invention ownership by Clifford P. Kubiak, Mark J. Llorente, Nathan S. Lewis, Robert H. Coridan, and Anna R. Beck. Additional work came from Bhupendra Kumar.

2.6 References

1 Winter, M. & Brodd, R. J. What are batteries, fuel cells, and supercapacitors? *Chemical reviews* **104**, 4245-4270 (2004).

2 Steward, D., Saur, G., Penev, M. & Ramsden, T. Lifecycle cost analysis of hydrogen versus other technologies for electrical energy storage. *US National Renewable Energy Laboratory (NREL)* (2009).

3 Rice, C., Ha, S., Masel, R. I., Waszczuk, P., Wieckowski, A. & Barnard, T. Direct formic acid fuel cells. *Journal of Power Sources* **111**, 83-89, doi:http://dx.doi.org/10.1016/S0378-7753(02)00271-9 (2002).

4 König, D. H., Baucks, N., Dietrich, R.-U. & Wörner, A. Simulation and evaluation of a process concept for the generation of synthetic fuel from CO2 and H2. *Energy* **91**, 833-841, doi:http://dx.doi.org/10.1016/j.energy.2015.08.099 (2015).

5 Park, S., Vohs, J. M. & Gorte, R. J. Direct oxidation of hydrocarbons in a solid-oxide fuel cell. *Nature* **404**, 265-267 (2000).

6 Friedl, J. & Stimming, U. Model catalyst studies on hydrogen and ethanol oxidation for fuel cells. *Electrochimica Acta* **101**, 41-58, doi:http://dx.doi.org/10.1016/j.electacta.2012.12.130 (2013).

7 Uda, T. & Haile, S. M. Thin-Membrane Solid-Acid Fuel Cell. *Electrochemical and Solid-State Letters* **8**, A245-A246, doi:10.1149/1.1883874 (2005).

8 Umar, M. & Aziz, H. A. *Photocatalytic Degradation of Organic Pollutants in Water*. (2013).

9 Fateh, R., Dillert, R. & Bahnemann, D. Self-Cleaning Properties, Mechanical Stability, and Adhesion Strength of Transparent Photocatalytic TiO2–ZnO Coatings on Polycarbonate. *ACS Applied Materials & Interfaces* **6**, 2270-2278, doi:10.1021/am4051876 (2014).

10 Mueller-Mach, R., Mueller, G. O., Krames, M. R., Shchekin, O. B., Schmidt, P. J., Bechtel, H., Chen, C.-H. & Steigelmann, O. All-nitride monochromatic amber-emitting phosphor-converted light-emitting diodes. *physica status solidi (RRL) – Rapid Research Letters* **3**, 215-217, doi:10.1002/pssr.200903188 (2009).

11 Herrasti, P. & Peter, L. Photocurrent doubling during the oxidation of formic acid at n-CdS: an investigation by intensity modulated photocurrent spectroscopy. *Journal of Electroanalytical Chemistry and Interfacial Electrochemistry* **305**, 241-258, doi:http://dx.doi.org/10.1016/0022-0728(91)85522-Q (1991).

12 Higashimoto, S., Ushiroda, Y. & Azuma, M. Electrochemically Assisted Photocatalysis of Hybrid WO3/TiO2 Films: Effect of the WO3 Structures on Charge Separation Behavior. *Topics in Catalysis* **47**, 148-154, doi:10.1007/s11244-007-9026-3 (2008).

13 Gerrard, W. Photoelectrolysis using a tungsten oxide anode in chlorine and sulphate solutions. *Journal of Electroanalytical Chemistry and Interfacial Electrochemistry* **86**, 421-424 (1978).

14 Mi, Q., Coridan, R. H., Brunschwig, B. S., Gray, H. B. & Lewis, N. S. Photoelectrochemical oxidation of anions by WO3 in aqueous and nonaqueous electrolytes. *Energy & Environmental Science* **6**, 2646-2653, doi:10.1039/C3EE40712H (2013).

15 Mi, Q., Zhanaidarova, A., Brunschwig, B. S., Gray, H. B. & Lewis, N. S. A quantitative assessment of the competition between water and anion oxidation at WO3 photoanodes in acidic aqueous electrolytes. *Energy & Environmental Science* **5**, 5694-5700, doi:10.1039/C2EE02929D (2012).

16 Peter, L. M. in *Comprehensive Chemical Kinetics* Vol. Volume 37 (eds R. G. Compton & G. Hancock) 223-280 (Elsevier, 1999).

17 Rao, P. S. & Hayon, E. Redox potentials of free radicals. I. Simple organic radicals. *Journal of the American Chemical Society* **96**, 1287-1294, doi:10.1021/ja00812a004 (1974).

18 Jendral, J. A., Monakhova, Y. B. & Lachenmeier, D. W. Formaldehyde in alcoholic beverages: large chemical survey using purpald screening followed by chromotropic Acid spectrophotometry with multivariate curve resolution. *International journal of analytical chemistry* **2011** (2011).

Chapter 3

A complete pathway for complete hydrocarbon oxidation in a photo fuel cell

3.1. Introduction

Much of the effort in fossil fuel mitigation has been directed toward methods compatible with existing infrastructure and energy technologies. One thrust has centered on developing synthetic fuels from renewable chemical feedstocks and alternative energies. While it is convenient to produce large quantities of simple small molecule fuels such as hydrogen, methanol, or formate, higher order reduction products such as manmade hydrocarbons have volumetric energy densities high enough to compete with fossil fuels.[1]

While combustion remains the easiest and most prolific method for extracting energy from fuels, the difficulty and cost of storing energy in synthetic fuels makes more efficient means of conversion attractive. One such technology is the fuel cell which transforms a combustion reaction into its constituent oxidation and reduction half-reactions. By spatially separating the two processes, electrical power can be extracted from the reaction. While fuel cell conversion efficiencies can surpass the fundamental combustion efficiency set by the Cannot cycle, multi-carbon fuels prove difficult to oxidize in a fuel cell without energy intensive methods such as operation at high

temperatures so as to overcome the energy barriers associated with their strong molecular bonds and stabilizing structures.[2,3]

As described in Chapter 2, one such method for overcoming these barriers at near ambient conditions is the photo fuel cell. The basic principle is as follows. First a portion of the electrical energy withdrawn from a fuel is used to power a light source. This light excites a photosensitive catalytic material that can perform energy intensive C-C and C-H activations. Upon oxidizing fuel molecules, this activation produces high energy intermediates that may be oxidized without further need for light until another highly stable intermediate is formed. Herein, we choose as our fuel linear hydrocarbons for their simplicity and energy density. As our photocatalytic anode materials we choose electrodes made from TiO_2 and WO_3 films for their robustness and well-demonstrated capacity for mineralization of organics under illumination.[4,5]

Choice of Fuel

Many metal oxide materials are capable of complete mineralization of organics in the presence of oxygen. Under illumination, TiO_2 and WO_3 produce highly oxidizing holes that collect at the surface and react with nearby organic materials and other surface bound species. When under aerobic conditions, oxygen facilitates complete oxidation of organics by either directly oxidizing the substrates or removing electrons gathered at the surface of the metal oxide to ensure holes continue to collect at the surface. However, in a fuel cell device, oxygen must be excluded in the anode chamber where fuel oxidation takes place to ensure electrons are collected by the anode. Under these conditions, complete oxidation of the fuel may be hindered leading to unwanted side-products that prevent complete fuel consumption. For example, molecules with long lived oxidation

intermediates such as radical aromatics may be too stable to further oxidize under reaction conditions or, worse, react with each other to form more complex molecules.[6] As such we have taken as our model fuel a simple linear saturated hydrocarbon chain which represents the highest reduction state possible for a given number of carbons and has the lowest molecular complexity.

Disassembling the Hydrocarbon Chain

A proposed pathway for efficient oxidation of an n-carbon long alkane is shown in Figure 3-1. While complete mineralization of hydrocarbons and long chain organics by illuminated metal oxides is known, the express goal of minimizing light input and maximizing electrical output has not been explored.[7-9] Unless we can sufficiently reduce the number of photoexcitations required for mineralization, organics and hydrocarbons cannot serve as competent synthetic fuels for the proposed photo fuel cells. At this stage, it is uncertain if such a device will yield a positive power output even with optimally chosen fuels, but before we consider practical energy expenditures and losses, we must demonstrate that the chosen photocatalysts are competent at performing the proposed oxidation steps on the chosen fuels to minimize light energy input and maximize electron extraction from the fuel.

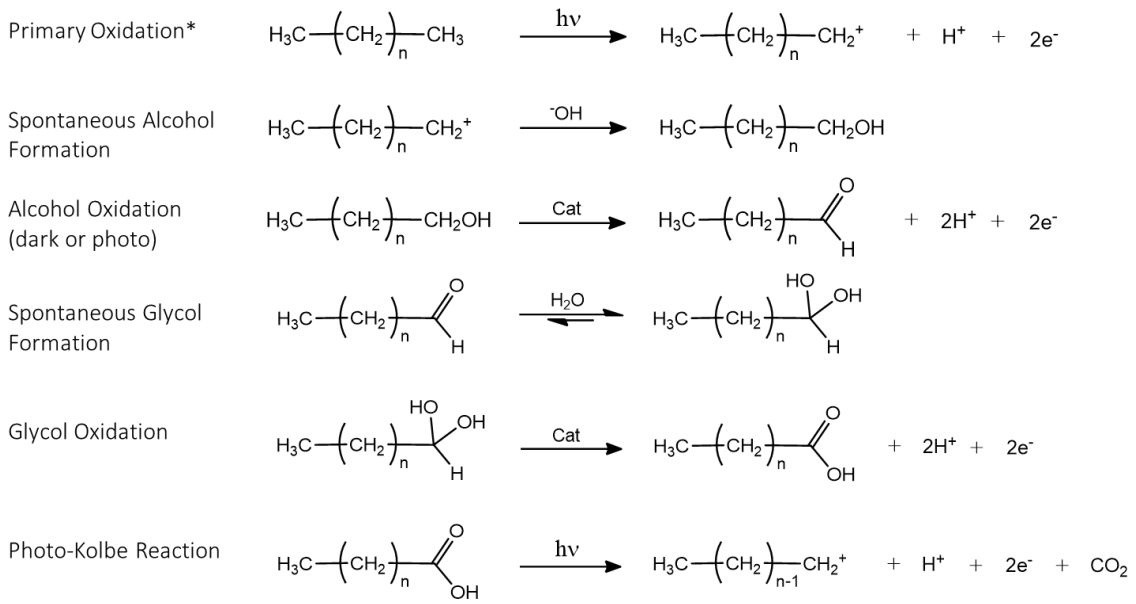

Figure 3-1 A proposed scheme for oxidizing hydrocarbons and minimizing light energy input. The guiding principles of the path are that continued oxidation of hydrocarbons leads to formation of the following series of molecule species: alcohols, aldehydes/glycols, carboxylic acids, and then alcohols again after decarboxylation. The species with high activation barriers to oxidation include the initial C-H activation and the C-C activation. Alcohols are quite often current doubling substrates, so oxidation from them may also be performed by a photoanode.

In using this proposed scheme, we first identify hurdles to complete oxidation of hydrocarbons which include stable intermediates and unwanted side reactions. Not explicitly stated but essential to the above scheme, we must also demonstrate the capacity for sequential oxidation wherein difficult to oxidize forms of the fuel are oxidized by the photoanode then subsequently oxidized downstream by thermal catalysts or electrocatalysts so as to minimize the necessity for light input. In the oxidation of n-alkanes, the expected hurdles are as follows: oxidation of the carbon chain through C-H activation, decomposition of the carbon chain via C-C activation, and sequential oxidation. The selectivity from these bond activations must also follow the proposed series of steps to ensure relative ease of downstream oxidations: the as mentioned C-H or

C-C bond activation, alcohol formation, alcohol oxidation to an aldehyde, aldehyde oxidation to a carboxylic acid, and decarboxylation via C-C activation leading to the formation of a smaller alcohol and progressively smaller carbon chains.

There are two types of side products that we have identified that we wish to avoid. Dimerization of singly oxidized substrates often occurs when using noble metal anodes or illuminated metal oxides to perform the oxidation. This is possible during both C-H bond and C-C bond activation with the latter known as the Photo Kolbe process.[10] In either case, continued oxidation of potential fuels would produce increasingly larger and more complex molecules that would prevent complete fuel consumption and foul the electrode surface.

Another unwanted reaction pathway after bond activation may occur during the two electron oxidation, alkene formation. Conditions selective for alkenes over alcohols will lead to downstream energy costs needed to activate the newly formed C=C double bonds. The goal of an efficient photo fuel cell device is to form progressively simpler and smaller molecules minimal energy input. Figure 3-2 outlines how an illuminated metal oxide, n-TiO_2, may be used in the proposed pathway. Here we simplify the oxidation steps by having all electrons collected by the conduction band of the semiconductor photoanode.

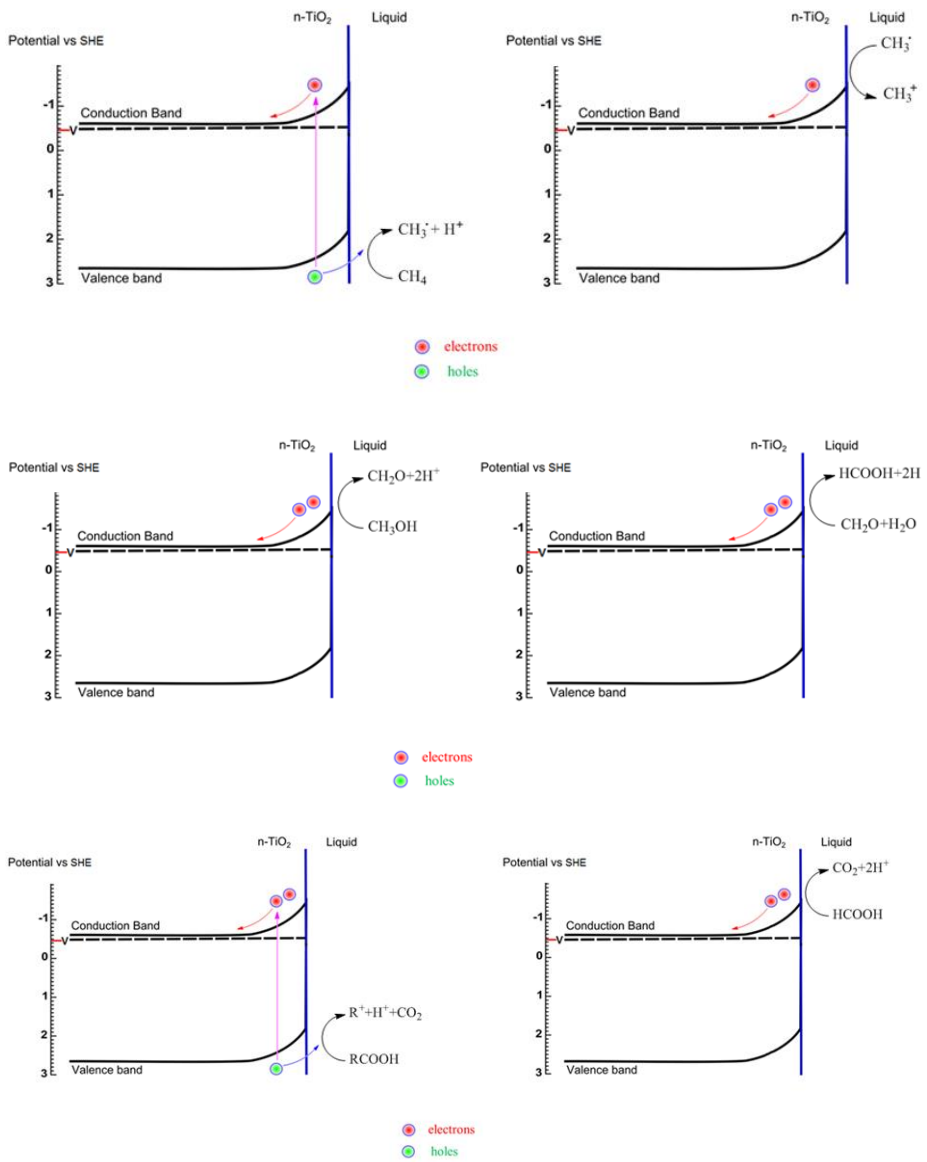

Figure 3-2 Oxidation steps using TiO_2 for the proposed scheme. Upon the initial oxidation of a hydrocarbon like methane, a high energy radical is formed wherein the species may perform current doubling by injecting its radical electron. In the presence of water or hydroxides, this cation will spontaneously form an alcohol. With the appropriate thermal catalysts, we may extract two electrons to form an aldehyde and two more to form the carboxylic acid. Two electrons per photoexcited hole may be collected via current doubling from the carboxylic acid.

In order to validate the proposed pathway, we must demonstrate that the

photoanode can overcome the identified hurdles in the oxidation of a simple hydrocarbon

which serves as our model fuel. While ethane and methane would seem like good candidate fuel molecules, the model fuel must be large enough to produce an alkene upon C-H activation and properly emulate larger hydrocarbon molecules. While ethane is large enough to undergo beta-hydride elimination upon C-H activation, for larger hydrocarbon molecules beta-hydride elimination takes place between the alpha carbon and a non-terminal second carbon. Similarly, upon decarboxylation, propionic acid/propionate creates a two-carbon species which only has terminal carbons. To emulate the oxidation of longer chain hydrocarbons, butyric acid/butyrate and propane have been selected as test molecules in the activation of C-C and C-H bonds, respectively. After these oxidation steps have been demonstrated, we also seek to demonstrate how multiple catalysts may participate in fuel oxidation to ensure the minimum number of photoexcitation events required to consume the fuel.

3.2 Discussion

C-C and C-H activation

We first focus on tackling the hurdles specific to the light driven oxidation steps. While C-C and C-H bond activation target different substrates, the experiments required to validate their steps in the overall scheme are the same. In both cases we share the common goal of oxidizing a model substrate to a C_3 alcohol via a two electron oxidation. The main side products that we actively seek to inhibit are alkenes which may be formed via beta hydride elimination and dimers which show up as a thick and often brown film on the electrode surfaces. We primarily wish to avoid alkenes as their double bonds require high energy input to activate as compared to O-H bonds in alcohols. Should we

be able to selectively form alcohols, they have the added benefit of having higher polar and thus have easier to target handles in downstream oxidation events.[11]

I began my investigation with the oxidative C-C activation of butyric acid and butyrate rather than the primary C-H activation of propane due to their much higher solubility in water over propane. I performed bulk electrolyses in 0.1 M H_2SO_4 aqueous media and 10 mM butyric acid with illuminated WO_3 electrodes and 0.1 M NaOH aqueous and 10 mM butyrate with illuminated p25 TiO_2 electrodes. No current multiplication or current increase was measured in these experiments after addition of butyric acid/butyrate. 10 mM butyric acid was added to 0.1 M H_2SO_4 aqueous solution with a WO_3 electrode serving as the photoanode. 10 mM sodium butyrate was added to 0.1 M NaOH solution with a TiO_2 electrode serving as the photoanode. N_2 was sparged through solution for more than five minutes before bulk photoelectrolyses which were performed under 2.4 mW/cm^2 of 365 nm illumination. The anode potential was held at 0.5 V vs Ag/AgCl. Below in Table 3-1 is a list of the as measured gas chromatography retention times for potential products from these studies and the chomatographs of working solution after having performed the bulk photoelectrolyses. Higher concentrations of OH^- facilitate the formation of alcohols, so it would be expected that oxidations in basic media are more likely to yield alcohols over acidic media.

Table 3-1 Retention times of expected compounds from the oxidation of butyric acid and propane. Bolded and italicized are the times for acetone, isopropanol, and n-propanol, which are likely products under aqueous conditions.

Analyte	Retention Time
propane	0.84
propylene	0.84
n-propyl ether	0.90
isopropyl ether	0.91
acetalydehyde	0.97
propionaldehyde	1.09
acetone	***1.13***
isopropanol	***1.59***
ethanol	1.64
n-propanol	***2.72***
propionic acid	~10.2
butyric acid	~14.1
acetic acid	~14.9

Below in Figure 3-3 and Figure 3-4 are chromatographs showing the profile of oxidation products from butyric acid in acidic media and sodium butyrate in alkaline media, respectively.

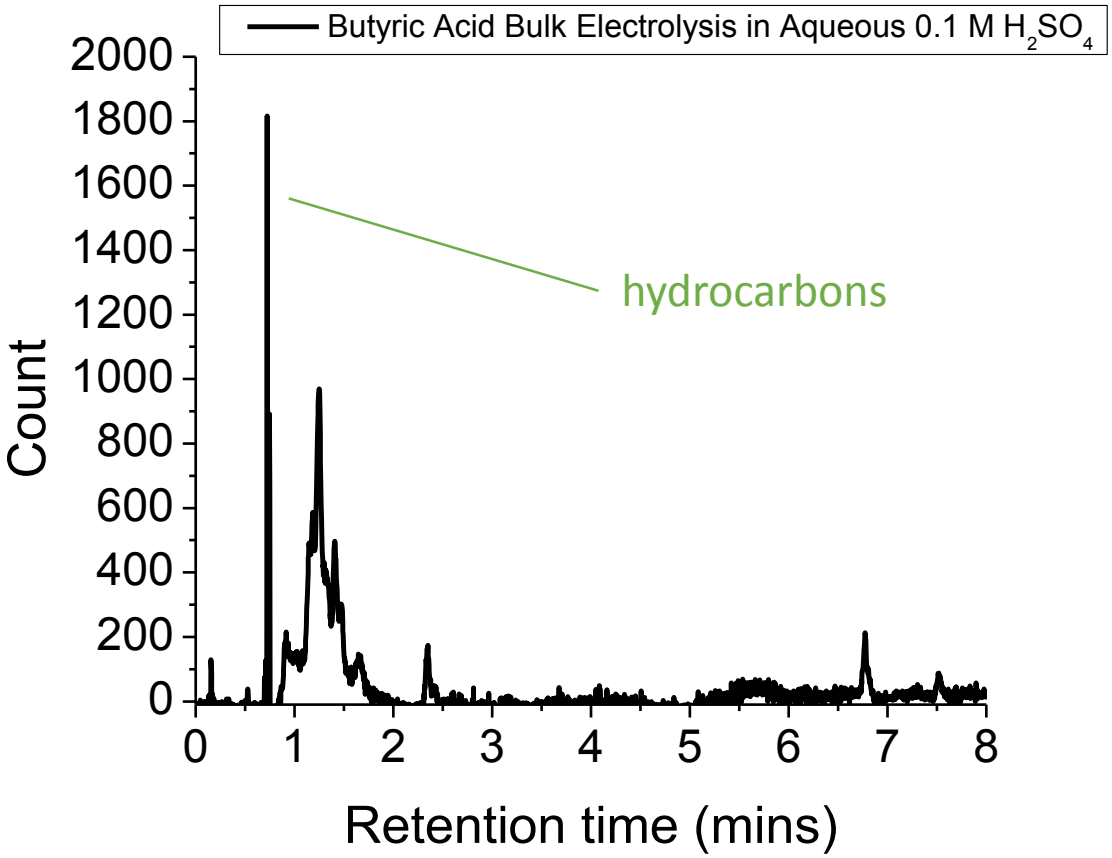

Figure 3-3 10mM butyric acid in 0.1M H_2SO_4 aqueous. 2.4 C of charge passed. The first tall peak corresponds to the retention time of hydrocarbons, alkanes and alkenes. No alcohols or ketones were detected in measurable quantities.

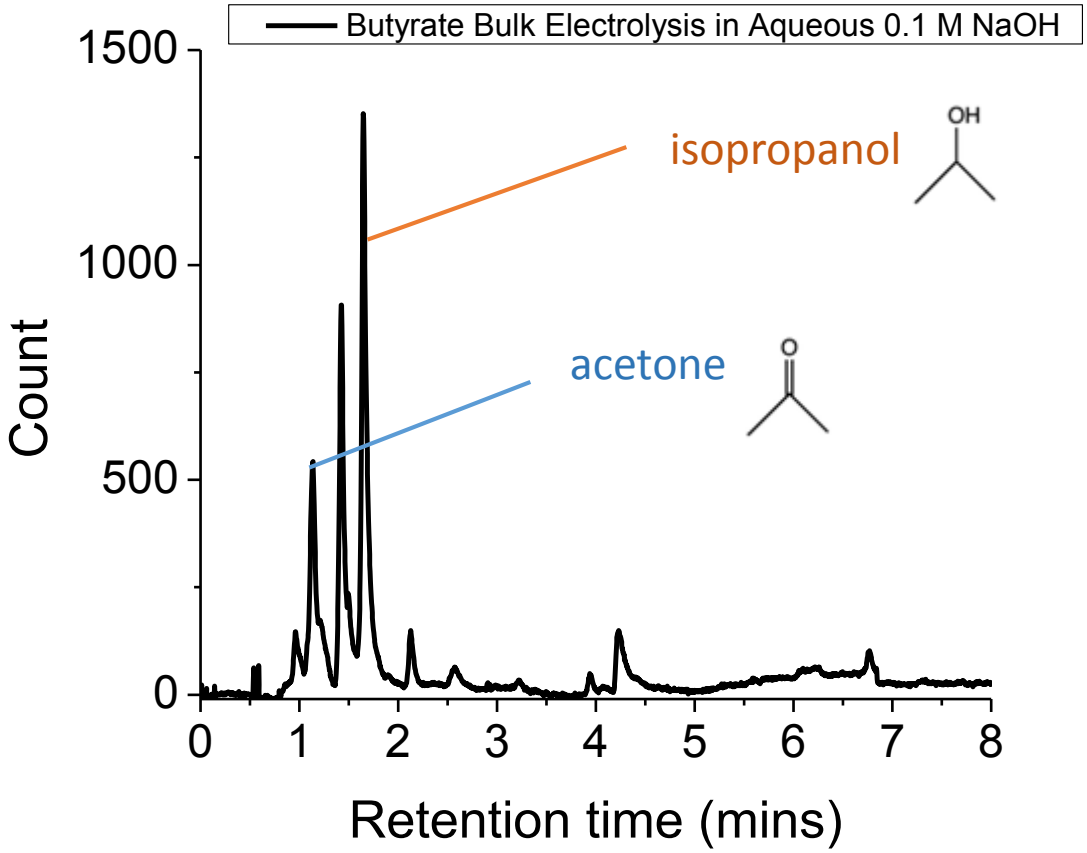

Figure 3-4 10mM butyric acid in 0.1M NaOH aqueous. First peak acetone, second peak identified as isopropyl acetate, third peak is isopropanol. The total charge passed was 1.54 C. The areas under the acetone and isopropanol peaks correspond to 2.1 micromoles and 2.0 micromoles in total working solution respectively. n, the number of electrons to form acetone is expected to be 4. n for isopropanol is expected to be 2. The total charge required to form these species is expected to be 1.19 C, which is consistent with the charge passed during the bulk electrolysis. No hydrocarbons were detected.

A variety of peaks corresponding to trace products were found in both chromatographs, but two of the major products from oxidizing butyrate with illuminated TiO_2 in basic media were isopropanol and acetone. Though these products are not explicitly along the proposed oxidation pathway, isopropanol is an oxidation intermediate that is more easily oxidized than propylene. Isopropanol, like methanol and ethanol, is an established current doubling substrate that forms acetone as its primary product. As

acetone is a detected product, a potential concern in the oxidation of acetone is aldol condensation on the surface of the metal oxide; however, in aqueous media, the aldol condensation reaction is suppressed by high concentrations of water via its back reaction.[12]

With the promising results from butyrate oxidation, I performed dissolved propane oxidation under similar alkaline conditions to test whether or not similar products could be produced. Propane (98% purity) was sparged into 0.1 M NaOH solution for five minutes and bulk photoelectrolysis was performed under 2.4 mW/cm^2 365 nm illumination. The TiO_2 photoanode potential was held at 0.5 V vs Ag/AgCl. Isopropanol and acetone were again detected in the working solution as shown in Figure 3-5.

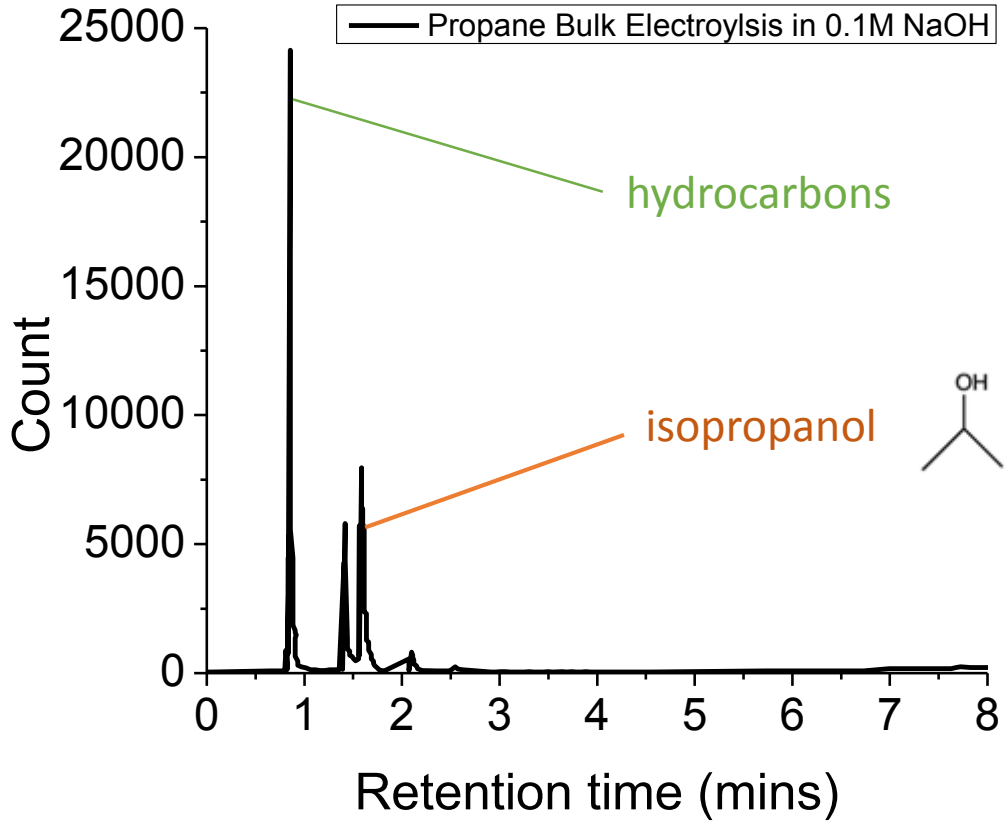

Figure 3-5 Saturated propane oxidation in 0.1M NaOH aqueous. First peak is propane, and third peak is isopropanol. Second peak remains unidentified. The total charge passed was 1.4 C. The areas under the isopropanol peaks corresponds to 3.0 micromoles in solution. The total charge required to form isopropanol from propane is expected to be 0.57 C, which corresponds to some lost charge likely to water oxidation.

As can be seen from the above chromatograph, a similar profile of primary products was detected. To our knowledge this is the first time acetone or isopropanol have been found as primary products in the oxidation of propane in ambient temperatures and pressures. Along with this demonstrated capacity for TiO_2 to isopropanol and acetone from oxidizing propane, it is worth noting that propane has been previously reported as a current doubling substrate on TiO_2 in nonaqueous environments where CO_2 was detected as an oxidation product.[13] In this study, current multiplication was curiously not detected

in the oxidation of ethane and methane. The authors concluded that propane or higher order alkanes are necessary for sufficient surface interaction with TiO_2 to yield its second unpaired electron after an initial oxidation. Conditions that selectively produce alcohols from oxidizing propane have to our knowledge not been previously reported. Though pH 13 aqueous media provides a lower solubility for propane than the concentrated triflic acid monohydrate solution used in the aforementioned studies, it is clear from the product distribution in Figure 3-5 that a solubility of propane in water of 0.9 mM is sufficient to yield valuable oxidation products via bulk photoelectrolysis.

Sequential Oxidation, Close Proximity Photoanode and Dark Anode Electrodes

If we were to use the photoanode for all fuel oxidation steps, we would be limited to at best two electrons per photoexcitation as per the previously described current doubling mechanism. One way to overcome this limit is to introduce an additional electrode capable of performing downstream oxidations without the need for light. Our proposed implementation uses dark heterogeneous catalysts together with the metal oxide photoanodes, as pictured below in Figure 3-6. I chose gold for the dark anode material due to its high resistance to fouling while in the presence of carbon monoxide or while performing formaldehyde oxidation as compared to platinum and other noble metals.[14,15] Separation of these two anode materials is essential. While there are some benefits to metal deposition directly onto metal oxide surfaces, electrons are usually trapped in these metal sites. Without the presence of oxygen to extract these electrons, charge recombination at the metal/metal oxide interface occurs leading to net energy losses.[16] In other words, the dark catalyst's electronic states reside in the middle of the

semiconductor band gap and act as electron trap sites too energetically low to transfer electrons to the semiconductor conduction band but high enough to allow holes and electrons to recombine. In our proposed implementation, both the gold and metal oxide materials would share a back contact but remain spatially separated.

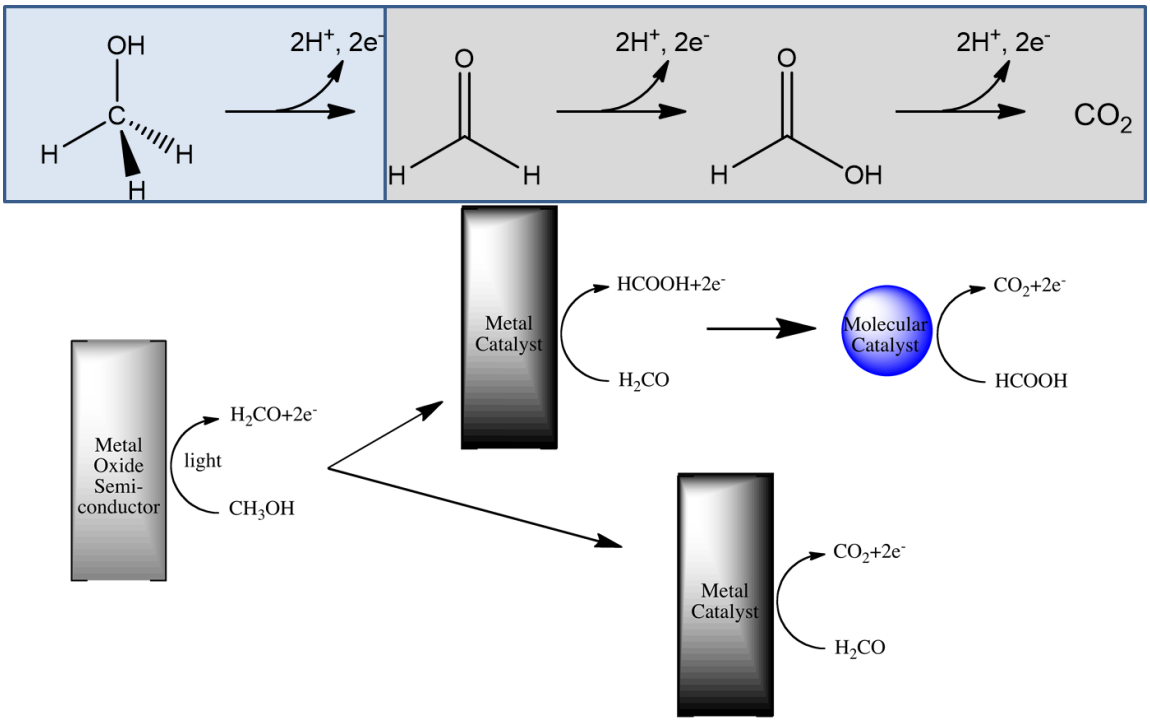

Figure 3-6 Sequential oxidation via multiple catalysts. Methanol may be current doubled at the metal oxide to form formaldehyde. Formaldehyde may be either completely oxidized by a metal catalyst to CO_2 or to formate which may then be oxidized by another catalyst such as a molecular homogeneous electrocatalyst.

Since the oxidation of methanol may be performed directly by gold at potentials approaching 0.5V vs Ag/AgCl, we wish to demonstrate that photoelectrooxidation of methanol may lead to the formation of formaldehyde which may then be oxidized at less anodic potentials.[14] I first fabricated gold electrodes by sputtering ~500 nm of gold onto glass slides followed by a mild polishing with standard electrode polishing pads. To keep the two types of electrode materials in close proximity as a means to capture downstream

substrate intermediates on the dark catalyst, in the electrochemical cells, I separated gold electrodes from the TiO_2 electrodes using a strip of Teflon tape of 0.3mm thickness as a spacer. The gold electrodes showed no photoresponse under illumination with the UV LED without the presence of a photoelectrode. Electrode areas for both the dark anode and photoanode were 1cm x 1cm. The desired reaction steps we wished to demonstrate are pictured in Figure 3-7.

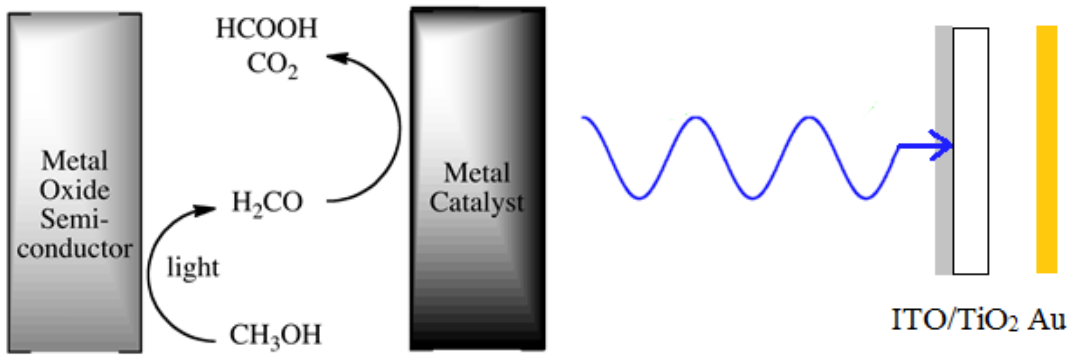

Figure 3-7 Close proximity sequential oxidation as performed with p25 TiO_2 and gold electrodes. The photoanode is back illuminated through a glass/ITO.

In an attempt to minimize downstream oxidation of formaldehyde and formate by the photoanode, I modulated the light used to back-illuminate the TiO_2 with a sinusoidal signal. The initial goal was to evaluate whether or not a net increase in dark current was possible when using discrete periods of reduced light intensity which would allow oxidation intermediates from the photoanode to diffuse away from the electrode to the dark anode. Both the photoanode and gold anode were held at 0V vs Ag/AgCl and current from each was measured independently.

An unexpected consequence of applying light modulation to the close proximity electrodes was the discovery that illumination of the TiO_2 and therefore a photovoltage at

its surface leads to a direct attenuation of the effective surface potential of the gold electrode as evidenced by the sinusoidal “dark” current depicted in Figure 3-8. Anodic photovoltage becomes competitive by creating an electric field that suppresses the anodic potential of the gold. As is clear from Figure 3-8, the photocurrent at the TiO_2 electrode and dark current of the gold electrode are synced with each other. One may use the phase offset between the gold current and the photocurrent to discern whether current at the gold surface is faradaic or capacitive. Without the presence of methanol, gold current remains small in the nanoamperes scale. A 10x magnification of the current is included in the figure to help visualize the 90° phase offset indicative of purely capacitive current. Once methanol has been added to the electrolyte, formaldehyde and/or formate are formed at the photoanode and diffuse downstream to the gold. The gold current becomes 180° out of phase with the photocurrent demonstrating that its voltage is suppressed when the photoanode is illuminated and that the dark current must be faradaic. The suppression of the gold potential under illumination demonstrates that minimizing light via pulsing or other types of signal modulation must be used in the optimization of current collection by the dark anode. Further implications of this result and other implementations of light intensity shaping will be discussed later in Chapter 5.

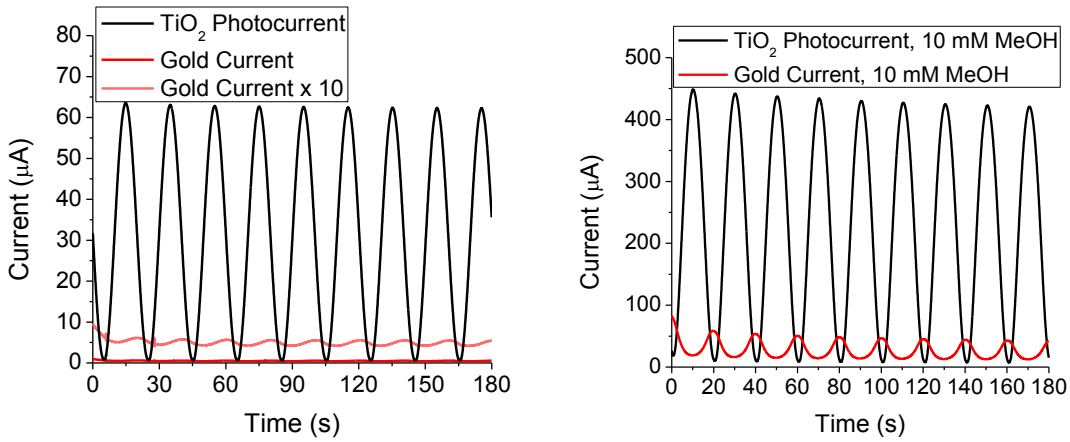

Figure 3-8 Photocurrent from intensity modulated photoelectrolysis with close proximity sequential oxidation as performed with p25 TiO_2 and gold electrodes. The potential at the gold surface is negatively attenuated by the photovoltage at the photoelectrode. Without the presence of methanol, formaldehyde is not formed and at 0 V vs Ag/AgCl gold has nothing to oxidize and all current at the gold electrode is capacitive as indicated by the low amplitude and out of phase current. In the presence of methanol and after illumination, formaldehyde is formed and in-phase faradaic current is observed at the gold electrode. Illumination intensity was centered at 2.4 mW/cm^2 of 365 nm light and was modulated with an amplitude of 2.4 mW/cm^2.

Sequential Oxidation, Rotating Ring Disk Electrochemistry

While it is clear that oxidation downstream of the photooxidation is possible, we also seek to quantify the limits of sequential catalysis in the oxidations of methanol and formaldehyde. A powerful tool in probing sequential charge transfer events is rotating ring disk electrochemistry (RRDE) as described in Chapter 1. To probe formaldehyde oxidation by a secondary gold electrode I used a BASi RRDE electrode shaft with interchangeable disks and fabricated a p25 electrode film coated custom titanium disk. I made various attempts at creating stable TiO_2 electrodes, but the most robust and well behaved TiO_2 disk was the simplest involving a simple dropcast and annealing of a p25 suspension onto a titanium chuck. The ring electrode was made of polished gold with an inner radius of 0.225 inches and outer radius of 0.350 inches. According to equation E1-

4 this would yield an ideal current ratio between the ring and disk electrodes of 0.255 assuming n_{disk} and n_{ring} are the same. The current response under disk voltage sweeping and with varied rotation rates are shown below in Figure 3-9.

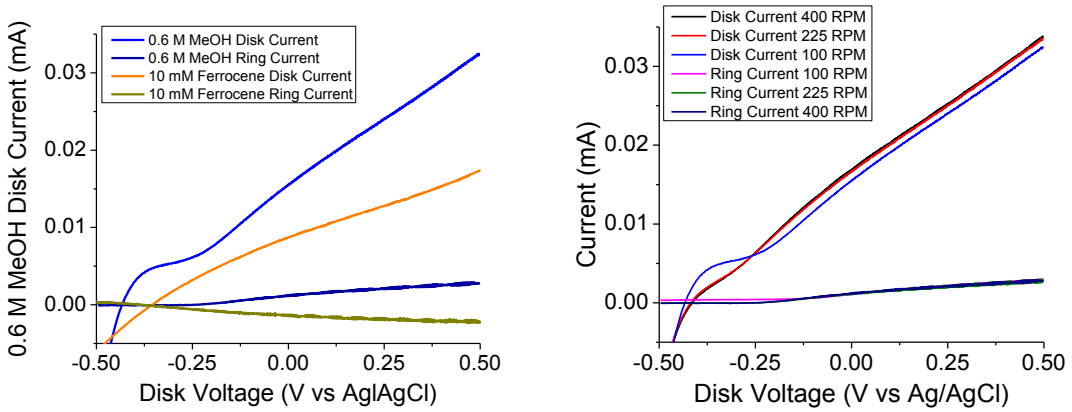

Figure 3-9 Rotating ring disk electrochemistry with illuminated TiO_2 Disk/Au Ring and 20 mV/s scan rate. *(Left)* A comparison of current vs applied disk voltage at 400 RPM for 10 mM ferrocene sequential oxidation then reduction (orange and gold) and 0.6 M methanol oxidation then oxidation (blue and dark blue). Note that the gold current is negative because it represents ferrocenium reduction. Ferrocene scans were performed in 0.1 M $TBAPF_6$ acetonitrile with the ring potential held at 100 mV vs Ag/AgCl. Methanol scans were performed in 0.1 M NaOH aqueous with a ring voltage held at 0.0 V vs Ag/AgCl. As measured, the current ratio with ferrocene, $N_{Ferrocene}$, is 0.123 and the current ratio with methanol, $N_{Methanol}$, is 0.084. $N_{Theoretical}$ is 0.255 for the given electrode geometries. *(Right)* Methanol scans performed with varying rotation rates show both photocurrent and ring current have no rotation rate dependence. Increased rotation implies increased mass transport of analyte to the electrode, but photocurrent in this experiment is limited by light intensity and not substrate availability.

Two immediate results are revealed from these voltage sweeps. First, current at both electrodes is independent of rotation rate once a sufficient rotation rate is reached. Photocurrent is limited by light intensity and not substrate availability and the proportion of ring current to disk current is only a function of geometry. One may note that the ratio when using methanol is approximately 33% of the current ratio when using ferrocene. This suggests that the TiO_2 disk consumes some of the formaldehyde it produces before it can reach the ring. Both current ratios, N, are lower than the theoretical current ratio,

0.255. This suggests that the non-planarity of the disk plays a role in the lower yield by hindering diffusion from the disk electrode to the ring electrode. Figure 3-10 shows how typical behavior of the one electron oxidation of ferrocene and subsequent reduction of ferrocenium as a function of rotation rate as performed on the same electrode with the disk replaced with a standard planar gold disk.

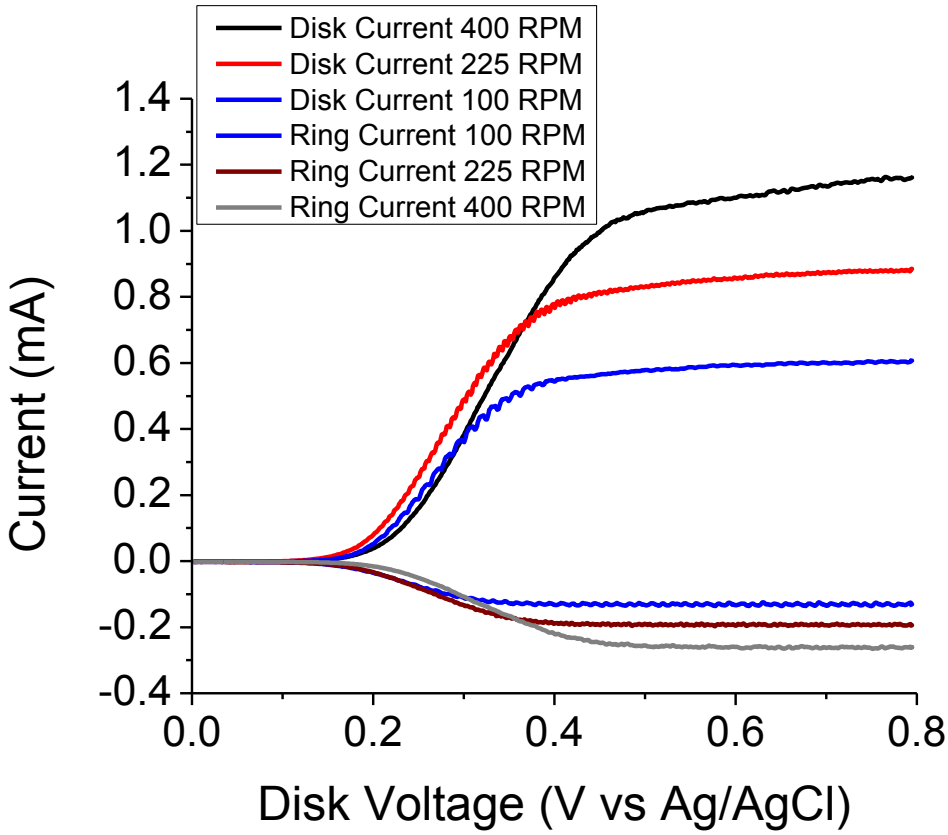

Figure 3-10 Rotating ring disk scans of ferrocene with Au Disk/Au Ring. Solution conditions 0.1 M $[Et_4N]BF_4$ in acetonitrile. Scans were performed at 20 mV/s. The theoretical current ratio is 0.255. Measured current ratio is 0.22.

It is unclear from these results whether or not induced mass transport or close electrode proximity are sufficient to ensure the majority of oxidation steps take place downstream away from the illuminated photoanode.

3.3 Methods

Making Electrodes

The electrodes used in this chapter were fabricated via spin coating nanoparticle TiO_2 and electrodepositing nanoparticle WO_3 onto conductive back contacts. FTO, ITO, Ag, Ti were used as back contacts as all these materials demonstrated ohmic behavior when using these forms of WO_3 and TiO_2. ITO and FTO on glass were used as purchased from Sigma Aldrich for back illumination experiments. Ti and Ag back contact films were deposited onto glass slides via sputtering. All surfaces were degreased via sonication in a series of water, isopropanol, and methanol before material deposition. Once the films were annealed, onto the back contact surfaces, a circular area of active semiconductor surface on all electrodes was left uncovered while the rest was sealed with an inert Loctite 1C Hysol epoxy to prevent contact between solution and inactive parts of the electrode.

Gold Film Electrodes

Gold coated slide electrodes were created by first degreasing glass slides via sonication in a series of water, isopropanol, and methanol. 500 nm of gold was subsequently deposited via sputtering or thermal evaporation. Gold coated slides were cut into 1 cm x 1.5 cm chips. Silver conductive paint was used to form a contact along the edge of a gold film that coated around to the opposite side of the glass chip. A wire lead was attached to the edge of the conductive silver film, and both the wire and the silver paint were coated with a Hysol 1C epoxy to prevent direct contact of the wire or the silver with working solution. 1 cm x 1 cm square below the wire lead was left revealed to solution after wrapping the lead 1 cm x 0.5 cm portion with Teflon tape.

TiO_2 Nanoparticle Film Electrode Fabrication

For TiO_2 films, commercially available p25 TiO_2 was purchased from Degussa. The material is comprised of a mixture of rutile and anatase phase nanoparticles with an average diameter of 25 nm. A suspension of 400 mg of p25 nanoparticles in 5 mL of 50%v/v ethanol and water was cast onto the back contacts at 500 RPM for 5 seconds followed immediately by spinning the stage at 1500 RPM for another 60 seconds or until the film is uniform and solvent evaporated. I left one edge of the back contact surface revealed so as to later attach a wire lead. The as deposited material was placed into a 500°C tube furnace open to atmosphere for three hours to anneal the film to the back contact and the nanoparticles to each other.

WO_3 Nanoparticle Film Electrode Fabrication

WO_3 electrodes were made as per literature.[17] A solution of peroxytungstic acid (50 mM) in 30% (v/v) isopropanol/water was stirred at room temperature for 24 hours in the presence of a Pt mesh. The Pt mesh and isopropanol reduced the concentration of free H_2O_2. An FTO slide was then immersed in the peroxytungstic acid solution to a depth of 1.0 cm, and cathodic electrodeposition was performed in quiescent solution at -0.50 V vs. Ag/AgCl to produce a passage of charge density of -0.25 C/cm^2 at a current density of approximately -0.3 mA/cm^2. The sample was then removed, rinsed with water and ethanol, then heated in air at 275°C for 10 minutes. The deposition cycle was completed three times. The sample was annealed at 500°C in air for an hour yielding an approximate WO_3 film thickness of 300 nm.

Bulk Photoelectrolyses

Photoelectrolyses were performed using a custom Teflon electrochemical cell with quartz windows. Photoelectrodes were placed within the working solution 1 cm from the illumination sourceFor photoelectrolyses using WO_3 and TiO_2 photoanodes, 0.1 M H_2SO_4 and 0.1 M NaOH aqueous solutions were used, respectively. 10 mM of butyric acid or 10 mM sodium butyrate was then added. Prior to decarboxylation electrolyses, working solution was sparged with N_2 or Argon gas to remove oxygen. For propane oxygen, 98% propane was sparged for five minutes before cell was sealed just before photoelectrolyses.

For all photoelectrolyses, were illuminated under 2.4 mW/cm^2 illumination intensity from a 365 nm LED purchased from Thor Labs and light intensity was measured by an Ophir PD300 silicon photodiode sensor.

Gas Chromatography Liquid Samples

A DB-Wax column installed in an HP5890 Series II Gas Chromatography instrument with N_2 carrier gas and hydrogen flame FID was used to detect and quantify liquid phase products. A sample of working solution was neutralized and 0.5 µL of solution was injected into the inlet.

Proximity Au/TiO_2 Electrode Simultaneous Oxidation

A custom gas tight glass cell with quartz windows was used to allow multiple working electrodes. The gold coated slide electrode was held in close proximity to and separated from the p25 TiO_2 on ITO photoelectrode using 300 µm thickness PTFE tape. The photoelectrode was back-illuminated under 2.4 mW/cm^2 illumination intensity from a 365 nm LED purchased from Thor Labs and light intensity was measured by an Ophir PD300

silicon photodiode sensor. An Ag/AgCl electrode separated by a vycor tip was used as a reference and a glassy carbon rod was used for the auxiliary electrode. Electrochemical experiments used a Pine bipotentiostat that independently controlled the voltages and monitored the currents of both the gold and TiO_2 electrodes. Electrolytic solutions were 0.1 M NaOH aqueous and methanol oxidation experiments were performed with 10 mM MeOH added.

In the light modulation experiments, a LED controller was modulated via an external function generator such that the effective illumination intensity was centered at 2.4 mW/cm^2 of 365 nm light and was modulated with an amplitude of 2.4 mW/cm^2. Both electrodes were held at 0 V vs V vs Ag/AgCl, which was chosen to prevent undesirable electric fields to be maintained between the electrodes and allow formaldehyde oxidation to take place at the Au electrode but prevent direct methanol oxidation at the Au surface.

Rotating Ring Disk Electrode Construction

A commercial Pine ring disk electrode shaft that could be fitted with interchangeable disk-electrodes was used. Disk electrodes have a radius of 0.200 inches and the gold ring electrode has an inner radius of 0.225 inches and an outer radius of 0.350 inches. For standard RRDE experiments, a gold coated disk that comes standard with the shaft was used, while for photoelectrochemical experiments, a custom photoelectrode disk was created. The photoactive disk material, the p25 TiO_2 film, was deposited onto a machined titanium chuck by dropcasting 200 µL of 20 mg/mL mixture of p25 TiO_2 in 1:1 ethanol/water onto a Ti chuck of radius 0.200 inches. The coating was left to dry in the dark and was annealed at 300°C for 30 minutes in a quartz tube furnace in air to promote

inter-particle annealing, surface attachment, and Ti oxidation to form a metal-passivating TiO_2 surface on the chuck.

Rotating Ring Disk Electrode Experiments

Prior to all electrochemical experiments, the working solution was sparged with N_2 or Argon gas to remove oxygen, and a small positive pressure was maintained to exclude air.

A commercial Pine rotating ring disk rotator and controller were used to spin the electrode shaft and a Pine bipotentiostat with computer console was used for electrochemical measurements. A 250 mL round bottom three neck flask served as the electrochemical cell with PTFE septa used to exclude air. An Ag/AgCl wire was used as the reference electrode. Platinum wire was used as the auxiliary.

For ferrocene reduction/oxidation experiments, 0.1 M NBu_4PF_6 in acetonitrile was used as the electrolytic solution. 10 mM ferrocene was added to solution. For methanol oxidation experiments, 0.6 M MeOH and 0.1 M NaOH aqueous was used. The photoelectrode was illuminated from the base by a collimated 365 nm photodiode light source at a distance of 1 cm below the glass flask. The power output for the photodiode and the electrode height was adjusted to maintain an incident power density on the photoelectrode of 1.0 mW/cm^2 as measured by an Ophir PD300 photodiode power sensor.

3.4 Conclusions

While WO_3 has proven to be a stable photoanode capable of current multiplication using various substrates, the approach that we have taken requires not just

a robust current multiplying anode but a medium that facilitates the further downstream oxidation and mineralization of fuels. WO_3 is most active in acidic media, but higher acidity leads to unwanted products like alkenes that require additional input energy to oxidize. Illuminated TiO_2 in basic media continues to be a promising system for oxidizing fuels and produce easily oxidized intermediates, isopropanol and acetone, but we must continue to increase the yields of those reaction intermediates and prevent them from being consumed by the photoanode. Of additional note, I found that voltage crosstalk between the photoanode and dark anode lowers the effective voltage at the dark anode thus inhibiting oxidative current.

While not specific to the fuel cell objective, the results outlined here demonstrate an important synthetic result, specifically the selectivity for alcohols and ketones from the oxidation of carboxylates and alkane chains using illuminated TiO_2 in alkaline aqueous media. This synthetic method is worth investigating on its own merits and could prove useful to commercial synthetic processes.

3.5 Acknowledgements

Much of the material in this chapter is related to a patent “Photoassisted high efficiency conversion of carbon-containing fuels to electricity” with shared invention ownership by Clifford P. Kubiak, Mark J. Llorente, Nathan S. Lewis, Robert H. Coridan, and Anna R. Beck.

3.6 References

1 Olah, G. A. Beyond Oil and Gas: The Methanol Economy. *Angewandte Chemie International Edition* **44**, 2636-2639, doi:10.1002/anie.200462121 (2005).

2 Shao, Z., Haile, S. M., Ahn, J., Ronney, P. D., Zhan, Z. & Barnett, S. A. A thermally self-sustained micro solid-oxide fuel-cell stack with high power density. *Nature* **435**, 795-798, doi:http://www.nature.com/nature/journal/v435/n7043/suppinfo/nature03673_S1.html (2005).

3 Zhou, Z. F., Gallo, C., Pague, M. B., Schobert, H. & Lvov, S. N. Direct oxidation of jet fuels and Pennsylvania crude oil in a solid oxide fuel cell. *Journal of Power Sources* **133**, 181-187, doi:http://dx.doi.org/10.1016/j.jpowsour.2003.12.044 (2004).

4 Anpo, M. & Kamat, P. V. *Environmentally benign photocatalysts: applications of titanium oxide-based materials*. (Springer Science & Business Media, 2010).

5 Solarska, R., Santato, C., Jorand-Sartoretti, C., Ulmann, M. & Augustynski, J. Photoelectrolytic oxidation of organic species at mesoporous tungsten trioxide film electrodes under visible light illumination. *Journal of Applied Electrochemistry* **35**, 715-721, doi:10.1007/s10800-005-1400-x.

6 Ni, X., Ye, J. & Dong, C. Kinetics studies of methyl methacrylate photopolymerization initiated by titanium dioxide semiconductor nanoparticles. *Journal of Photochemistry and Photobiology A: Chemistry* **181**, 19-27, doi:http://dx.doi.org/10.1016/j.jphotochem.2005.10.021 (2006).

7 Alizadeh Fard, M., Aminzadeh, B. & Vahidi, H. Degradation of petroleum aromatic hydrocarbons using TiO2 nanopowder film. *Environmental Technology* **34**, 1183-1190, doi:10.1080/09593330.2012.743592 (2013).

8 Jia, C., Wang, Y., Zhang, C. & Qin, Q. UV-TiO2 Photocatalytic Degradation of Landfill Leachate. *Water Air Soil Pollut* **217**, 375-385, doi:10.1007/s11270-010-0594-7 (2011).

9 Vargas, R. & Núñez, O. Photocatalytic degradation of oil industry hydrocarbons models at laboratory and at pilot-plant scale. *Solar Energy* **84**, 345-351, doi:http://dx.doi.org/10.1016/j.solener.2009.12.005 (2010).

10 Klocke, E., Matzeit, A., Gockeln, M. & Schäfer, H. J. Electroorganie Synthesis, **55[1]**. Influences on the Selectivity of the Kolbe versus the Non-Kolbe Electrolysis in the Anodic Decarboxylation of Carboxylic Acids. *Chemische Berichte* **126**, 1623-1630, doi:10.1002/cber.19931260720 (1993).

11 Sánchez, V. M., de la Llave, E. & Scherlis, D. A. Adsorption of R−OH Molecules on TiO2 Surfaces at the Solid−Liquid Interface. *Langmuir* **27**, 2411-2419, doi:10.1021/la103511c (2011).

12 El-Maazawi, M., Finken, A. N., Nair, A. B. & Grassian, V. H. Adsorption and Photocatalytic Oxidation of Acetone on TiO2: An in Situ Transmission FT-IR Study. *Journal of Catalysis* **191**, 138-146, doi:http://dx.doi.org/10.1006/jcat.1999.2794 (2000).

13 Harima, Y. & Morrison, S. R. Current doubling during propane oxidation on the n-TiO2 anode in trifluoromethanesulfonic acid monohydrate. *Journal of Electroanalytical Chemistry and Interfacial Electrochemistry* **220**, 173-177, doi:http://dx.doi.org/10.1016/0022-0728(87)88013-0 (1987).

14 Ureta-Zañartu, M. S., Berríos, C., González, T., Fernández, F., Báez, D., Salazar, R. & Gutiérrez, C. Electrocatalytic oxidation of alcohols at gold electrodes in alkaline media. *Int J Electrochem Sci* **7**, 8905-8928 (2012).

15 Habibi, B. & Delnavaz, N. Electrocatalytic oxidation of formic acid and formaldehyde on platinum nanoparticles decorated carbon-ceramic substrate. *International Journal of Hydrogen Energy* **35**, 8831-8840, doi:http://dx.doi.org/10.1016/j.ijhydene.2010.05.129 (2010).

16 Subramanian, V., Wolf, E. E. & Kamat, P. V. Catalysis with TiO2/Gold Nanocomposites. Effect of Metal Particle Size on the Fermi Level Equilibration. *Journal of the American Chemical Society* **126**, 4943-4950, doi:10.1021/ja0315199 (2004).

17 Mi, Q., Zhanaidarova, A., Brunschwig, B. S., Gray, H. B. & Lewis, N. S. A quantitative assessment of the competition between water and anion oxidation at WO3 photoanodes in acidic aqueous electrolytes. *Energy & Environmental Science* **5**, 5694-5700, doi:10.1039/C2EE02929D (2012).

Chapter 4

Paired electrolysis in the simultaneous upgrading of two renewable carbon feedstocks

4.1 Introduction to Paired Electrolysis

In the pursuit of sustainable chemistry, electrolysis reactions are becoming more prevalent because they use electrical energy as the driving force for chemical transformations that maximize atom economy.[1-3] While such reactions are growing in importance, many of them optimize the efficiency of atom usage without paying similar attention to optimizing the use of energy. Every electrochemical process may be thought of as a complete reaction split into two half-reactions, reduction and oxidation. This fact may be leveraged to allow two desirable half-reactions to be performed simultaneously. In this way, a thoughtful combination of half-reactions may be used to maximize the amount of useful product generated from an electrolysis thereby maximizing the energy efficiency of the reaction. To date, a number of paired electrochemical reactions of this type have been successfully accomplished.[1] Yet in spite of this success, paired electrochemical reactions remain limited in scope and greatly underutilized by the larger synthetic community. Much of this neglect can be attributed to a desire to carefully choose half reactions based on their complementarity, out of convenience, specific product compatibility, or a demand for voltage minimization. In other words, the half

reactions in a paired electrolysis are selected because of the manner in which they fit each other. However, this does not need to be the case. In a constant current (galvanostatic) electrolysis, the working potential of both the anode and cathode automatically adjust to the potential of the substrates in solution. Hence, any oxidation or reduction reaction may be paired with any other reduction or oxidation reaction. A paired electrolysis does not need to be developed around specifically matched half reactions but instead can be designed around synthetic needs for larger chemical processes. Rather than look for specific redox reactions to be paired, we may look to use paired electrochemical reactions to improve the sustainability of a wide variety of synthetic transformations. Consider the example illustrated in Scheme 1. In this paired electrochemical reaction, two reactions were selected because of their use in the larger effort to valorize biomass. The anodic reaction converts syringaldehyde derived from the lignin in raw sawdust into a "privileged" benzimidazole building block for a variety of applications.[4] The cathodic reaction generates carbon monoxide from carbon dioxide so as to treat CO_2 as a source for synthetic reagents.[5-9] the half-reactions represent part of a larger synthetic effort toward sustainable chemistry and were not selected to optimize the efficiency of one half-reaction or because of their specific complementarity.[1,10,11] They were selected for how they fit within a larger synthetic effort.

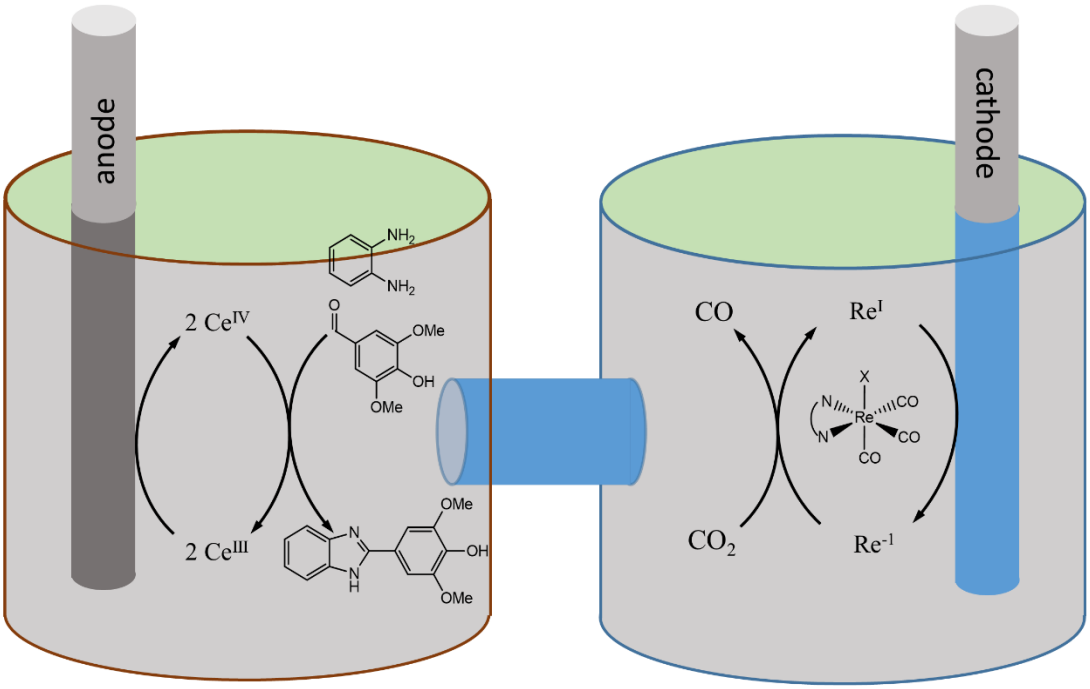

Figure 4-1 A simplified diagram depicting the half-reactions studied in this paper using a 2-compartment cell. Ceric ammonium nitrate (CAN) acts as the mediating electrocatalyst for the benzaldehyde diamine condensation reaction which releases protons into solution. Re(4,4′-di-tert-butyl-2,2′-bipyridine)$(CO)_3Cl$ (Re(bipy-tBu)$(CO)_3Cl$) acts as the electrocatalyst for the selective conversion of protons and CO_2 to CO and H_2O.

While synthetically driven paired electrolyses of the type illustrated in Figure 4-1 are easy to design in terms of a proof of principle experiment, they are not necessarily ideal from an energetic standpoint. The energy required to run the cell is to a large extent dictated by the synthetic transformations that need to be accomplished. But, this does not mean that the energy of the electrolysis should not be optimized. Optimization of the energy associated with the electrochemical cell is essential for practical application of the reaction. So, how does one optimize the efficiency and hence sustainability of a paired electrochemical reaction selected solely for synthetic utility? One must look to choosing

reaction conditions for the two half-reactions that optimize reaction rates with respect to applied voltage.

As electricity may be readily sourced through renewable means, the primary challenges` for a sustainable electrochemical process may be enumerated as (1) sustained electrolysis, (2) high Faradaic yield, (3) optimized power conversion efficiency, (4) current matching of the anodic and cathodic half-reactions, (4) chemical compatibility between half-reactions, (5) formation of products with higher value than the chemical substrates, (6) and renewably sourced chemical feedstocks. In this chapter we will discuss how these goals can be addressed in the context of the example paired electrochemical reaction shown above. This pairing lowers the minimum applied cell potential for the reaction to 2.3 V compared to 2.9 V using OER, and dramatically increases the efficiency of input energy by producing useful products at both half-reactions. Herein, we define the electrochemical parameters that need to be addressed in order to optimize the performance of the electrochemical cell for such a paired electrolysis and to power such an electrolysis by a photovoltaic.

For a complete electrolysis reaction, the total voltage at steady-state may be treated as the sum of the voltages from different parts of the cell as can be seen in equation E4-1 where $V_{\text{Cell-Resistance}}$ is the sum total of all resistances including separator and solution resistance.[12] In practice, the voltage required to drive each half-reaction may be measured against reference electrodes as shown in equation E4-2. In cells that require a membrane or frit to separate the compartments, a substantial cell resistance arises from the compartment separator. The resistance is dependent on the choice of electrolyte, separator material, and separator dimensions. In a cell that exhibits constant cell

resistance, R_{Series}, between the anode and cathode such as the cells used in this study, we may approximate the term $V_{Series\text{-}Resistance}$ with a linear term, IR_{Series}, using Ohm's law where I is the total current passed through the cell. In this regime we may characterize the entire cell voltage as comprised of the two voltages that drive the half-reactions and the linear resistance term.

$$V_{Total}=[V_{Anode}-V_{Cathode}]+V_{Cell\text{-}Resistance} \quad \textbf{E4-1}$$

$$V_{Total}=[(V_{Anodic}-V_{Reference}) - (V_{cathode}-V_{Reference})]+V_{Cell\text{-}Resistance} \quad \textbf{E4-2}$$

We first start with investigating the electrochemistry of the individual half-reactions before focusing on the pairing of the two.

4.2 Electrochemical Upgrading of CO_2 and a Lignin Derived Aromatic

A custom Teflon cell was used in preliminary cyclic voltammetry (CV) experiments to characterize the mechanism by which the condensation half-reaction takes place. A mixed solvent system of 8:3:1 CH_3CN:THF:MeOH with 0.8 M Et_4NBF_4 supporting electrolyte was used to ensure solvation of substrates and anodic product, and to maintain the proton concentration required for the cathodic reaction.[13,14] With methanol acting as a weak Brønsted acid, the proton concentration in either half reaction is effectively buffered mitigating adverse chemical potential changes during prolonged electrolyses. Figure 4-2 shows the current-voltage behavior of the CAN electrocatlytic mediator before and after the addition of the organic substrates.

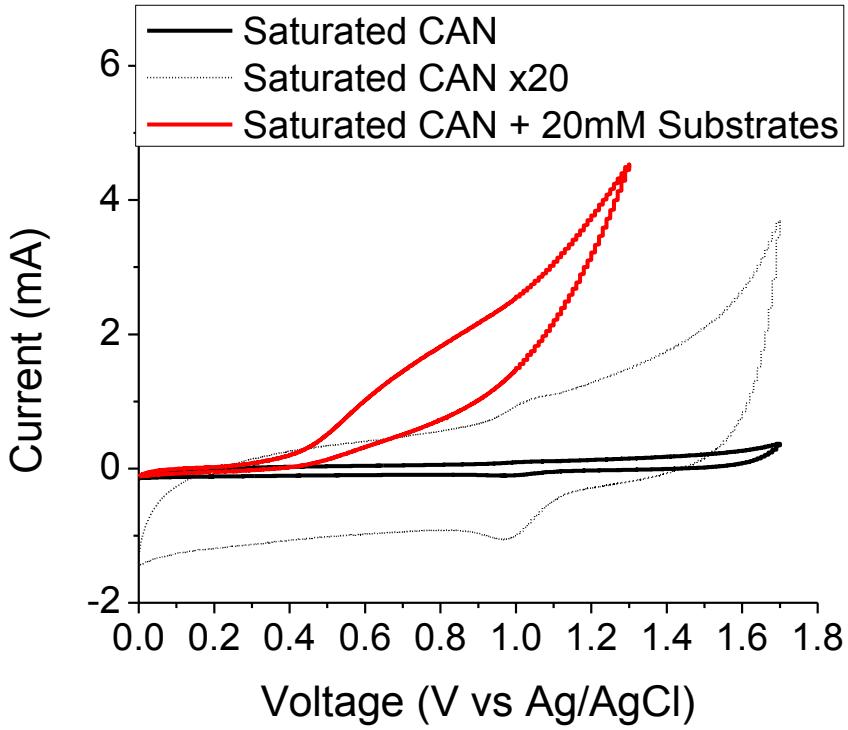

Figure 4-2 Cyclic voltammograms for the electrochemical behavior of the 5mM cerium ammonium nitrate electrocatalyst in 8:3:1 CH_3CN:THF:MeOH 0.8 M $TEABF_4$ solution using a Tokai glassy carbon rod (2.55 cm^2 working area) after sparging the H-cell with N_2. A redox feature corresponding to the Ce(III/IV) couple can be seen at 1.0 V vs Ag/AgCl. Scan rate is 100 mV/s. Currents exceeding 5 mA in the electrochemical H-cell exceeded the potentiostat's voltage limit and could not be acquired. Current behavior in red corresponds to 20 mM o-phenylendiamine and 20 mM syringaldehyde which matches well with faradaic current behavior for the condensation reaction shown in Figure 4-7.

In the absence of the CAN mediator, a cloudy violet-black mixture of oxidized phenolic oligomers and stable organic radicals are produced. I performed CV experiments using a BASi glassy carbon electrode 3 mM diameter working electrode, an Ag/AgCl wire as the reference electrode which I separated from solution using a glass compartment and Vycor tip. I utilized a platinum wire as the counter electrode. The electrolytic solution was an 8:3:1 CH_3CN:THF:MeOH mixture with 0.8 M Et_4NBF_4. In attempting to elucidate the relationship between substrates and electrocatalytic current, concentrations of mediator and substrates were varied as per Table 4-1 and Figure 4-3.

Table 4-1 The varying concentrations of catalyst and substrates for the anodic condensation reaction as performed in 0.8 M Et_4NBF_4 and 8:3:1 CH_3CN:THF:MeOH. Cyclic voltammograms at each of these concentrations were performed at various scan rates.

Run	CAN (mM)	o-phenylenediamine (mM)	Syingaldehyde (mM)
1	**1.25**	0	0
2	**2.5**	0	0
3	**5**	0	0
4	**5**	10	10
5	**5**	20	10
6	**5**	40	10
7	**5**	40	20
8	**5**	40	40

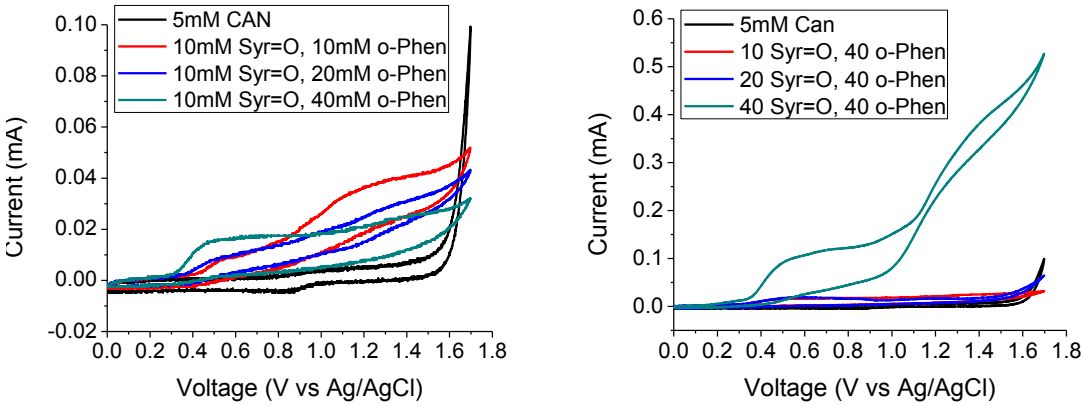

Figure 4-3 Increasing substrate concentrations in cyclic voltammograms of 5mM CAN in 8:3:1 CH_3CN:THF:MeOH and 0.8 M $TEABF_4$ using a BASi glassy carbon working electrode 3 mm in diameter after sparging with N_2. Scan rate is 100 mV/s. (Left) shows current behavior with increasing o-phenylenediamine. Currents at higher potentials begin to decrease with increased o-phenylenediamine, possibly indicating the formation of current hindering intermediates such as stable aromatic radicals or oligomers. Lower potential current begins to increase with increased concentration indicating the potentials for the initial oxidation of o-phenylenediamine is less positive than the potential required for activation of the catalyst without substrate available. (Right) shows current behavior with increasing syringaldehyde. At 40 mM, current dramatically increases and current-voltage behavior begins to match well with that shown in Figure 4-7.

Of additional note, an unintentional but beneficial consequence came from using

Et_4NBF_4 as the supporting electrolyte and methanol as part of the solvent mixture. The Re

catalyst becomes catalytically active at overpotentials less negative than previously reported.[15] While the $E_{1/2}$ for the relevant reduction of the catalyst resides at -1.60 V vs NHE, the onset of catalysis occurs at a less negative potential as shown in Figure 4-4. We attribute this to Et_4N^+ and methanol facilitating Cl^- loss from the catalyst and the subsequent stabilization of the active Re^{-1} species.[6] Further electrochemical evidence for this appears in Figures 4-5 and 4-6 which show shifts in current onset upon the addition of methanol and THF.

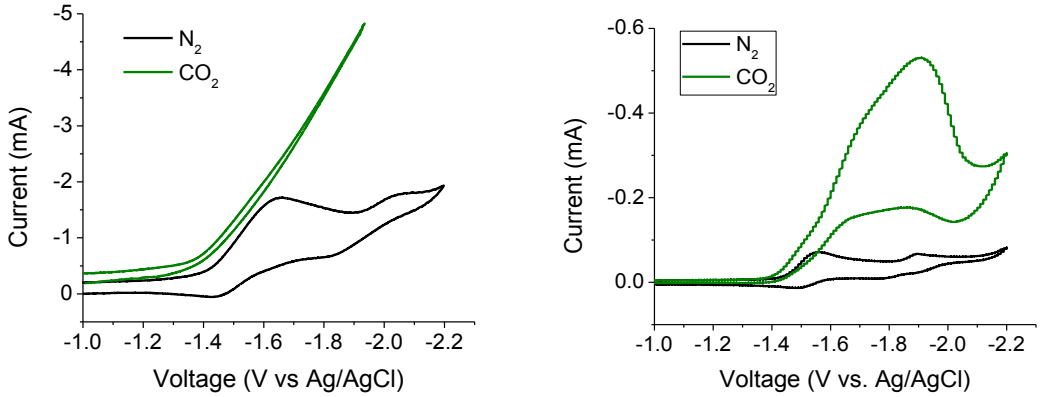

Figure 4-4 (Left) Cyclic voltammograms of 5 mM Re(bipy-tBu)$(CO)_3$Cl catalyst in 8:3:1 CH_3CN:THF:MeOH 0.8 M Et_4NBF_4 solution using a Tokai glassy carbon rod (2.55 cm^2 working area) after sparging with N_2 and CO_2. Scan rate is 100 mV/s. Due to high series resistances when using a separator, currents exceeding ±5 mA exceeded standard potentiostat voltage limits. (Right) Cyclic voltammogram data for the same conditions using an analytical BASi 3 mm diameter glassy carbon working electrode in a custom Teflon cell. Ag/AgCl wire was used as the reference and Platinum wire was used as the counter electrode.

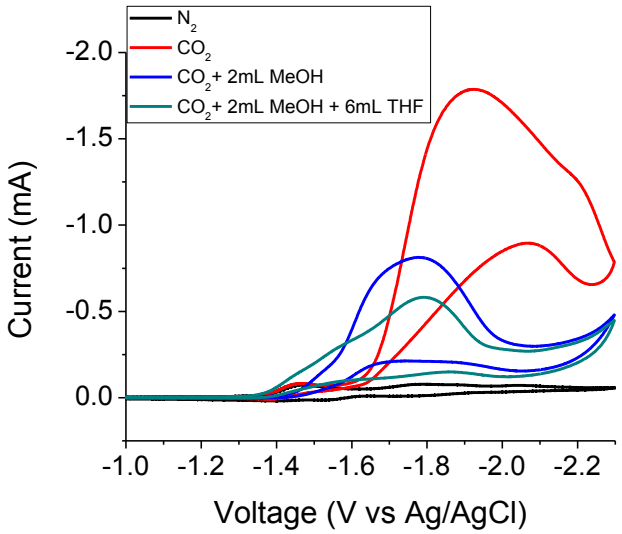

Figure 4-5 A series of cyclic voltammograms with a scan rate of 100 mV/s showing the effects of sequentially adding the different components of the solvent mixture to an initial concentration of 0.12 M Et_4NBF_4 and 7.5 mM Re(bipy-tBu)$(CO)_3$Cl catalyst in 16 mL CH_3CN. In black is the voltammogram corresponding to an N_2 sparged solution. In red is a CO_2 sparged solution with trace water acting as the weak Brønsted acid for the CO_2 reduction. In blue, 2 mL of methanol is added shifting the onset of catalytic current to less negative potentials. In green, 6 mL of THF is added with the additional effect of lowering the onset of faradaic current. Peak current is lowered to 75% of the previous CV due to dilution of catalyst.

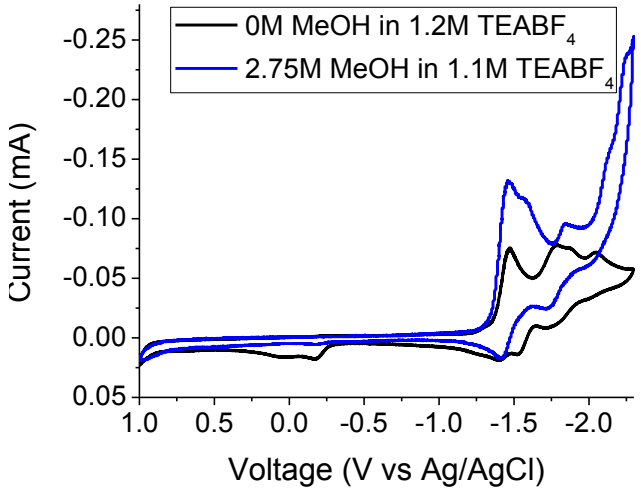

Figure 4-6 Cyclic voltammagrams of Re(bipy-tBu)$(CO)_3$Cl at a scan rate of 100 mV/s in N_2 sparged solutions with and without added methanol. The initial increase in current and lack of a reverse oxidation peak near -0.2 V is attributed to methanol facilitating Cl^- loss from the catalyst.

In my preparation for the pairing of these two half-reactions, I have found conditions that lower the onset potential for the CO_2 reduction catalyst, an unexpected result and one that assists in bringing down the energy costs for that half-reaction and therefore for the complete paired reaction as well.

4.3 Paired Electrolysis of Carbon Feedstocks

When driving a paired electrolysis, attempting to arbitrarily increase rates of product formation by increasing applied voltage comes at progressively higher energy costs. One must target an acceptable current range – not so low that rates of product formation are slow and not so high that energy loss due to resistance becomes prohibitively costly or undesirable side reactions predominate. To begin such a task, we need to consider electrochemical reactions as whole processes. Take as example the generic anodic half-reaction A of the form $A_{Reduced}$->$A_{Oxidized}$. This half-reaction is paired with a cathodic half-reaction B of the form $B_{Oxidized}$->$B_{Reduced}$. The total reaction of A+B may be described as ($A_{Reduced}$+$B_{Ozidized}$)->($A_{Oxidized}$+$B_{Reduced}$). As previously described in E4-1 and E4-2 and temporarily putting aside resistive voltage losses, the total voltage required to drive this reaction at a given rate may be described as $\Delta V=V_A-V_B$. Optimizing the energy efficiency of the cell requires minimizing ΔV. For most synthetic reactions, this is done by choosing a reaction at the counter electrode that occurs readily at a minimum potential. This lowers the energy barrier for the overall process and hence the desired reaction at the working electrode. However, for a paired electrochemical reaction where both reactions are defined by a synthetic goal, this is not an option.

Instead we focus our aim on minimizing the total voltage applied to maintain reaction desired rates. In the glass cells used to conduct the paired electrolysis reaction shown in Figure 4-1, the separator is a fine glass frit wherein small ion electrolytes such as $LiClO_4$, $LiPF_6$, and Et_4NBF_4 give nearly constant series resistances of 700 ± 50 Ω across both electrodes regardless of current demand or electrode area. Since the voltage required for electrolysis is typically on the order of 1 to 3 volts, if current demand is greater than a few milliamps, IR_{Series} becomes the dominant voltage term. Figure 2 shows steady state current-voltage behavior for both half-reactions and the total cell as a function of stepped cathodic potentials. The cathode compartment contains 5 mM $Re(bipy\text{-}tBu)(CO)_3Cl$ and saturated carbon dioxide. The anode compartment contains 5 mM ceric ammonium nitrate (CAN), 40 mM syringaldehyde, and 44 mM o-phenylenediamine. CAN functions as the electrocatalytic mediator for the oxidative condensation reaction and has a relevant $E_{1/2}$ of 1.0 V vs Ag/AgCl as measured, as demonstrated in Figure 4-2.

As previously stated, I used a mixed solvent system of 8:3:1 CH_3CN:THF:MeOH with 0.8 M Et_4NBF_4 supporting electrolyte both to ensure solvation of substrates and product at the anode compartment and to maintain a constant proton concentration for the cathodic reaction. Figure 4-7 shows the current-voltage behavior under solution stirring for each half-reaction and for the whole cell. For the isolated current voltage behavior of the half-reactions, the current initially appears exponential as a function of applied potential. This is consistent with kinetically limited electrolytic conditions. When looking at the whole cell, however, the current responds nearly linearly at higher voltages with a slope of $(840\ \Omega)^{-1}$ which is consistent with series-resistance becoming the dominant term.

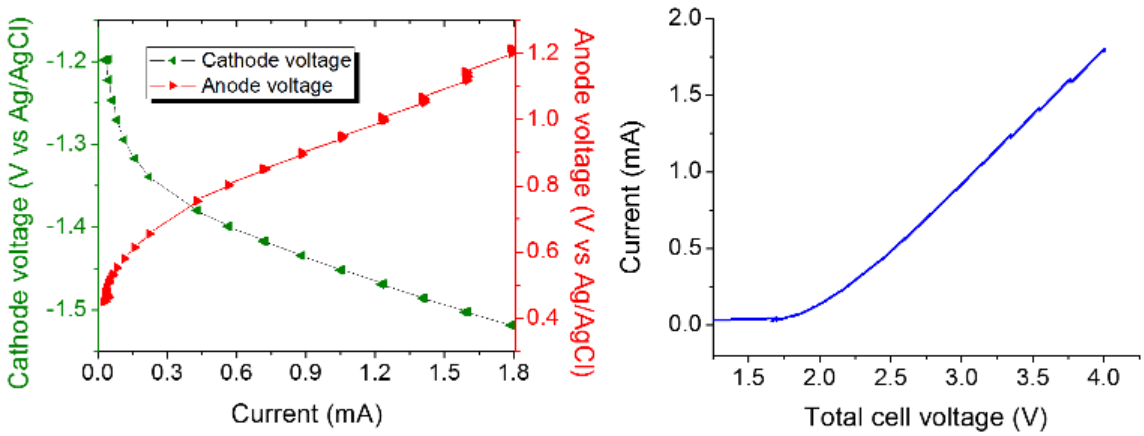

Figure 4-7 Steady state current-voltage behavior for each half-reaction was studied via holding the cathode at incrementally decreasing potentials vs an Ag/AgCl reference electrode and measuring the current and anode voltage. Cathode compartment contains 5 mM Re(bipy-tBu)$(CO)_3$Cl. Anode compartment contains 5 mM CAN, 40 mM syringaldehyde, and 44 mM o-phenylenediamine. Data is corrected for solution resistance between active electrodes and reference electrodes. (Left) Under electrolysis conditions, current rises nearly exponentially as a function of applied voltage at both the anode and the cathode. Higher overpotentials are required at the anode with respect to the cathode which is indicative of larger barriers and less efficient catalysis. (Right) The current-voltage response of the electrolysis cell exhibits exponential behavior at lower current demands and becomes approaches linearity due primarily to separator resistance. Total series resistance between anode and cathode was measured before and after steady-state measurements to be 740 Ω.

If one were to drive these electrolysis cells with a photovoltaic device, the voltage and current produced by the device must be within the range specific to the reaction conditions and equipment used. A custom photovoltaic device was created to produce appropriate voltages and currents by modifying commercially available single crystalline SuperCell photovoltaic cells. Under direct solar irradiation, the device performed with a solar energy conversion efficiency of 13% at a maximum power point at 3.1 mA and 4.3 V as shown in Figure 4-8.

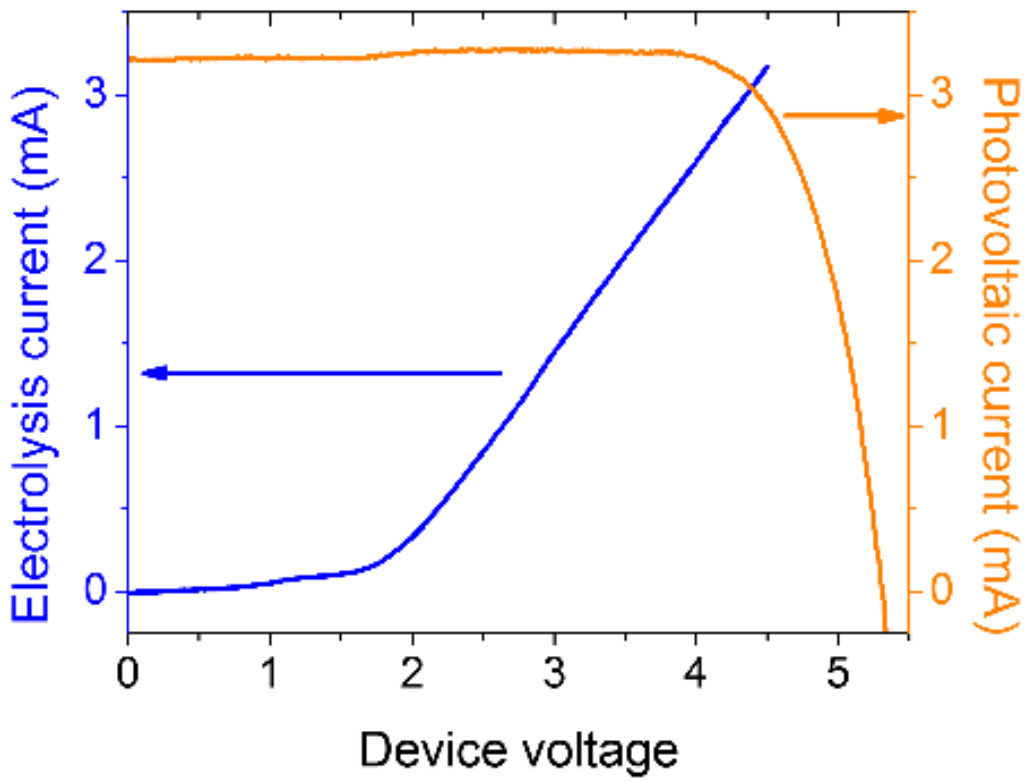

Figure 4-8 Current-voltage behavior for both the electrochemical cell and the custom photovoltaic device under 98 mW/cm^2 solar illumination. When the electrolysis cell is driven by the photovoltaic, the operating current and voltage is determined by where the two curves intersect. Scan rates for both were 20 mV/s. Cathode compartment contains 5 mM Re(bipy-tBu)(CO)$_3$Cl. Anode compartment contains 5 mM CAN, 40 mM syringaldehyde, and 44 mM o-phenylenediamine.

Using this device to power the electrochemical cell, I performed bulk electrolyses under peak mid-day solar flux in La Jolla, CA under various weather conditions, but in order to mitigate variance between experiments, I performed constant current electrolyses to simulate pairing with a photovoltaic under steady solar flux. Voltage demand for a constant current chronopotentiometry held at 2.75 mA begins at 4V and stays nearly constant for about half an hour then increases progressively with time as can be seen in

Figure 4-9. By tracking current and anode voltage as a function of time for a constant cathode-voltage electrolysis, it is immediately revealed that the increased voltage demand arises almost entirely from the anode half-reaction, as seen in Figure 4-10. Two major effects at the anode occur: [1] the condensation product reaches maximum solubility and begins to deposit at the anode and [2] reactants begin to deplete, increasing the potential required to maintain constant current.

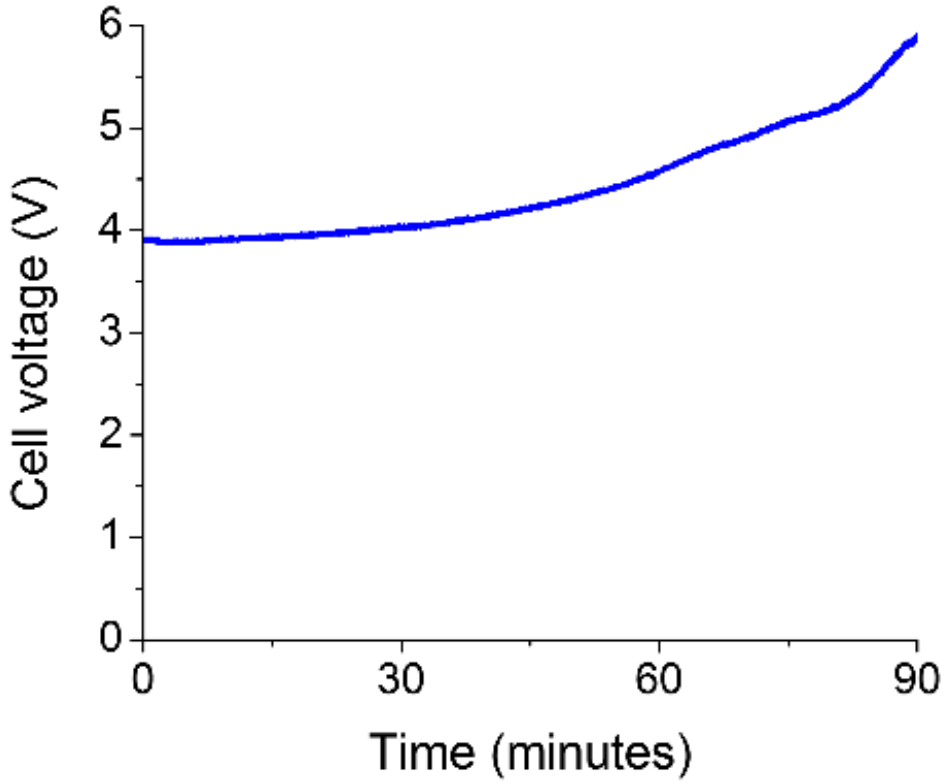

Figure 4-9 Voltage vs time for the paired electrolysis when performed under constant current conditions of 2.75 mA. Cathode compartment contains 5 mM Re(bipy-tBu)$(CO)_3$Cl. Anode compartment contains 5 mM CAN, 40 mM syringaldehyde, and 44 mM o-phenylenediamine. Over time, the voltage demand increases, indicating that either reaction rates are diminishing or resistance is increasing. Series resistance between electrodes was measured before and after experiments and was determined to stay constant within 5 Ω.

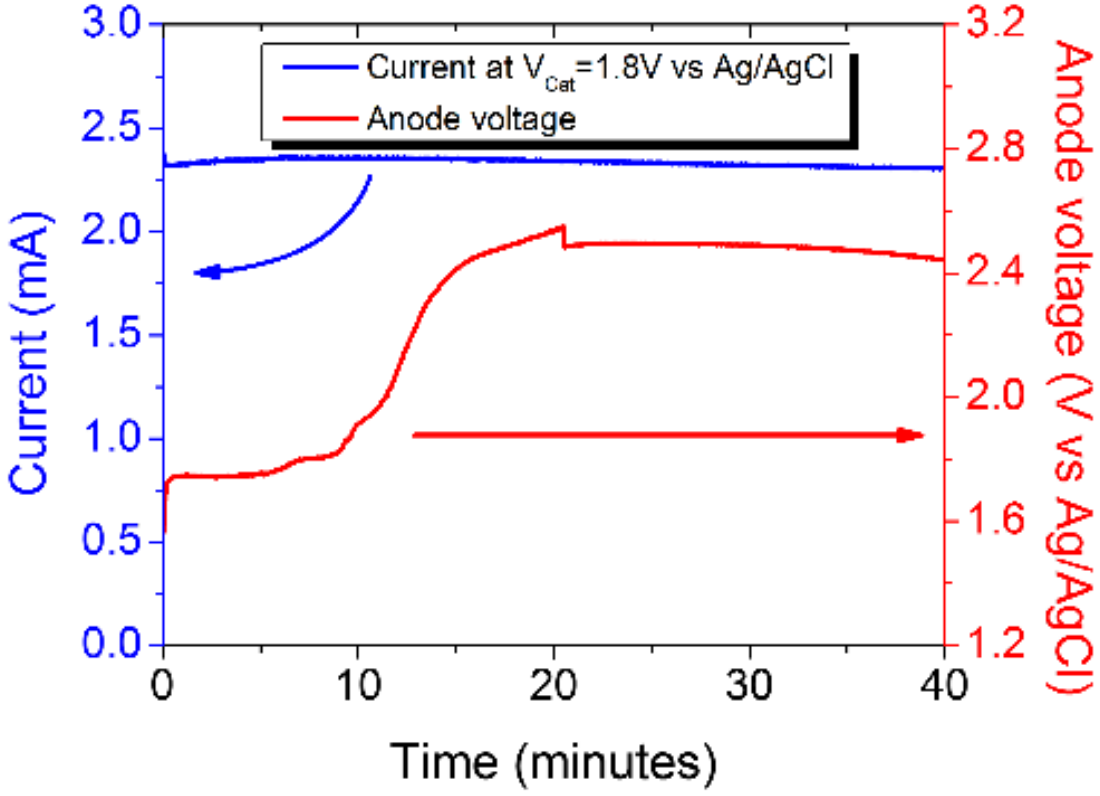

Figure 4-10 Current and anode voltage during constant cathode voltage electrolysis using lower initial substrate concentrations in anode chamber. Cathode compartment contains 5 mM Re(bipy-tBu)$(CO)_3$Cl. Anode compartment contains 5mM CAN, 20mM syringaldehyde, and 22 mM o-phenylenediamine. Both compartments were sparged with CO_2 until saturation. Cathode voltage was held at -1.8V vs Ag/AgCl. Current remained nearly constant throughout electrolysis, consistent with increased voltage demand arising from the anode reaction rather than the cathode reaction. Series resistance between anode and cathode was measured as 710 Ω and 720 Ω before and after electrolysis, respectively.

Table 4-2 Faradaic yield for CO and the anodic condensation product during a 2.75 mA constant current electrolysis. Cathode compartment contains 5 mM Re(bipy-tBu)$(CO)_3Cl$. Anode compartment contains 5mM CAN, 20mM syringaldehyde, and 22 mM o-phenylenediamine. Measurement of condensation product yield required isolation and concentration of the product from the anode working solution to ensure sufficient analyte for product quantification.

Faradaic Yield (%)	Electrolysis Time		
Products	32 min	64 min	120 min
CO	~100%	~100%	~90%
Condensation Product			~65%

While this paired reaction shows quantitative yields of CO and high yields of the condensation product as determined by gas chromatography and NMR respectively, the increasing voltage demand provides further motivation to investigate improved catalysts and catalytic conditions for this condensation product. Even so, when such reactions are scaled as industrial processes they are maintained at conditions that optimize reaction rates, yields, energy efficiency. A practical implementation of this pairing should maintain conditions similar to early portions of this electrolysis with maintained substrate concentrations and extracted product.

4.3 Materials and Methods

Materials

The following chemicals were used without further purification. Syringaldehyde (≥98%), o-phenylenediamine (≥99.5%), Et_4NBF_4 (≥99%), CAN (≥99.99%), Methanol (≥99.8%). Re(bipy-tBu)$(CO)_3Cl$ was synthesized as previously published.[15] Acetonitrile (CH_3CN)

and tetrahydrofuran (THF) were dried over basic alumina with a custom dry solvent system.

Electrode Preparation

5 mm diameter glassy carbon rod electrodes were purchased from Tokai Carbon. Before experiments, electrodes were cleaned with piranha solution and aqua regia to remove any organic or metal depositions. Ag/AgCl electrodes were prepared by anodizing of 99.999% pure silver wire in 3 M HCl solutions. 3mm diameter glassy carbon working electrodes used for cyclic voltammetry scans in the Supplementary Figure data were purchased from BASi and polished using a series of standard alumina and diamond particles ending with a 1 µm diamond polish, rinsed with methanol, and potentially swept in blank working solution until capacitive scans were clean and showed no further hysteresis.

Photovoltaic Device Preparation

The photovoltaic device was created from eleven individual cells rated to perform with a short circuit current of 10 mA and open circuit potential of 0.5 V with dimensions of 0.2cm x 2.2cm under standard Air Mass 1.5 solar irradiance. The cells for this paper were chipped to ¼ their original area to produce ¼ the current in order to better current match the electrochemical cell and were soldered in series to produce the required voltage. Current voltage behavior under solar illumination was performed outdoors with direct normal incident irradiance under midday sun. Solar irradiance values were used as reported for the day and time of the experiments in La Jolla, CA.

Electrochemistry Solution Conditions

The cathode compartment contained 5 mM of the Re(bipy-tBu)$(CO)_3$Cl catalyst that was synthesized as previously published. The anode compartment contained 5 mM of the electrocatalytic mediator ceric ammonium nitrate (CAN), 40 mM o-phenylenediamine, and 44 mM syringaldehyde unless otherwise noted. The solution was magnetically stirred using Teflon bars during steady state experiments including chronopotentiometry, chronoamperometry, and bulk electrolyses. A mixed solvent system of 8:3:1 CH_3CN:THF:MeOH and 0.8 M Et_4NBF_4 was used for the working solution. Bone dry N_2 or bone dry CO_2 (<10 ppm H_2O) was sparged into stirred solution from both compartments for five minutes.

Steady State Potentiometry And Linear Sweep Voltammetry

All electrochemical experiments were performed a Gamry Reference 600 Potentiostat. A ~30 mL total volume glass H-Cell with fine glass frit and shared head space was used for all paired electrolysis studies as shown in Supplementary Fig 1. Cells were cleaned with piranha solution and aqua regia and sealed with septa with thin wire leads then taped. Cells were tested to ensure they were gas tight by filling cells with forming gas and measuring H_2 concentration over the course of 4 hours. Reference electrodes were separated from solution via glass and vycor tip. Ferrocene was added as an internal standard to solution after experiments were completed to verify voltage position of reference electrodes. Resistance measurements between the glassy carbon electrodes and their respective reference electrodes ranged between 20 to 40 Ω. Post-experiment voltage compensation was performed for slow scan rate (≤ 20 mV/s) and steady state experiments and solution was magnetically stirred with Teflon coated stir bars.

Figure 4-11 Electrochemical H-cell sealed with septa. Each compartment contains its own Ag/AgCl reference electrode separated from solution by a glass tube terminated by a vycor tip and its own carbon rod electrode. Both compartments contain a mixture of 8:3:1 acetonitrile:tetrahydrofuran:methanol and 0.8 M Et_4NBF_4. As shown, the left compartment contains 5 mM ceric ammonium nitrate, 40 mM o-phenylenediamine, and 44 mM syringaldehyde. The right compartment contains 5 mM Re(4,4′-di-tert-butyl-2,2′-bipyridine)$(CO)_3Cl$.

Stepped cathodic potential amperometry was performed with 25 mV steps held for 60 s. Anode potential with respect to the anode compartment's Ag/AgCl reference electrode was simultaneously recorded via the voltage input capability of the Reference 600 potentiostat. Linear sweep voltammetry were performed at 20 mV/s under stirring conditions. The scan rate was chosen such that slower scan rates produced identical current-voltage behavior.

Bulk electrolyses and product analysis

Bulk electrolyses were performed for both 60 minutes at constant current and 90 minutes and 120 minutes for constant voltage. Constant current experiments were performed at a set current of 2.75 mA. Constant voltage experiments were performed by holding the cathode voltage at -1.8 V vs Ag/AgCl. Anode voltage was measured as described in

previous section. Gas phase products were evaluated gas chromatography on a Hewlett-Packard 7890A series gas chromatograph equipped with two molsieve columns (30 m × 0.53 mm i.d. × 25 μm film). A 1 mL injection was split between the two columns, one with N_2 carrier gas and one with He carrier gas, in order to quantify both CO and H_2 simultaneously. No H_2 was detected. Gas chromatography calibration curves were made by sampling known volumes of CO and H_2 gas. After bulk electrolyses, condensation products were first extracted in DCM from a pH 7 buffer then refluxed. Product was dissolved in deuterated methanol in order to take H-NMR spectra then analyzed via high resolution mass spectrometry.

Quantification of the products is shown below in Figures 4-12 and 4-13.

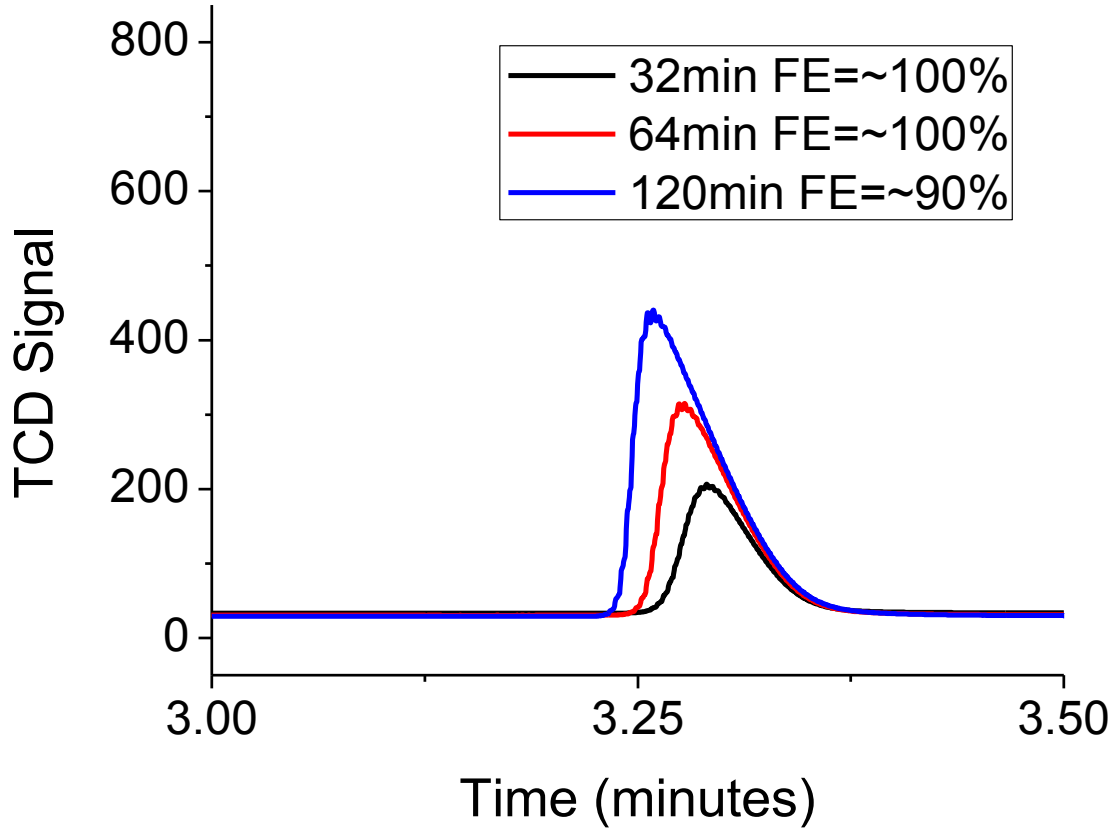

Figure 4-12 Gas chromatographs corresponding to samples from different times during a two hour bulk electrolysis with constant current of 2.75 mA as performed in an H-cell using glassy carbon rods. Cathode compartment contained 5mM Re(bipy-tBu)$(CO)_3$Cl. Anode compartment contained 5 mM CAN, 40 mM o-phenylenediamine, and 44 mM syringaldehyde. Both are sparged with CO_2 until saturation.

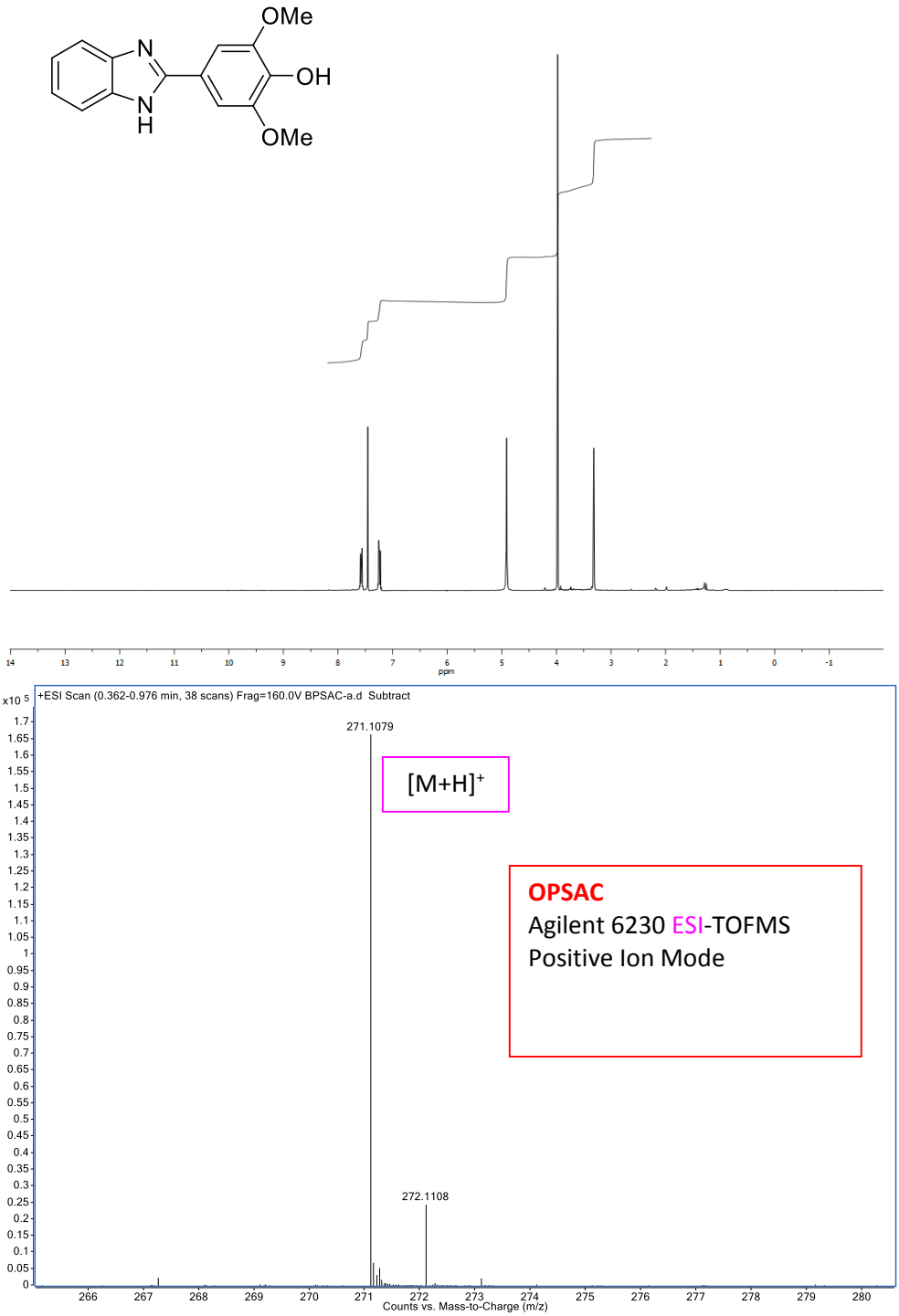

Figure 4-13 (Top) shows an H-NMR spectrum of the extracted product from the anode compartment using the same conditions as Figure 13. (Bottom) shows the high resolution mass spectrum of the isolated product post H-NMR with the majority peak corresponding to the protonated form of the benzimidazole product.

4.4 Conclusions

The principles discussed here represent fundamental concerns in evaluating chemical and energy demands of a paired electrolysis reaction. While further optimization of this example pairing through more energy efficient and earth-abundant catalysts would be desirable, this paired electrolysis represents one step in a fully integrated multi-step scheme for electrochemically generating intermediates in the conversion of renewable carbon feedstocks into high value commodity chemicals.[16]

4.5 Acknowledgements

Much of the material for this chapter comes directly from a manuscript entitled "Paired Electrolysis in the Simultaneous Upgrading of Two Renewable Carbon Feedstocks." by Mark J. Llorente, Bichlien N. Nguyen, Kevin D. Moeller, and Clifford P. Kubiak, which has been submitted for publishing. The dissertation author is the primary author of this manuscript.

4.6 References

1 Frontana-Uribe, B. A., Little, R. D., Ibanez, J. G., Palma, A. & Vasquez-Medrano, R. Organic electrosynthesis: a promising green methodology in organic chemistry. *Green Chemistry* **12**, 2099-2119, doi:10.1039/C0GC00382D (2010).

2 Yoshida, J.-i., Kataoka, K., Horcajada, R. & Nagaki, A. Modern Strategies in Electroorganic Synthesis. *Chemical Reviews* **108**, 2265-2299, doi:10.1021/cr0680843 (2008).

3 Sperry, J. B. & Wright, D. L. The application of cathodic reductions and anodic oxidations in the synthesis of complex molecules. *Chemical Society Reviews* **35**, 605-621, doi:10.1039/B512308A (2006).

4 Nguyen, B. H., Perkins, R. J., Smith, J. A. & Moeller, K. D. Solvolysis, Electrochemistry, and Development of Synthetic Building Blocks from Sawdust.

The Journal of Organic Chemistry **80**, 11953-11962, doi:10.1021/acs.joc.5b01776 (2015).

5 Li, K., An, X., Park, K. H., Khraisheh, M. & Tang, J. A critical review of CO2 photoconversion: Catalysts and reactors. *Catalysis Today* **224**, 3-12, doi:http://dx.doi.org/10.1016/j.cattod.2013.12.006 (2014).

6 Grice, K. A. & Kubiak, C. P. in *Advances in Inorganic Chemistry* Vol. Volume 66 (eds Aresta Michele & Eldik Rudi van) 163-188 (Academic Press, 2014).

7 Kim, D., Sakimoto, K. K., Hong, D. & Yang, P. Artificial Photosynthesis for Sustainable Fuel and Chemical Production. *Angewandte Chemie International Edition* **54**, 3259-3266, doi:10.1002/anie.201409116 (2015).

8 Kondratenko, E. V., Mul, G., Baltrusaitis, J., Larrazabal, G. O. & Perez-Ramirez, J. Status and perspectives of CO2 conversion into fuels and chemicals by catalytic, photocatalytic and electrocatalytic processes. *Energy & Environmental Science* **6**, 3112-3135, doi:10.1039/C3EE41272E (2013).

9 Martin, A. J., Larrazabal, G. O. & Perez-Ramirez, J. Towards sustainable fuels and chemicals through the electrochemical reduction of CO2: lessons from water electrolysis. *Green Chemistry* **17**, 5114-5130, doi:10.1039/C5GC01893E (2015).

10 Suga, S., Okajima, M., Fujiwara, K. & Yoshida, J.-i. Electrochemical Combinatorial Organic Syntheses Using Microflow Systems. *QSAR & Combinatorial Science* **24**, 728-741, doi:10.1002/qsar.200440003 (2005).

11 Guenot, B., Cretin, M. & Lamy, C. Clean hydrogen generation from the electrocatalytic oxidation of methanol inside a proton exchange membrane electrolysis cell (PEMEC): effect of methanol concentration and working temperature. *J Appl Electrochem* **45**, 973-981, doi:10.1007/s10800-015-0867-3 (2015).

12 Winkler, M. T., Cox, C. R., Nocera, D. G. & Buonassisi, T. Modeling integrated photovoltaic–electrochemical devices using steady-state equivalent circuits. *Proceedings of the National Academy of Sciences* **110**, E1076-E1082, doi:10.1073/pnas.1301532110 (2013).

13 Kumar, B., Smieja, J. M., Sasayama, A. F. & Kubiak, C. P. Tunable, light-assisted co-generation of CO and H2 from CO2 and H2O by Re(bipy-tbu)(CO)3Cl and p-Si in non-aqueous medium. *Chemical Communications* **48**, 272-274, doi:10.1039/C1CC16024A (2012).

14 Keith, J. A., Grice, K. A., Kubiak, C. P. & Carter, E. A. Elucidation of the Selectivity of Proton-Dependent Electrocatalytic CO2 Reduction by fac-

Re(bpy)(CO)3Cl. *Journal of the American Chemical Society* **135**, 15823-15829, doi:10.1021/ja406456g (2013).

15 Smieja, J. M. & Kubiak, C. P. Re(bipy-tBu)(CO)3Cl−improved Catalytic Activity for Reduction of Carbon Dioxide: IR-Spectroelectrochemical and Mechanistic Studies. *Inorganic Chemistry* **49**, 9283-9289, doi:10.1021/ic1008363 (2010).

16 Francke, R. & Little, R. D. Redox catalysis in organic electrosynthesis: basic principles and recent developments. *Chemical Society Reviews* **43**, 2492-2521, doi:10.1039/C3CS60464K (2014).

Chapter 5

Future work

5.1 Future Investigations in Photo Fuel Cells

Surface Dependent Product Selectivity

In the pursuit of a high efficiency optical fuel cell, TiO_2 and WO_3 have shown well behaved product selectivity for C-C and C-H activation consistent with the influence of pH; alkaline solutions destabilize radical species with respect to neutral or acidic media and thus facilitate complete ionization inhibiting the production of unwanted side reactions such as radical-radical bond formation and beta hydride elimination.[1] Double bond formation from beta hydride elimination was more readily detected from fuel oxidation products in pH 1 solutions. I demonstrated in Chapter 3 the capacity for illuminated TiO_2 to perform C-C and C-H activation to create desirable oxidation intermediates, but the specific mechanism by which the surface interacts with substrates and electrolyte has not been fully elucidated. In order to optimize a material's capacity for this selective oxidation pathway, we must determine the reaction steps and at what sites these steps take place.

The most photoactive phases of TiO_2 are the stable rutile phase and metastable anatase phase. The form of TiO_2 used most in my research was a commercially available mixture of both rutile and anatase nanoparticles that produces a synergistic effect that

increases photocatalytic activity compared to either of the two phases alone.[2,3] Single crystalline rutile TiO_2 is commercially available, but crystalline anatase-phase TiO_2 has been a recent advancement.[4] A recent paper compares the most reactive surface of rutile TiO_2, {101}s, with the isolated and highly active {001} anatase over various film thicknesses and found the {001} anatase surface to be nearly twice as active as the {001} rutile.[5] Additionally, the {111} anatase surface has been produced and shown to produce a nearly order of magnitude higher water splitting efficiency than the {001} surface.[6] All of the previously described surfaces would make excellent candidates to test differences in product selectivity and photooxidative efficiency where the best balance of selectivity and photoactivity would need to be determined.

<u>TiO_2 Doping and Band Gap Tuning</u>

As shown in the electrode materials I produced, annealed p25 nano-particle TiO_2 films show promise as a photoanode material in fuel cells, but their lange band gaps create a large excitation energy loss. Of particular interest, black-TiO_2 is formed by doping TiO_2 under higher temperature high pressure hydrogen to produce a material with higher electrical conductivity and a smaller effective band gap.[7,8] The most studied form of black-TiO_2 is, quite conveniently, hydrogen-annealed p25 nanoparticles and may be formed by placing p25 TiO_2 under 35 bars of hydrogen gas at 25°C. The added interstitial hydrogen raises the valence band of the TiO_2 by nearly 1 V and thereby lowers the required minimum photon excitation energy to ~1.82 eV, and as the color would suggest a wider spectrum of light is absorbed by the material than intrinsic TiO_2. Initial experiments in photocatalytic oxidative activity show effective hydrogen release from oxidized methanol under visible light illumination.[9] By using black TiO_2, the smaller

bandgap lowers the light energy required per photon to produce the same photocurrent, and its increased conductivity would improve charge separation which in turn lowers recombination rates at mild anodic potentials. Both effects would enhance photocurrent onset and magnitude as compared to the films used in my previous studies. In principle, black TiO_2 should be entirely compatible with the alkaline conditions used in my previous sequential oxidation experiments.

The difference in efficiency from using different band gap materials may be seen in the voltage dependent equation E5-1. The band gap energy dependent term is $\lambda_{excitation}$, the wavelength of the photons needed to excite photoanode.

$$Efficiency = \frac{[N_e \times V_{output}] - \left[\frac{100\%}{IPCE(V_{anode})} * \frac{1.24\times10^{-9} V\cdot nm}{\lambda_{excitation}}\right]}{\left[\frac{\Delta H_{fuel}}{F}\right]}, \qquad \textbf{E5-1}$$

$$V_{output} = V_{anode} - V_{cathode} = V_{anode} - \left(1.23V + 0.59V \times pH + V_{overpotential}\right)$$

To understand the equation, one may focus on the three bracketed terms. The two in the numerator represent the electrical energy output and light energy required in mineralizing a fuel molecule, respectively. The denominator represents the chemical energy in a fuel molecule released through its complete mineralization. N_e is the number of electrons that can be extracted through mineralization. IPCE represents the effective current multiplication exhibited by the fuel cell as described in Chapter 2. ΔH_{Fuel} is the heat of combustion for a mole of fuel and F is the charge in coulombs per mole of electrons. In this equation we assume a 100% power efficient light source and negligible surface recombination of excited charges.

As evident from the second bracketed term, higher current multiplication and longer excitation wavelengths increase the fuel cell's power conversion efficiency.

Assuming black TiO_2 exhibits at least the same IPCE as undoped TiO_2 and that the excitation wavelength required by black TiO_2 corresponds to its reported band gap, the 1 V band gap decrease would correspond to a ~35% decrease in light energy required for complete fuel consumption.

Light Intensity Shaping to Mitigate Over-Oxidation by Photoanodes

While I have demonstrated the successful activation of C-H and C-C bonds to form alcohols and ketones on photoexcited TiO_2, we must look to prevent photogenerated holes from oxidizing other reaction intermediates. Even acetone may be considered an undesirable product if it is generated by the photoanode. One method for mitigating unwanted oxidation at the TiO_2 surface may be through light intensity shaping. Instead of a constant high intensity beam, high intensity pulses of light could be used to limit the photoexcited holes delivered to the anode surface and prevent over-oxidation of a molecule. If the light pulses are too brief and too sharp a majority of the current will be used in charging and discharge electrolytic capacitance near the surface or maintain photovoltage too quickly to facilitate electron extraction as evidenced by the suppression of current multiplication at high frequency intensity modulation.[10,11] Conversely, if light pulses are too long, there may be no change in product selectivity, and pulsing would serve no purpose. In order to evaluate this method, light pulses of varying duration, intensity, and spacing could be used to illuminate TiO_2 anode materials. Product distributions may then be analyzed by standard means including gas chromatography and mass spectrometry. Maximum alcohol yield and maximum current multiplication may occur under different light conditions and therefore must be treated as separate targets to be balanced later.

Anode Architecture

Once the desired intermediates have been produced, they must be captured and oxidized by a separate dark anode material to prevent the waste of light energy. While I tested the merits of anode proximity and induced mass transport in Chapters 2 and 3, electrode architecture may be designed to minimize diffusion distance between the photoanode and dark anode materials. As depicted in Figure 5-1, Interdigitated electrodes could help maintain high electrode surface areas and optimize the distance between the two electrodes over those regions. In attempting to minimize the distance of the two electrodes, one must also look to mitigate voltage "cross-talk" between electrodes as shown in Chapter 3 between planar gold and TiO_2 electrodes wherein the effective anodic surface potential of the gold was reduced by proximity to the illuminated electrode.

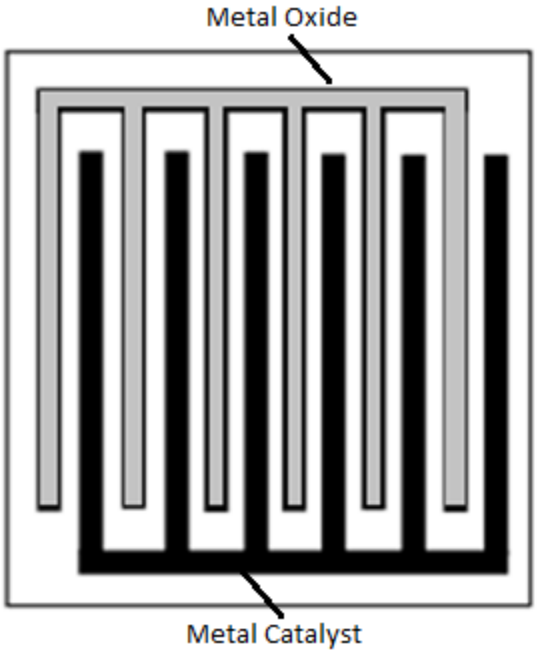

Figure 5-1 Basic interdigitated electrode scheme. By varying the dimensions and distance of the electrodes, one may not only optimize diffusion rates between electrodes but also probe the field interactions between photoilluminated metal oxides and the close proximity metal catalyst. Both materials may share a back contact or be held at different potentials.

5.2 Prospects for Paired Electrolysis in Sustainable Chemistry

Multiple Synthetic Steps Driven by One Paired Electrolysis

The pairing of two high value half-reactions can represent a net gain in energy efficiency by reducing energy costs compared to each half-reaction paired to an inexpensive but useless half-reaction. Additionally, same-site production of reactants via electrochemical processes could turn what would be a byproduct into a downstream feedstock for a multi-step reaction. One may pair any oxidation reaction such as organic polymerization, dehydrogenation, and chain cyclization with hydrogen or CO generation at the cathode. The H_2 and CO may then be used in downstream carbonylation, hydrogenation, and hydroformylation reactions to further upgrade those organic products. We can take as example the electrochemical carbonylation of alkynes. A palladium based electrocatalysts such as $Pd(II)(OAc)_2$ is released in its inactive Pd(0) form upon being displaced by ambient CO.[12] The catalyst may be electrochemically reactivated by oxidizing Pd(0) to its active Pd(II) form. In order to replace the CO consumed in this reaction, we could pair the anodic reaction with the reduction of CO_2 to CO and therefore complete a stoichiometrically balanced electrochemical process.

The principles outlined may be used to replace thermally driven chemical processes with analogous electrochemical reactions and prevent the need for added oxidizing and reducing reagents. As previously discussed, lignin represents a renewable resource for aromatics that could replace petroleum as a chemical feedstock, but it must be depolymerized and disassembled before use in synthetic processes. One specific method for depolymerization requires the catalyst-assisted oxidation of lignin followed by bond cleavage by formic acid.[13] The oxidation catalysts in the first step may be

refreshed by an anode wherein the electrons extracted by the catalyst may be supplied to the cathode to reduce CO_2 to formate. If the catalysts for lignin oxidation and formate production are sufficiently stable, the only inputs for this depolymerization are applied potential, the lignin substrate, and ambient CO_2 which is continually cycled back into formate.

The possible applications for paired electrolysis are too great to be enumerated here; in principle any anodic reaction may be paired with any cathodic reaction. These pairings represent a vast phase space to explore. As I showed in Chapter 4, the required overpotential to drive the CO_2 reduction catalyst was unexpectedly lowered by ~300 mV, and was only discovered, under conditions meant to optimize the sustained pairing of the two half reactions. Exploring and optimizing new pairings may reveal new knowledge about each half-reaction and allow us to further leverage our knowledge to create more efficient and sustainable chemical processes.

5.3 References

1 Klocke, E., Matzeit, A., Gockeln, M. & Schäfer, H. J. Electroorganie Synthesis, 55 [1]. Influences on the Selectivity of the Kolbe versus the Non-Kolbe Electrolysis in the Anodic Decarboxylation of Carboxylic Acids. *Chemische Berichte* **126**, 1623-1630 (1993).

2 Ohno, T., Sarukawa, K., Tokieda, K. & Matsumura, M. Morphology of a TiO2 Photocatalyst (Degussa, P-25) Consisting of Anatase and Rutile Crystalline Phases. *Journal of Catalysis* **203**, 82-86, doi:http://dx.doi.org/10.1006/jcat.2001.3316 (2001).

3 Scanlon, D. O., Dunnill, C. W., Buckeridge, J., Shevlin, S. A., Logsdail, A. J., Woodley, S. M., Catlow, C. R. A., Powell, M. J., Palgrave, R. G., Parkin, I. P., Watson, G. W., Keal, T. W., Sherwood, P., Walsh, A. & Sokol, A. A. Band alignment of rutile and anatase TiO2. *Nat Mater* **12**, 798-801, doi:10.1038/nmat3697

4 Liu, M., Piao, L., Zhao, L., Ju, S., Yan, Z., He, T., Zhou, C. & Wang, W. Anatase TiO2 single crystals with exposed {001} and {110} facets: facile synthesis and enhanced

photocatalysis. *Chemical Communications* **46**, 1664-1666, doi:10.1039/B924172H (2010).

5 Luttrell, T., Halpegamage, S., Tao, J., Kramer, A., Sutter, E. & Batzill, M. Why is anatase a better photocatalyst than rutile? - Model studies on epitaxial TiO2 films. *Scientific Reports* **4**, 4043, doi:10.1038/srep04043 (2014).

6 Xu, H., Reunchan, P., Ouyang, S., Tong, H., Umezawa, N., Kako, T. & Ye, J. Anatase TiO2 Single Crystals Exposed with High-Reactive {111} Facets Toward Efficient H2 Evolution. *Chemistry of Materials* **25**, 405-411, doi:10.1021/cm303502b (2013).

7 Chen, X., Liu, L. & Huang, F. Black titanium dioxide (TiO2) nanomaterials. *Chemical Society Reviews* **44**, 1861-1885, doi:10.1039/C4CS00330F (2015).

8 Zhu, Q., Peng, Y., Lin, L., Fan, C.-M., Gao, G.-Q., Wang, R.-X. & Xu, A.-W. Stable blue TiO2-x nanoparticles for efficient visible light photocatalysts. *Journal of Materials Chemistry A* **2**, 4429-4437, doi:10.1039/C3TA14484D (2014).

9 Sinhamahapatra, A., Jeon, J.-P. & Yu, J.-S. A new approach to prepare highly active and stable black titania for visible light-assisted hydrogen production. *Energy & Environmental Science* **8**, 3539-3544, doi:10.1039/C5EE02443A (2015).

10 Peat, R. & Peter, L. M. Determination of the rate constant for hole injection during current doubling at p-GaAs. *Electrochimica Acta* **31**, 731-734, doi:http://dx.doi.org/10.1016/0013-4686(86)87043-8 (1986).

11 H. Schoenmakers, G., Vanmaekelbergh, D. & J. Kelly, J. The mechanism of current-doubling reactions at ZnO photoanodes. *Journal of the Chemical Society, Faraday Transactions* **93**, 1127-1132, doi:10.1039/A606734D (1997).

12 Chiarotto, I. & Feroci, M. Palladium-catalyzed electrochemical carbonylation of 2-amino-1-alkanols to oxazolidin-2-ones under very mild conditions. *Tetrahedron Letters* **42**, 3451-3453, doi:http://dx.doi.org/10.1016/S0040-4039(01)00497-X (2001).

13 Rahimi, A., Ulbrich, A., Coon, J. J. & Stahl, S. S. Formic-acid-induced depolymerization of oxidized lignin to aromatics. *Nature* **515**, 249-252, doi:10.1038/nature13867